Characterization of A-plane Grown GaN on Sapphire Substrates by Electron Microscopy

THÈSE N^{O} 4193 (2009)

PRÉSENTÉE LE 2 MARS 2009

À LA FACULTÉ SCIENCES ET TECHNIQUES DE L'INGÉNIEUR
CENTRE INTERDISCIPLINAIRE DE MICROSCOPIE ÉLECTRONIQUE
PROGRAMME DOCTORAL EN SCIENCE ET GÉNIE DES MATÉRIAUX

ÉCOLE POLYTECHNIQUE FÉDÉRALE DE LAUSANNE

POUR L'OBTENTION DU GRADE DE DOCTEUR ÈS SCIENCES

PAR

Yadira ARROYO ROJAS DASILVA

M.Sc. in metallurgy and materials science,
Universidad Michoacana de San Nicolas de Hidalgo, Morelia, Mich., Mexique
et de nationalité mexicaine

acceptée sur proposition du jury:

Prof. K. Scrivener, présidente du jury
Prof. P. Stadelmann, directeur de thèse
Dr F. Diologent, rapporteur
Prof. K. Leifer, rapporteur
Dr J. Michler, rapporteur

ÉCOLE POLYTECHNIQUE
FÉDÉRALE DE LAUSANNE

Suisse
2009

To My Parents

Abstract

Gallium nitride (GaN) is one of the most interesting materials for devices applications such as blue light emitting diodes, laser diodes and high power and high temperature electronic applications, because of its large band gap (3.39 eV). Several growth techniques including metal organic chemical vapor deposition (MOCVD), molecular beam epitaxy (MBE) and hybrid vapor phase epitaxy (HVPE) are employed to synthesize high quality GaN. Sapphire, that is available in several orientations, is the common substrate to grow GaN. The GaN that grown on $c-(0001)$ sapphire, has a wurtzite structure and suffers of spontaneous polarization effects. These effects create internal electric fields that affect the operation and the efficiency of the devices. This work is part of a large effort to grow defects free GaN layers in non-polar geometries undertaken at LASPE-IQEP-EPFL. Among the non-polar geometries, the a-$(11\bar{2}0)$ GaN geometry has been selected. The specimens were produced using the HVPE and Epitaxial lateral Overgrowth (ELO) techniques and were fully characterized mainly by electron microscopy observations.

Despite the ELO improvements and smaller lattice mismatch in a-GaN ($\approx 1.1\%$) than c-GaN ($\approx 16\%$), a high density of dislocations and stacking faults are still observed. They are results of the lattice mismatch and the difference of the thermal expansion coefficients between the components. The reduction of defect density due to ELO has been found to be approximately two orders of magnitude for dislocations ($1\times10^{10}\,cm^{-2}$ to $3\times10^{8}\,cm^{-2}$) and for stacking faults ($1\times10^{6}\,cm^{-1}$ to $4\times10^{4}\,cm^{-1}$). In the ELO window areas, the threading dislocations have screw and mixed characters with Burgers vector $\vec{b}=\frac{1}{3}[11\bar{2}0]$ and $\vec{b}=\frac{1}{3}[11\bar{2}3]$ respectively. In the overgrown ELO areas, the dislocations have different characters such as screw character with $\vec{b}=\frac{1}{3}[11\bar{2}0]$, edge character with $\vec{b}=\frac{1}{3}[\bar{2}110]$ and partial dislocations.

Different types of stacking faults have been observed in the a-GaN film: basal (BSF) I_1 and

I_2, prismatic (PSF) $(11\bar{2}0)$ and $(10\bar{1}0)$. The I_2 BSF is bordered by two Shockley partial dislocations of Burgers vector $\vec{b} = \frac{1}{3} < 10\bar{1}0 >$ and its energy γ has been calculated: 50 $ergs/cm^2$. Prismatic stacking faults, $\vec{R} = \frac{1}{2}[1\bar{1}01]$ are located at the end of the I_1- BSFs, where stair rod dislocations are formed at the intersection of the two faults.

In order to know the influence of these defects on the optical properties, cathodoluminescence (CL) and microphotoluminescence (μ-PL) experiments were performed. These observations demonstrate that the optical properties are affected by the high density of stacking faults. The CL spectra show 4 different emission peaks where the dominant emission at 3.42 eV is attributed to the I_1 BSFs. In μ-PL spectra, 4 emission peaks are also observed, where the dominant one at 3.44 eV in the window area of the ELO mask is also attributed to the SFs and that at 3.49 eV in the overgrown mask area is the typical NBE transition. This shows that locally the GaN film is of good quality.

A single GaN quantum well (SQW) intercalated by two $Al_{1-x}Ga_xN$ layer were grown on HVPE-ELO templates by MBE. The structural characterization of six specimens have shown a high pits density on the sample surface ($1 \times 10^{12}\, cm^{-2}$) associated with the threading dislocations of screw character ending at the bottom of the pits. Moreover, the pits created at the intersection, near the surface, of several dislocations groups have been observed. A high density of BSFs (1×10^5 to $1 \times 10^6\, cm^{-1}$) was found in the samples, which are formed at $Al_{1-x}Ga_xN/GaN$ interface and propagated towards the specimen surface. We also observed that these stacking faults affect the optical properties of the SQW-GaN.

Our results have shown that the inhomogeneity of the optical properties of $a-(11\bar{2}0)$ GaN layers is associated with specific structural defects, in particular BSFs. These results provide guidelines to design new growth procedures aimed at improving the overall quality of such GaN films.

Keywords: a-GaN, r-sapphire, HVPE-ELO, defects, dislocations, stacking faults, optical properties.

Version résumée

Le nitrure de gallium, GaN, est un des plus intéressants matériaux pour les applications des dispositifs semiconducteur comme les diodes électroluminescencentes dans le bleu et le vert, les diodes laser et les applications électroniques de forte puissance et à haute température, en raison de sa grande largeur de bande interdite, 3.39 eV. Plusieurs techniques de déposition sont employées pour la synthèse de GaN de haute qualité, en particulier l'epitaxie en phase vapeur par décomposition d'organo-métallique "MOCVD" (Metal Organic Vapor Chemical Deposition), l' épitaxie par jets moléculaires "MBE" (Molecular Beam Epitaxy) ou l'Epitaxie d'hydrides en phase vapeur "HVPE" (Hydride Vapor Phase Epitaxy). Le saphir monocristallin, qui est disponible dans plusieurs orientations, est le substrat le plus utilisé pour la croissance épitaxiale de GaN. Le GaN qui croît sur saphir c-(001) a une structure polaire de type "wurtzite" et souffre des effets de polarisation spontanée qui dégrade le fonctionnement et l'efficacité des dispositifs. Ce travail fait partie d'une recherche dirigée par le laboratoire LASPE-IPEQ pour croître en géométrie non-polaire des couches de GaN libres des défauts cristallins. Parmi les géométries non-polaire possibles, la direction du croissance perpendiculaire à l'axe c, $a-(11\bar{2}0)$ GaN a été sélectionnée. Les films de GaN ont été produits en utilisant la méthode de déposition HVPE-ELO (Epitaxial Lateral Overgrowth) et caractérisés principalement par des observations en microscopie électronique.

En dépit des améliorations introduites par la méthode ELO et du faible écart des paramètres cristallins de la géométrie a-$(11\bar{2}0)$ ($\approx 1.1\%$) comparé à c-GaN ($\approx 16\%$), une haute densité de dislocations et de fautes d'empilement est encore observée qui peut être attribuée principalement à la différence de coefficients de dilatation thermique entre le saphir et le GaN. La réduction de la densité des défauts cristallin par la méthode ELO est de deux ordres de grandeur pour les dislocations ($1 \times 10^{11}\, cm^{-2}$ à $1 \times 10^{9}\, cm^{-2}$) et un ordre de

grandeur pour les fautes d'empilement ($1 \times 10^6\, cm^{-1}$ à $1 \times 10^5\, cm^{-1}$) . Dans la fenêtre du masque ELO, les dislocations ont un caractère vis ou mixte avec des vecteur de Burgers $\vec{b} = \frac{1}{3}[11\bar{2}0]$ ou $\vec{b} = \frac{1}{3}[11\bar{2}3]$. Au dessus du masque ELO, les dislocations ont des caractères différents, en particulier le caractère vis avec $\vec{b} = \frac{1}{3}[11\bar{2}0]$ et le caractère coin avec $\vec{b} = \frac{1}{3}[\bar{2}110]$.

Plusieurs types de fautes d'empilement ont été observés dans les films de GaN en géométrie a-$(11\bar{2}0)$: basales (BSF) I_1 et I_2, prismatique $(11\bar{2}0)$ et $(10\bar{1}0)$. Les BSFs de type I_2 sont délimitées par des dislocations partielles de vecteur de Burgers $\vec{b} = \frac{1}{3}[10\bar{1}0]$, et leur énergie de faute a été mesurée et est égale à 50 $ergs/cm^2$. Les fautes d'empilement prismatiques, $\vec{R} = \frac{1}{2}[1\bar{1}01]$ sont situés à la fin de deux BSFs de type I_1.

Afin de connaître l'influence de ces défauts sur les propriétés optiques, des observation en microphotoluminescence (μ-PL) et cathodoluminescence (CL) ont été réalisées. Ces observations ont démontré que les propriétés optiques sont affectées par la haute densité de fautes d'empilement. Les spectres CL montrent 4 pics d'émission différents, le pic principal à 3.42 eV pouvant être attribué aux fautes d'empilement I_1. Les spectres μ-PL montrent également 4 pics d'émission, les principaux sont à 3.44 eV dans la fenêtre du masque ELO et 3.49 eV au dessus du masque ELO. Ce résultat prometteur démontre que la croissance ELO rend possible la synthèse de films GaN de qualité localement suffisante pour que l'émission NBE (Near band edge) soit dominante.

La croissance par MBE a été utilisée pour déposer sur les échantillons HVPE-ELO une série de quatre couches de GaN et d'alliage AlGaN. La caractérisation structurale de six échantillons de ce type a montré une haute densité de piqûres (pits) ($1 \times 10^{12}\, cm^{-2}$) sur la surface des échantillons. Ces dèfauts sont associés à des dislocations de caractère vis. De plus, des puits créés à partir de l'intersection, proche de la surface, de plusieurs groupes de dislocations et d'une haute densité de PSFs (1×10^5 to $1 \times 10^6\, cm^{-1}$) provenant de l'interface entre GaN et $Al_{1-x}Ga_xN$ et se propageant vers la surface ont été observés. Les fautes d'empilement dans le film affectent les propriétés optiques du puit quantique GaN.

Nos résultats ont montré que l'hétérogénéité des propriétés optiques est associée à des

défauts structurels spécifiques, en particulier les BSFs. Ils fournissent des indications qui permettront de synthétiser des films minces de GaN de meilleures qualités structurelle et optique.

Mots-clés: a-GaN, r-saphir, HVPE-ELO, défauts crystallins, dislocations, fautes d'empilement, propriétés optiques.

Content

Chapter 1

Introduction

The present chapter provides a short overview of the Gallium nitride (GaN) based devices history. A description of the structural and optical properties of group-III nitrides, which have a wurtzite structure and grow normally in *c*-plane is provided. Nitrides which grow in c-plane (along the polar c-axis), suffer of polarization effects. Due to this polarization, non polar directions are chosen such as *a*-plane GaN. The most import difference between *c*- and *a*-GaN are reviewed.

1.1 Brief history of GaN

Group-III nitrides semiconductors, gallium nitride (GaN), aluminium nitride (AlN) and indium nitride (InN), have emerged as promising materials for optoelectronic devices due to their direct bandgaps. Their wide bandgaps and strong bond strength make them ideal to use for violet, blue and green emitting devices and for high temperature transistors [1]. One of the most promising semiconductor is GaN, which has been studied intensively in the last years due to its practical applications in optoelectronic and electronic devices. Some applications of GaN are:

- Light emitting diodes (LEDs) [2, 3].
- Laser diodes (LDs) [4] which are active in the green, blue, ultraviolet wavelengths.
- Detectors [5].

- High temperature/high power electronics [6] due to its high thermal conductivity ($2.0-2.1\,Wcm^{-1}K^{-1}$), wide bandgap energy ($3.4\,eV$), high breakdown field ($\sim 3.3\,MV/cm^{-1}$) and high electron mobility ($\approx 1350\,cm^2V^{-1}s^{-1}$).

The crystalline structure of GaN was first reported by Juza and Hahn [7] in 1938, who produced small needles and platelets with hexagonal structures passing ammonia (NH_4) over hot gallium. In 1969, Maruska and Tietjen [8] reported the deposition of the first large single crystal GaN epitaxial film on sapphire by chemical vapor deposition method. All the GaN films at that time were produced as n-type. The advancements of GaN devices depend on several parameters during the synthesis and fabrication. Device applications of the GaN, LEDs, depend on the formation of $p-n$ junctions, therefore several efforts were made to dope GaN (p-type) and to improve the performance of the devices. Amano et al. [9] doped p-type GaN with magnesium (Mg) using AlN buffer layer on sapphire. Their results were improved by Nakamura [10] using a GaN buffer layer for p-type GaN, with a hole concentration $3 \times 10^{18} cm^{-3}$. These results have been improved using different growth techniques such as molecular beam epitaxy (MBE).

Fabrication of electronic and optoelectronic devices from nitrides alloys (Al, Ga and In) has become important due to their energy bandgap and dielectric constants which depend on the alloy composition. Therefore by using these compounds, the devices can be fabricated emitting from red to ultraviolet wavelength. Ultraviolet light emitting diodes (UV LEDs) are the key devices for several applications such as solid-state lighting, bio-chemical detection, air/water purification and high density data storage [11].

Though GaN based materials have a large density of threading dislocations up to $1 \times 10^{10} cm^{-2}$ [12, 13], the GaN based light emitting devices are far less sensitive to threading dislocation density than other optoelectronic materials. Nevertheless, there are several studies showing that threading dislocations influence the electrical and optical properties, confirming that the dislocation density affects the performance of the GaN based devices [11, 14].

1.2 Structural properties

1.2.1 Wurtzite structure

Group-III nitrides such as GaN, AlN and InN can crystallize as either wurtzite or zincblende structures [15]. At ambient temperature and atmospheric pressure, the thermodymamically stable phase is the wurtzite structure, which consists of two hexagonal close packed sublattices (Ga and N) shifted by $\frac{3}{8}$ (0.375) each other along the polar [0001] axis (Figure 1.1a). Both sublattices are constituted by one atomic species, resulting in four atoms per unit cell. Every atom of one kind is surrounded by four atoms of the other kind which are arranged at the edges of a tetrahedron. Crystals with wurtzite structure belong to the space group of $P6_3mc$ (No. 186). The lattice constants, the internal displacement parameters and thermal expansion coefficients of III-nitrides group are given in Table 1.1.

Parameter	GaN	AlN	InN
Lattice constant (nm)	a=0.319	a=0.3111	a=0.3544
	c=0.518	c=0.4980	c=0.5718
u	0.377	0.382	0.379
Thermal expansion	$a = 5.59 \times 10^{-6}$	$a = 4.15 \times 10^{-6}$	$a = 3.8 \times 10^{-6}$
coefficients (K^{-1})	$c = 3.17 \times 10^{-6}$	$c = 5.27 \times 10^{-6}$	$c = 2.9 \times 10^{-6}$

Table 1.1: *Structural properties for III-nitrides with wurtzite structure.*

The atoms position in the GaN lattice are: Ga-atoms in both (000) and $(\frac{2}{3}, \frac{1}{3}, \frac{1}{2})$, while N-atoms at $(0, 0, u)$ and at $(\frac{2}{3}, \frac{1}{3}, \frac{1}{2} + u)$; where u is the internal displacement parameter, which is defined as anion-cation bond length along [001] direction, u=$\frac{3}{8}$ [16] (Table 1.1). Along the [0001] direction, the hexagonal close packed stacking sequence is $AaBbAaBb...$ where the capital letter corresponds to the cations (Ga^{3+}) and the lower case to anions (N^{3-}) (Figure 1.1b).

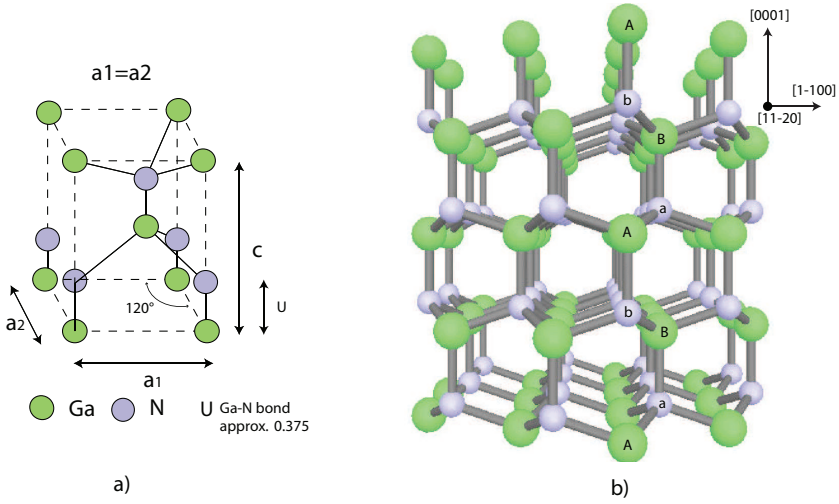

Figure 1.1: *Wurtzite GaN strucuture: a) unit cell which consists in two hexagonal close packed sublattices (Ga and N) where* $a_1 = a_2 \neq c$, $\alpha = \beta \neq \gamma$ *and* u *is the bond between cation and anion* ($u = \frac{3}{8}$). *b)* $[11\bar{2}0]$ *projection of the GaN structure. The stacking sequence AaBbAaBbAaBb.... is given along* [0001] *direction.*

1.2.2 Polarization in wurtzite structure

Group-III nitrides have structures which are highly sensitive to strain and deformation due to the different physical properties (lattice mismatch and thermal expansion coefficient) of the materials constituents, the deformations alter the electronic band structure. This class of materials exhibits polarization effects linked to their symmetry which affects all the crystal properties. The polarization field in c-direction in c-GaN layers is the sum of spontaneous polarization and piezoelectric polarization (macroscopic polarization), it affects the electric and optical properties of devices.

The wurtzite structure is the structure of highest symmetry compatible with the existence of spontaneous polarization [17] along the $c-$[0001] direction. The magnitude of the spontaneous polarization depends on any change in the temperature. For this reason, group-III nitrides belong to the family of pyroelectric materials. Table 1.2 shows the spontaneous polarization (P_{sp}) of group-III nitrides group calculated by Bernardini et al. [18].

Material Polarization $^oC/m^2$	GaN	AlN	InN
P_{sp}	-0.034	-0.090	-0.042
P_{pz}	1.8765	-3.1963	0.4448

Table 1.2: *Spontaneous and piezoelectric polarization for the group-III nitrides ; P_{sp} and $P^o_{pz}C/m^2$ [19] respectively.*

Piezoelectric polarization occurs when the crystal is under stress or deformation i.e. variation of lattice parameters or changes in the anion-cation bond (parameter u), which induces a modification of the whole lattice structure as shown in Figure 1.2.

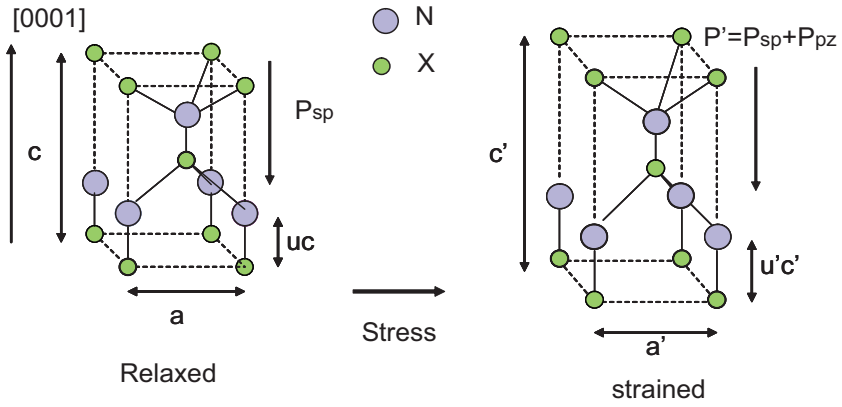

Figure 1.2: *Spontaneous and piezoelectric polarization along* [0001] *direction in wurtzite structure. The lattice parameters change due to the stress induces for the polarization. x is either Ga, Al or In.*

Table 1.2 also shows the piezoelectric polarization of the group-III nitrides. They were calculated using the equations obtained by Fiorentini et al. [19] which are shown in Appendix A.

Piezoelectric polarization strongly affects the performance of light emitting devices based on group-III nitrides. The electric field produces the spatial separation of electron and hole wave functions in Ga-based quantum well structure, high interface charge densities in group-III nitrides [20] and the reduction of the apparent bandgap [21]. The spontaneous polarization is a large internal electric field and affects strongly the bandgap. The total

polarization can influence the radiative recombination in light emitting devices.

Quantum confined Stark effect. — c-plane GaN layers with wurtzite structure suffer of polarization effects along the [0001] direction. This polarization is a large electric field that alters the band structure and produces the so called quantum confined Stark effect (QCSE). QCSE describes the change of the optical properties of quantum wells (QWs) when the electric field is applied perpendicular to the QW layers. The primary effect of QCSE is the shift of the energy levels to lower energy levels as sketched in Figure 1.3 shows the QCSE. The energy of the lowest transition is reduced by the application of an electric field, and the electrons and holes in these states are pulled to opposite side of the well. This effect reduces the emission efficiency in the polar c-GaN [22].

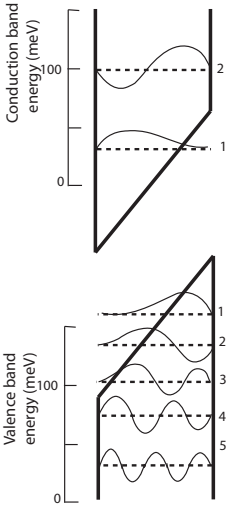

Figure 1.3: *Schematic of the action of an electric field on a quantum well: quantum confined Stark effect.*

1.2.3 Polarity

Group-III nitrides are materials with non-centrosymmetric crystal structure, therefore Ga polar or N polar layers can be grown. GaN with a wurtzite structure has a polar axis parallel to the *c*-direction of the crystal lattice, the sequence of the constituents Ga and N are reversed along the [0001] and [000$\bar{1}$] directions. The corresponding (0001) and (000$\bar{1}$)

faces are called Ga-face and N-face, respectively. The most common direction for growing GaN based materials is normal to the {0001}-basal plane, where the atoms are arranged in bilayers. In GaN, a basal surface should be either Ga- or N-face. Ga-face has Ga on the top position of the {0001} bilayer, corresponding to the [0001] polarity (Figure 1.4). It is important to note that the (0001) and (000$\bar{1}$) surfaces of GaN are not equivalent and differ in their chemical and physical properties [23].

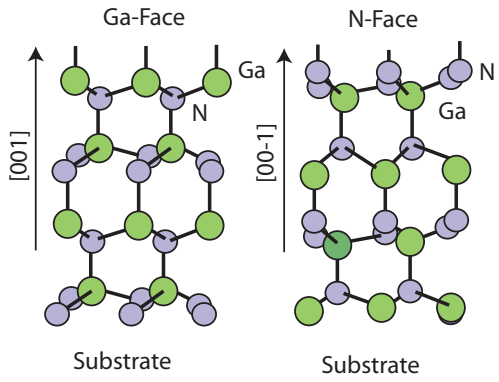

Figure 1.4: *Schematic drawing of the crystal structure of Ga-face and N-face in wurtzite GaN [20].*

Polarity is an important factor for the surface roughness and properties of the material which determines the quality of the material due to the growth technique. GaN can be grown by metal organic chemical vapor deposition (MOCVD) which is typically (0001) plane [24] and with molecular beam epitaxy (MBE) which is either (0001) or (000$\bar{1}$) planes [23]. The nature of the defects is also related to the polarity [25], the density of defects is higher in [000$\bar{1}$] than in [0001] direction.

1.3 Optical properties

The most important property of GaN, AlN and InN is their direct bandgap allowing efficient light emission. The bandgaps of the group-III nitrides are shown in Table 1.3 [1].

[1]The InN bangap does not have a fix number, it has been established between 0.65-0.7 eV

Material	GaN	AlN	InN
band gap (eV)	3.39	6.2	1.89

Table 1.3: *Band gap for the III-IV nitrides group [26]*

Some optical processes in semiconductors are associated with electronic transitions between the band edge of the valence band and the conduction band:

- Direct and indirect interband transitions.
- Intrinsic free excitons and excitons bound impurities.
- Transition related to impurity states associated with the bottom of the conduction band valleys (donors) and with the valence band maxima (acceptors).

The III-nitrides group has a direct bandgap, excellent mechanical properties, great stability and interesting physical properties, therefore, they can be used in a large variety of applications in the future, in addition to the application in light emitting devices. Some applications are: microwave emitter, piezoelectric elements and sensors.

1.3.1 Doping GaN

Doping determines the position of the Fermi level in a semiconductor making the material $n-$type if the Fermi level is close to the conduction band and $p-$type if it is closer to the valence band (Figure 1.5). In these figures, the electron exchange between the allowed bands and the level in the bandgap, the arrows indicate the possible transitions.

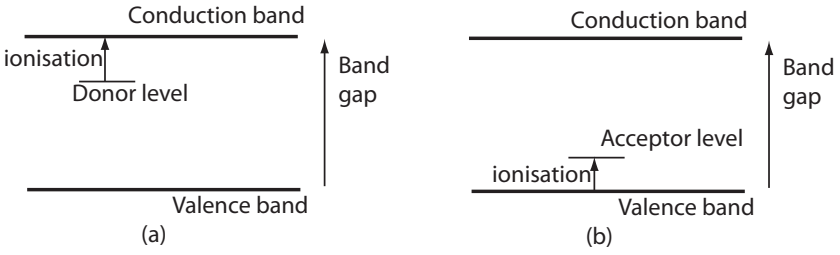

Figure 1.5: *Band diagrams: (a) n− and (b) p− type semiconductor.*

Doping controls the electron ($n-$type) or hole ($p-$type) concentration, and it also affect the mobility of carriers: high doping reduces the mobility. In general, wide bandgap semiconductors are difficult to dope both $n-$ and $p-$ types due to the native defects. Doping is an important parameter in order to improve the electronic properties of the devices.

The $n-$type dopants in GaN are silicon (Si), nitrogen (N), oxigen (O) and germanium (Ge), where the most common is Si. Si and Ge act as a single donor by substituting Ga in the GaN lattice. The elements used for $p-$type dopants are the column II such as zinc (Zn), cadmium (Cd), magnesium (Mg) and berilium (Be) substitutionally for Ga to form a single acceptor.

$p-$type GaN have been grown by MOVPE [27] and NH_3 MBE [28]. By MOVPE, p-GaN layers exhibit good conductivity and high hole concentration ($10^{17} cm^{-3}$). For NH_3 MBE, high quality of Mg-GaN can be achieved with the following characteristics:

- hole concentration $1 \times 10^{18} cm^{-3}$,
- electron mobility 9 cm^2/Vs,
- resistivity 0.75 ω.

The effects due to the piezoelectric and spontaneous polarization fields in Mg-GaN grown on c-direction are attributed to screening of the band bending that results in stronger emission and peak blue shift [29]. Mg in $p-$type GaN tends to diffuse and to accumulate on the surface resulting in more extended defects.

There are few reports for optical and electrical properties for $n-$ and $p-$types a-plane GaN on r-sapphire. Lee et al. [30] have grown a-plane GaN doped with Mg and Si, they believed that the degradation of optical efficiency was due to the crystal imperfections of a-GaN, the intrinsic crystal structure and the additional strain introduced by Si or Mg doping process. The electrons concentration of a-plane n-GaN is slightly lower that of c-plane $n-$GaN, whereas the hole concentration of a-plane p-GaN is higher than that of c-plane p-GaN.

1.4 c-plane GaN vs a-plane GaN

GaN films can grow on substrate materials in several orientations such as c-(0001), m-($1\bar{1}00$) and a-($11\bar{2}0$) planes. Figure 1.6 shows the different orientations of growth of GaN heteroepitaxial films in a hexagonal unit cell.

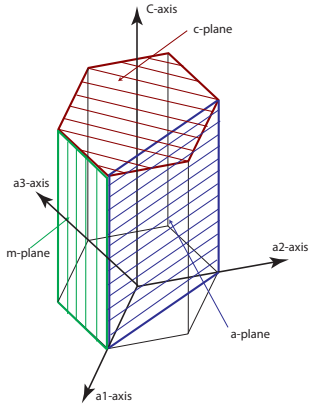

Figure 1.6: *Different orientations used to grow GaN thin films.*

The most common substrate materials to grow GaN epitaxial thin films are: sapphire (Al_2O_3) [31, 32], silicon carbide (SiC) [33], silicon (Si) [31, 34], $GaAs$, lithium gallate ($LiGaO_2$) [35], aluminium nitride (AlN) [36] and $\gamma - LiAlO_2$ [37]. Sapphire and SiC are the most frequently used substrates. Sapphire is preferred to SiC for the heteroepitaxial growth due to its lower cost, the availability of good quality crystals of large size and for the possibility of growing thin films in different orientations.

c-plane GaN is the most common orientation to grow the nitrides for device applications. However, GaN suffers of polarization effects originated from c-[0001] polar axis of the wurtzite structure. One approach to avoid this problem [38] is to grow GaN in non polar structures such as $m-\{1\bar{1}00\}$ [39] and $a-\{11\bar{2}0\}$ [40]. On basis of crystal symmetry, a- or m-planes of oriented films have their polar axis parallel to the surface. Consequently, the heterostructures grown in one of these orientations are free of the polarization effects.

In c-plane GaN films, the quality of the surface is better than in a-plane GaN which is affected by the high density of defects, mainly dislocations and SFs. Thick a-GaN layers can be grown without cracks in comparison of c-plane GaN [41]. The optical properties

of c- and a-planes GaN are similar [42] and the electrical properties of a-plane GaN layers are better [43] than those of c-plane GaN.

1.5 a-plane GaN

In order to avoid polarization effects, GaN layers have been grown in different directions than c-plane, e.i. m- and a-planes. a-plane GaN have been grown for several groups on different substrate materials, such as $r-$ sapphire [44–47], SiC [48], Si [31, 49], $LiAlO_2$ [35, 37, 50] and $4H - SiC$ [33, 51, 52] mainly by using HVPE [53] and MOVPE [54]. r-plane sapphire is the most common substrate used to grow a-plane GaN. Despite the large mismatch and large defect density, a-plane GaN has good material properties and can be used in several applications [2, 3, 43]. However, a-GaN is still studied in order to reduce the defect density and to improve the optical properties.

1.6 Outline of this work

The microstructural characterization of a-GaN on r-sapphire grown by HVPE-ELO is the continuation of a previous work. The material studied in that work was c-GaN layers grown by HVPE-ELO [55]. Since the optical properties in c-GaN are affected by the polarization effects, the non-polar directions have been chosen in order to improve them. In the last years, there has been a considerable interest in the study of $a-(11\bar{2}0)$ plane GaN layers grown on r-$(1\bar{1}02)$ plane sapphire. a-GaN layer on sapphire has a large mismatch, therefore, a high defect density (threading dislocations and stacking faults) is originated at their interface. These defects impair the properties of the material and limit the device applications.

The aim of this work is the study of microstructural characterization of a-plane GaN thick films grown on r-plane sapphire by HVPE-ELO using transmission electron microscopy. It includes the identification and the characterization of structural defects originated during

the growth and its relation with the optical properties. a-GaN layers are normally grown by MOCVD in order to obtain a high thin film quality. In this work, HVPE is used in order to obtain thick a-GaN layers without cracks which can be used as substrate materials to grow homoepitaxial GaN. ELO is implemented in order to reduce the defect density and hence, improving the optical properties.

A detailed study of the structural defects has to be carried out since new defects are created in a-GaN layers that in c-GaN layers do not have, such as basal stacking faults. The identification of these defects and their behavior on the optical properties must be analyzed to identify which kind of defect affects the optical properties. In this way, the results will provide guidelines to improve the quality of the a-GaN analyzing the growth process.

This work is organized in the following chapters:

Chapter 2 describes the techniques related to the electron microscopy, the characterization and the sample preparation.

A brief introduction to epitaxial growth in GaN is given in Chapter 3, where the differences between *c*- and *a*-planes GaN are emphasized. It also contains, an introduction of defects such as dislocations and stacking faults in hexagonal crystals mainly with wurtzite structure, and a brief review of structural defects produced during the growth in the a-GaN thin films using ELO.

Chapter 4 discusses the structural characterization of defects in a-GaN thin films grown on r-sapphire obtained in this work. The relation between these defects and the optical properties is given using cathodoluminescence and microphotoluminescence experiments. It also contains a characterization of a $Al_{1-x}Ga_xN/GaN/Al_{1-x}Ga_xN$ single quantum well growth in a-GaN template by MBE.

Finally, Chapter 5 summarizes this work and gives some perspectives to improve the optical qualityt of the a-GaN thick films grown by HVPE-ELO.

Chapter 2

Electron Microscopy

The different electron microscopy techniques used to characterize the a-plane GaN growth on r-plane sapphire are described in this chapter. Transmission electron microscopy (TEM) and high resolution transmission electron microscopy (HRTEM), are tools for defect identification at low magnification and atomic scales, respectively. Bright field (BF), dark field (DF) and weak beam (WB) techniques are used as tools for the identification of perfect, partial dislocations and stacking faults. A short description of cathodoluminescence and μ-photoluminescence techniques are given. Practical methods for the identification of the Burgers vector of dislocations, identification of the displacement vector of the stacking faults and the determination of the dislocation density, are described. Also, in this chapter, the description of the specimen preparation of thin films is given.

2.1 Electron matter interaction

Electrons are generated by an electron gun (thermionic or field emission), and are accelerated through an electrostatic field towards the specimen. When the electron beam reaches the thin specimen, it interacts with the specimen, producing several secondary signals (Figure 2.1) such as secondary electrons (SE), backscattered electrons (BSE), auger electrons (AE), X rays (XR), cathodoluminescence (CL), transmitted electrons, and inelastically and elastically scattered electrons. These signals can be employed to

form images (BF, DF, HRTEM), diffraction patterns, and are used to perform various spectroscopies (EDS, EELS, CL).

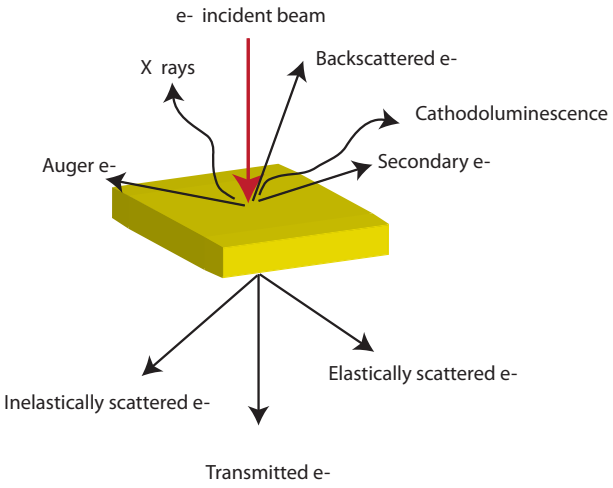

Figure 2.1: *Signals generated by the interaction of the electron beam with the specimen.*

The electrons that are elastically scattered are the major source for image contrast in TEM techniques such as bright and dark field TEM, and HRTEM. The inelastically scattered electrons are used for analytical electron microscopy, such as electron energy loss spectroscopy (EELS), x-ray microanalysis and catholuminescence analysis.

2.2 Transmission Electron Microscope

TEM is a successful and efficient tool for the characterization of crystalline structures. In contrast with SEM, it uses higher electron energies (100-400 kV), and the specimen must be electron transparent. TEM instruments have three essential components:

1. The illumination system, which consists of an electron gun, producing the electron beam, and a condenser system, focusing the beam onto the specimen.

2. The image-producing system, which consists of the objective lens, the movable specimen stage, and the intermediate and projector lenses group, and it focuses the electrons passing through the specimen in a real, highly magnified image.

3. The image-recording system, which converts the electron image into a perceptible to the human eye form. It usually consists of a fluorescent screen for viewing and focusing the image, and a camera for permanent recording.

The illumination system can be operated in two principal modes: parallel beam and convergent beam. The first mode is used in TEM for imaging and SAED diffraction, while the second is used in the scanning transmission electron microscope (STEM). The TEM imaging system changes depending on the mode of operation; either imaging or diffraction (Figure 2.2). In diffraction mode (Figure 2.2a), the imaging system lenses are adjusted so that the back focal plane of the objective lens acts as the object plane for the intermediate lens; therefore the diffracted pattern is projected onto the screen. In the imaging mode (Figure 2.2b), the intermediate lens is readjusted so that its object and image planes are conjugate planes of the object lens and the image is projected onto the screen.

The TEM analysis in this work was performed at Centre Interdisciplinaire de Microscopie Electronique (CIME) using a Philips CM20 TEM operating at 200 kV and a Philips CM300-FEG TEM operating at 300 kV.

2.3 Electron diffraction and defect imaging

The contrast details of the TEM images are determined by the intensity of the electron beams, which varies depending on the positions in the image. In order to understand the contrast features of TEM images, the intensity of the transmitted and diffracted beams at the exit surface of the specimen have to be calculated. The intensity can be calculated by Howie-Whelan theory which uses the two beams approximation. For a perfect and imperfect crystal, this theory is given in the Appendix B.

For this theory, the direction of the diffracted beam with respect to the incident beam ($\vec{g}$) is important. The wave vectors $\vec{k_0}$ and $\vec{k}$ of the incident and diffracted beams satisfy the

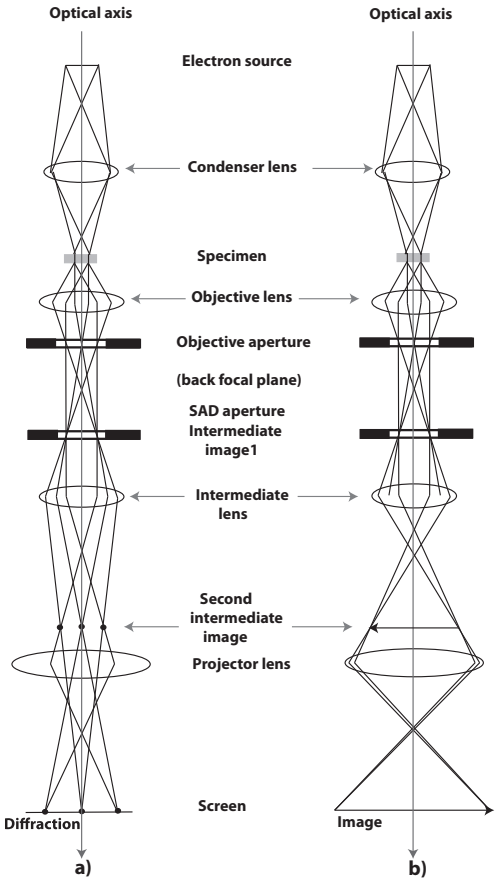

Figure 2.2: *Ray paths in the electron microscope: a) diffraction mode and b) imaging mode of TEM.*

Bragg law.

$$\vec{k} - \vec{k_0} = \vec{g} \tag{2.1}$$

where $\vec{g}$ is the reciprocal lattice vector, which is given by

$$\vec{g}_{hkl} = ha^* + kb^* + lc^* \tag{2.2}$$

where $\vec{g}_{(hkl)}$ is normal to the crystal reflecting (hkl) plane, and its length is $|g| = \frac{1}{d_{hkl}}$, where d_{hkl} is the spacing of $\{hkl\}$planes.

The Bragg law can be interpreted with the help of the Ewald sphere (Figure 2.3). Consider a crystal (C) with one (hkl) reflecting plane (G) at the correct Bragg angle. Then, draw a sphere with radius $1/\lambda$. The wave vectors k_0 and k of the incident and scattered beams satisfy the Bragg law with a length $1/\lambda$. Any point on the sphere represents the endpoint

of the vector k of a possible scattered wave.

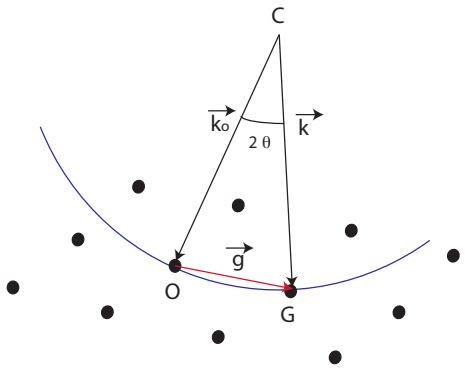

Figure 2.3: *Reflecting/Ewald sphere construction*

Bragg law states (Figure 2.3):

If C is the center of the sphere and if $\vec{CO} = \vec{k_o}$ (O is the origin of the reciprocal lattice) and $\vec{CG} = \vec{k}$ is a wave vector of the diffracted beam lying in the Ewald sphere

$$\vec{OG} = \vec{k} - \vec{k_o} = \vec{g_{hkl}} \tag{2.3}$$

In the elastic scattering, we have $|\vec{k}|=|\vec{k_o}|=|\vec{k_o} + \vec{g}|$

$$\begin{aligned} |\vec{k_o}|^2 = |\vec{k_o} + \vec{g}|^2 &= k_o^2 + 2k_o g + g^2 \\ 2k_o cos(90 - \theta_B) &= -g \\ 2k_o sin\theta_B &= g \end{aligned} \tag{2.4}$$

where $|g| = \frac{1}{d_{hkl}}$ and $k_o = \frac{1}{\lambda}$. Thus, the Bragg's law results in:

$$2\, d_{hkl}\, Sin\, \theta_B = \lambda \tag{2.5}$$

2.3.1 Contrast from dislocations

Dislocations can be characterized by their displacement vector ($\vec{R}$) and dislocation line ($\vec{u}$). $\vec{R}$ depends on the dislocation character, which can be screw, edge or mixed.

Making use of isotropic elasticity theory, the displacements field $\vec{R}$ of a dislocation depends on its character [56]:

Screw — The screw dislocations can be characterized by the fault where the dislocation line is parallel to its Burgers vector ($\vec{b}$) so that $\vec{b}.\vec{u} = 0$. The displacement vector $\vec{R}$ is given by

$$\vec{R} = \vec{b}\frac{\theta}{2\pi} = \frac{\vec{b}}{2\pi}\tan^{-1}\frac{y}{x} \tag{2.6}$$

where x and y are coordinates perpendicular to the dislocation line $\vec{u}$ (along z).

Edge — For an edge dislocation, there are two displacement components, one parallel to $\vec{b}$ ($\vec{R_1}$) and the other normal to the slip plane ($\vec{R_2}$)

$$\vec{R_1} = \frac{\vec{b}}{2\pi}[tan^{-1}\frac{y}{x} + \frac{xy}{2(1-\nu)(x^2+y^2)}] \tag{2.7}$$

and

$$\vec{R_2} = \frac{\vec{b}}{2\pi}[\frac{1-2\nu}{4(1-\nu)}\,In(x^2+y^2) + \frac{x^2-y^2}{4(1-\nu)(x^2+y^2)}] \tag{2.8}$$

Theoretically, a screw dislocation is invisible when $\vec{g}.\vec{b} = 0$, whereas an edge dislocation is invisible when $\vec{g}.\vec{b} = 0$ and $\vec{g}.\vec{b}\wedge\vec{u} = 0$. In practice, it is not possible for "$\vec{g}.\vec{b}\wedge\vec{u}$" to be zero; however it can be small enough to be considered zero. Specifically, the dislocation is considered invisible if the parameter $\vec{g}.\vec{b}\wedge\vec{u} \leq 0.08$ [57]. These conditions are known as the invisibility criterion.

Mixed — When a dislocation is neither pure screw nor pure edge, it is defined to be a mixed dislocation. The mixed dislocation displacement $\vec{R}$ is obtained by the combination of the screw and the edge displacement. The $\vec{R}$ of a general or a mixed dislocation is given by:

$$\vec{R} = \frac{1}{2\pi}(\vec{b}\,\phi) + \frac{1}{4(1-\nu)}\{\vec{b_e} + \vec{b}\times\vec{u}\,(2(1-2\nu)\,\ln r + \cos 2\phi)\} \tag{2.9}$$

$\vec{R}$ is given in polar coordinates (r and ϕ), $\vec{b}$ is the Burgers vector; $\vec{b_e}$ is the edge component of the Burgers vector; $\vec{u}$ unit vector along the dislocation line and ν is the Poisson's ratio.

Determination of the Burgers vector — For the interpretation of the dislocations images, it is important to know the magnitude and direction of the Burgers vector ($\vec{b}$). For screw and edge dislocations, the Burgers vector is parallel and normal to the dislocation line $\vec{u}$, respectively.

For the determination of $\vec{b}$, the two beam condition is used with different reflections ($\vec{g}$). The direction of $\vec{b}$ can be obtained using two non parallel reflection ($\vec{b} = \vec{g_1} \times \vec{g_2}$), where in these reflections the dislocations are out of contrast.

The identification of partial dislocations is more difficult because they are associated with stacking faults and give contrast under many diffracting conditions. Using the invisibility criterion, they can become invisible when either $\vec{g}.\vec{b} = 0$ or $\vec{g}.\vec{b} = \pm\frac{1}{3}$ [57, 58].

Isotropic theory cannot be used for the identification of the Burgers vector and the calculation of the displacement vector of dislocations in hexagonal crystals such as the GaN studied here. They are instead treated on the basis of the anisotropic theory [59]. In anisotropic crystals, many dislocations do not have a perfect edge or screw character. The dislocations do not have zero contrast when $\vec{g}.\vec{b} = 0$; instead, small residual contrast exist that can be interpreted analogously to $\vec{g}.\vec{b} = 0$. Typically, such mixed dislocations have a Burgers vector which has a component along the c axis. In that do not have any component in the c-axis (i.e they are in the basal plane) do have zero contrast when $\vec{g}.\vec{b} = 0$. In others words, isotropic theory can be applied to dislocations in the basal plane.

Determination of dislocation density — Dislocation density was determined using bright field two beam condition images. A grid consisting of three horizontal and vertical lines was superposed on such images. The total length of the lines is known (L). The number of intersections (N) between the grid lines and the dislocation lines were then counted. The dislocation density is then given by [57]:

$$\Lambda = \frac{2N}{Lt} \tag{2.10}$$

where t is the thickness of the foil which was measured by TEM, typically 200<t<400 nm. For example, figure 2.4 shows a bright field micrograph of the lateral overgrown area under $g = (1\bar{2}10)$ diffraction condition. Two grids (1 and 2) were superposed on the micrograph with L=6 μm, the number of intersections (N) are 11 and 10 respectively and the thickness T= 350 nm, which was obtained using the thickness fringes. In grid *1* the dislocation density Λ is 1.21×10^9 cm^{-2} and in grid *2* is 1.1×10^9 cm^{-2}. This method can be used for densities up $10^{11} - 10^{12}\, cm^{-2}$. The error has been reported to be $\approx 20\%$ [57, 60]

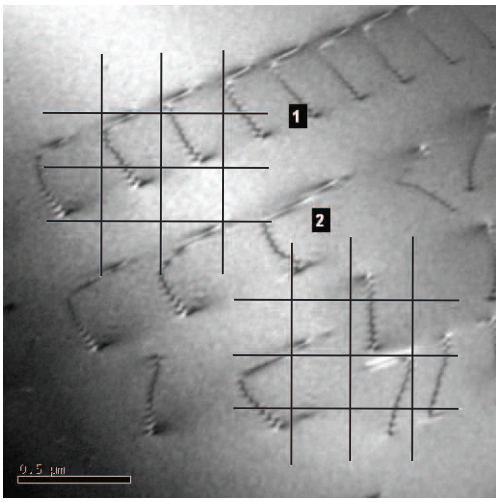

Figure 2.4: *Dislocation density measurements.*

2.3.2 Stacking faults

Stacking fault contrast takes the form of a series of dark and bright fringes, parallel to the line of the intersertion of the foil surface and the plane of the fault. The invisibility criterion is also used for SF analysis. In this case, the phase factor $\alpha = 2\pi\vec{g}.\vec{R}$ determines the invisibility criterion where $\vec{R}$ is the fault vector and $\vec{g}$ is the operating reflection of the two beam condition. The fault contrast occurs when $2\pi\vec{g}.\vec{R} \neq integer$; faults are out of contrast not only when $2\pi\vec{g}.\vec{R} = 0$ but also when $2\pi\vec{g}.\vec{R} = integer$.

Bright and dark micrographs under $\vec{g} = (01\bar{1}0)$ and $[\bar{2}110]$ zone axis were used to obtain the SF density. Densities were calculated by the number of intersections (N) along a line of known length (SF density=N/L).

2.4 Bright field and dark field image

Bright field (BF) and dark field (DF) imaging are used to form images from the transmitted beam or a diffracted beam. The objective aperture is inserted in the back focal plane of the objective lens to select one beam; and the non-selected reflections are absorbed (by the aperture). When the transmitted beam is selected by the aperture, as shown in Figure 2.5a, a BF image is obtained. When a diffracted beam is selected, a DF image is formed (Figure 2.5b). DF images are usually obtained by tilting the incident beam in order to have the diffracted beam on the optical axis, thus minimizing aberrations.

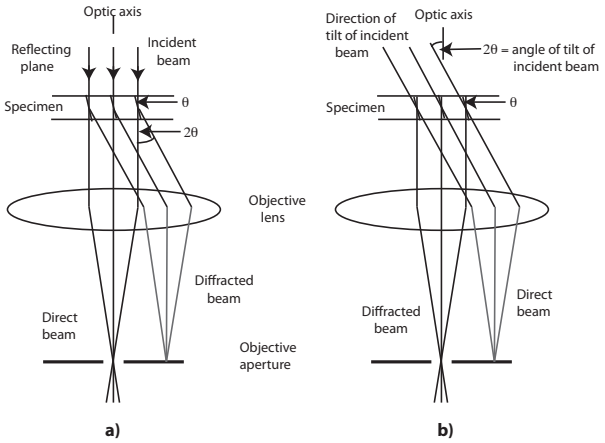

Figure 2.5: *Ray diagrams for a) BF image and b) DF image*

2.5 Two beam condition

In order to obtain a strong diffraction contrast in both BF and DF images, the specimen has to be tilted far away from the zone axis. The two beam condition is realized when only the transmitted beam and one diffracted beam are intense. Different images can be taken by selecting different $\vec{g}$ vectors for defect analysis.

Figure 2.6 shows the procedure to follow for obtaining the two beam condition. First, the identification of the zone axis is indispensable in order to know which $\vec{g}$ will be selected for DF images. With the help of the Kikuchi lines, the specimen is tilted until two

beam condition is reached. Then the objective aperture is inserted and centered around the transmitted beam, and a BF image is taken. Finally to obtain the DF image, the diffracted beam is tilted until it is centered in the aperture, as shown in Section 2.4.

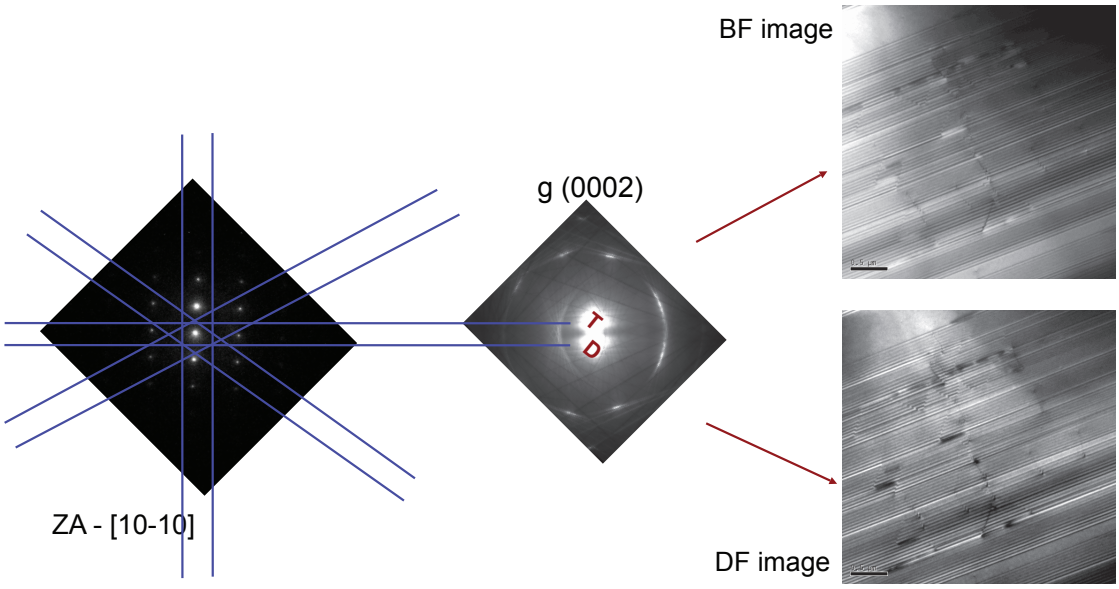

Figure 2.6: *Two beam conditions; the beam is tilted with the help of the Kikuchi lines until a two beam condition is set up, the transmitted beam (T) is used for BF image and the diffracted beam (D) for DF image. BF and DF images are complementary.*

The different reflections used in the defect analysis are shown in Figure 2.7. It shows the Kikuchi orientation map of GaN, which contains the different zone axes and the reflections used for the analysis. The Kikuchi map can be used to understand how the sample is tilted in order to have a desirable reflection.

2.6 Weak beam

The weak beam (WB) method was introduced in 1969 by Cockayne et al. [61] as an experimental method for studying individual lattice defects in the resolution range 2-10 nm. The image shows details of defects that normally used strong beams do not show, since the technique is sensitive to local displacement field. WB is mainly a technique employed to

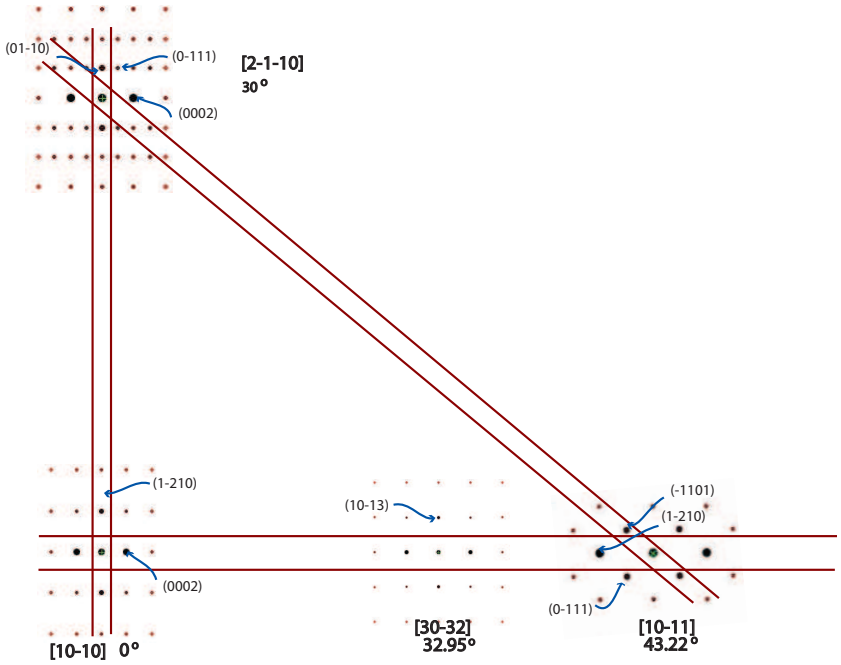

Figure 2.7: *Kikuchi map of GaN with the zone axes and reflections used for the analysis of dislocations.*

determine the stacking fault energy (γ), the closely spaced partial dislocations, the study of defects in semiconductors, the dissociation of perfect dislocations, jogs, interfaces and grain boundaries [62].

The steps necessary to form WB images are illustrated in Figure 2.8 using the help of the Ewald sphere and the Kikuchi lines in the BF and DF. In BF, the orientation of the specimen is set such that the $\vec{g}$ reflection satisfies the Bragg condition $s = 0$ (full lines), the Kikuchi lines pass through 0 and $\vec{g}$ as shown in Figure 2.8*a*. In WB-DF, the reflection $\vec{g}$ is tilted to the optic axis, and the objective aperture selects $\vec{g}$. The $\vec{g}$ reflection becomes very weak because in this orientation the crystal scatters only weakly in its direction. Instead, the $3g$ reflection is strong, since it satisfies the Bragg condition (dashed lines), $s_{3g} = 0$, as shown in Figure 2.8*b*. However using the weak $\vec{g}$ reflection, some defects can be resolved due to the local displacement field.

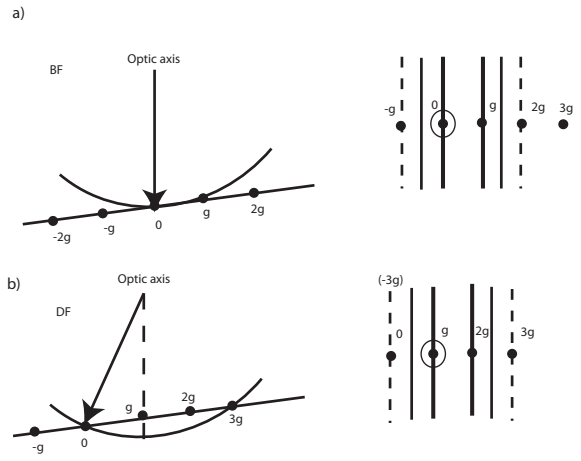

Figure 2.8: *Weak beam in the Ewald sphere scheme and Kikuchi lines scheme: a) BF when $s = 0$ and b) DF when $s_{3g} = 0$.*

2.7 High resolution electron microscopy

High resolution electron microscopy (HRTEM) is a powerful technique that is capable of providing image information at atomic resolution. It provides information in real space of the structural crystalline defects, such as dislocations, interfaces, etc. The contrast in high resolution is formed due to the interference of the transmitted and diffracted beams; it is called phase contrast. The Abbe theory of image formation for a crystalline material is described in Appendix C.

Figure 2.9 shows HRTEM images and their Fourier transforms of a-plane GaN taken under different diffraction conditions. The incident beam in Figure 4.41(a) is parallel to the $[10\bar{1}0]$ zone axis and in Figure 2.9(b) is parallel to the $[2\bar{1}\bar{1}0]$ zone axis. The atomic arrangement of the GaN and the lattice fringes spacing in the images are different. This technique can be used as a tool to complement the defect analysis.

2.8 Optical Characterization

The optical properties are studied in order to know the quality of the material, i.e. the behavior of the structural defects. For the analysis of the optical properties two tech-

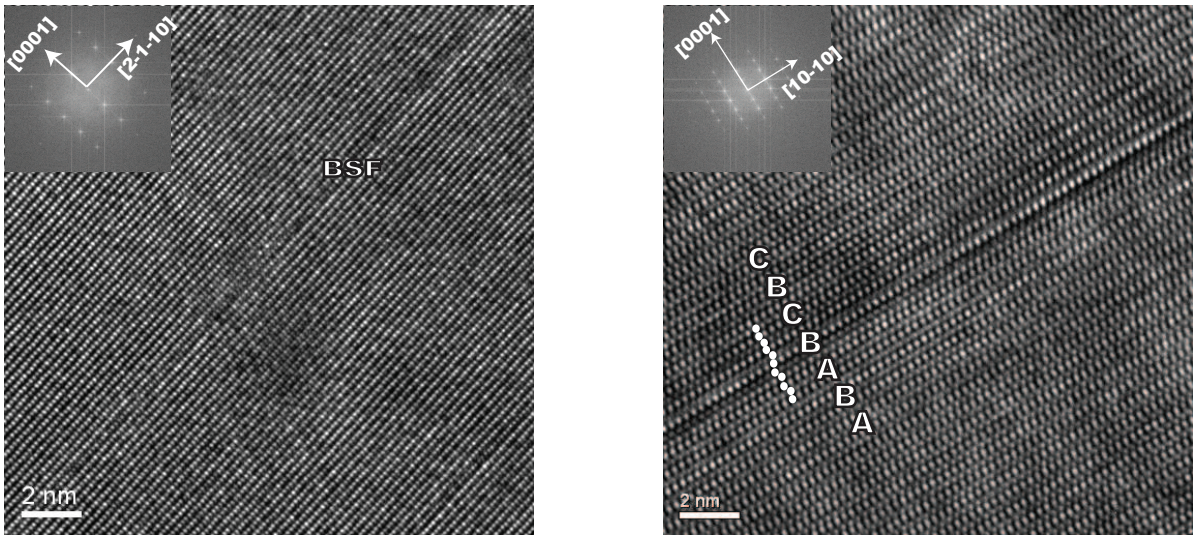

(a) (b)

Figure 2.9: *HRTEM images of the a-plane GaN/r-plane sapphire taken with different zone axes: a)* $[10\bar{1}0]$ *Zone axis and b)* $[2\bar{1}\bar{1}0]$ *zone axis.*

niques were used: cathodoluminescence (CL) in SEM and micro-photoluminescence (μ-PL).

2.8.1 Cathodoluminescence

When an electron beam interacts with a specimen many signals are generated (Section 2.1). One of the inelastic scattering signals is cathodoluminescence.

The cathodoluminescence in a semiconductor material is described in terms of recombination of electron-hole pairs. It involves transitions between states in the conduction (empty) or valence (filled) bands with those in the bandgap of the material by donors and acceptors. The transitions that lead to emission in semiconductor are shown in Figure 2.10. The cathodoluminescence emission spectra can be divided in to intrinsic or edge emission and extrinsic or characteristic emission.

Intrinsic emission is created by the recombination of electron and holes across the energy bandgap. Energy and momentum must be conserved during these transitions. This is

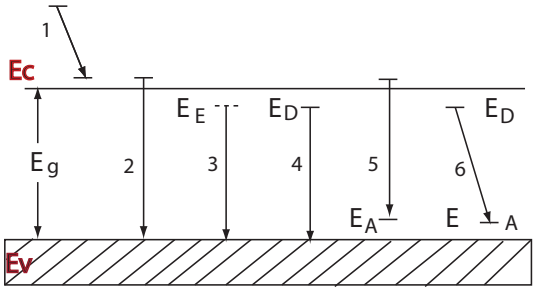

Figure 2.10: *Schematic diagram of reactive transitions between the conduction band (Ec), the valence band (Ev) and exciton (E_E), donor(E_D) and acceptor (E_A) levels in a semiconductor [63]. 1) thermalization process, 2) intrinsic emission, 3) exciton decay, 4)donor-to free-hole transition, 5) free-electron-to-acceptor transition and 6) donor-acceptor pair.*

when the maximum of the valence band and minimum of the conduction band occur at the same value of the wave vector **k**. The emission spectra, which depend on the presence of impurities, are extrinsic in nature. The emission band is activated by impurity atoms or other defects, and the emission features are characteristic of the particular activator.

Cathodoluminescence measurements. — This technique was carried out at the Paul Drude institute in Berlin using a scanning electron microscope operated at 10 kV beam energy on an electron transparent TEM sample held $\approx 5^o$K. This technique helps us to understand how defects affect the optical properties, because the concentration and distribution of photon emission can be correlated with the concentration and distribution of defects determined by the TEM studies.

In cathodoluminescence (Figure 2.11), the electrons are produced by the electron beam. Two condenser and one objective lenses are used to produce a fine electron beam that is focused onto the specimen surface. Scan coils deflect the beam so that the electron spot scans line by line, in a square raster over the specimen surface. The specimen holder is cooled at helium liquid temperature. When the electron beam impinges on the sample, it induces phonon emission from a localized area. The photons are collected by an elliptical mirror and are transferred by a light guide out of the microscope to the CL detection

system. The photons are analyzed in frequency by a monochromator and detected with a photomultiplier. Parallel detection is achieved using a Peltier cooled CCD camera.

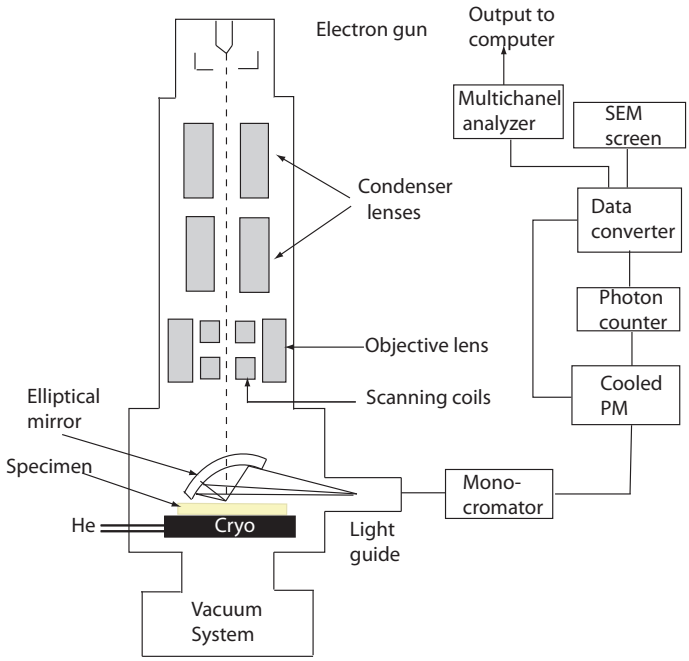

Figure 2.11: *Schematic diagram showing the basic component of a SEM instrument and a typical CL detection system.*

μ-Photoluminescence (PL) measurements. — Photoluminescence is the spontaneous emission of photons from a material under optical excitation. A laser with a particular wavelength is directed onto the sample and absorbed by the sample material, where by a process called photoexcitation occurs. The photoexcitation causes the material to move to a higher electronic state. It then releases energy (photons), as it relaxes and returns back to a lower energy level. The emission of light or luminescence through this process is called photoluminescence.

The PL measurements of a-GaN samples were carried out in collaboration with LASPE. this measurements were used to analyze how defects affect the optical properties. A low-temperature (LT) UV-μ-photoluminescence equipment with spacial and spectral resolutions of 250 and 0.012 nm, respectively, was used.

2.9 TEM specimen preparation

The sample preparation is an important prerequisite for TEM observations, because the specimens have to be transparent to the electron beam. As a result of the strong electron matter interaction, the specimen must be made extremely thin. There are several procedures for preparing specimens for TEM.

TEM cross sectional ($[10\bar{1}0]$ and [0001] GaN) and plan-view samples were prepared for this work. Their preparation can be divided in to three parts: *a*) preparation of a disc, *b*) disc grinding and polishing and *c*) ion milling.

Preparation of a disc — The GaN layer has a thickness of the order of 20 microns when grown using ELO. The SiO_2 stripes are aligned in the $< 1\bar{1}00 >$ direction in GaN film. For cross sectional samples, the material was cut perpendicularly to the stripes in 2 mm wide slices using a diamond saw (Figure 2.12a). As the thickness of the GaN layer is small, two parts of the sample were sandwiched together in order to protect the layers and bonded using $G1$ epoxy (Figure 2.12b). Then, the sandwich was put into an arcap and the remaining cavity of the arcap was filled with $G1$ epoxy. Finally, slices 600 μm in thickness were cut from the arcap.(Figure 2.12c).

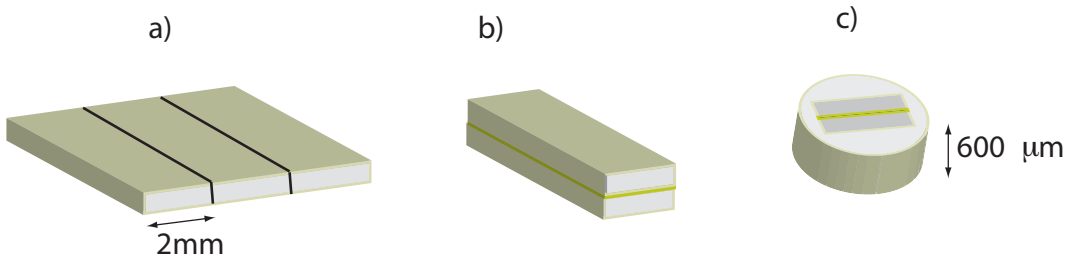

Figure 2.12: *Specimen disc preparation*

Disk grinding and polishing — The 600 μm thick disc is mechanically ground down, from both sides, to 80-100 μm thickness using diamond paper from 15 μm to 0.5 μm (Figure 2.13a and b). One side is ground and polished by a commercial dimple machine

(Gatan: Dimpler Grinder) until we obtain a sample with a thickness between 20-30 μm (Figure 2.13c).

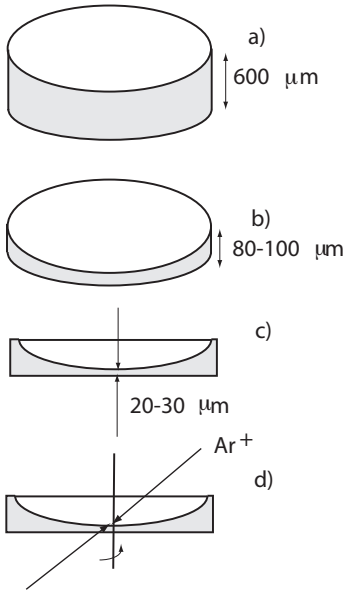

Figure 2.13: *Preparation of the disk: a) 600 µm disc, b) disc grinding, c) disc dimple and d) ion milling.*

Ion milling — TEM samples are ion milled until they have an electron transparent area (Figure 2.13d). The samples were bombarded in the ion milling machine (Gatan:Precision Ion Polishing System) using Ar^+ ions under an accelerating voltage between 2 and 3 kV. The samples were cleaned using 2 kV in order to remove the amorphous layers produced during the bombardment.

Chapter 3

Epitaxial Growth

This chapter presents an overview of homoepitaxial and heteroepitaxial growth of GaN, some information about sapphire (Al_2O_3), which is the most common substrate material used for the growth of GaN thin films and a general description of the MOVPE, MBE and HVPE growth methods. In HVPE and MBE growth method sections, the a-plane GaN samples used in this work are described. Moreover, a review of the heteroepitaxial growth in *a*- and *c*-plane GaN on *r*- and *c*-plane sapphire is provided. During the heteroepitaxial growth, different defects are formed in the GaN thin films, mostly at the GaN/sapphire interface. Finally, this chapter relates the principal defects occurring during the epitaxial growth of GaN using ELO.

3.1 Epitaxial growth

The characteristics of epitaxial GaN layers differ depending on the epitaxial growth mode, homoepitaxial or heteroepitaxial growth. The quality of the epitaxial GaN layers depends on the growth technique, the substrate and the processing conditions.

3.1.1 Homoepitaxial growth

The GaN films are of better quality when they are obtained by homoepitaxial growth rather than heteroepitaxial. The first homoepitaxial GaN layer was grown using metal organic vapor phase epitaxy (MOVPE) by Detchprohm et al. [64], and demonstrated a high crystal quality and good surface morphology.

MOVPE [65–67], molecular beam epitaxy (MBE) [66, 68] and HVPE [67] have been successfully used to grow GaN homoepitaxial layers. Homoepitaxial GaN layers have excellent optical properties due to their low dislocation density [65]. Unfortunately, GaN substrates are not large enough to produce GaN homoepitaxial films for device fabrication.

3.1.2 Heteroepitaxial growth

GaN layers are grown by heteroepitaxy that is on foreign substrates, because there is no GaN bulk single crystal available of diameter $d > 1cm^2$. The substrate properties determine the crystal orientation, polarity, surface morphology, strain, and defect concentration in the GaN layer and thus, the quality of the GaN layer. Growth on a foreign substrate leads to the presence of strain in the layers due to the difference between the lattice parameters and thermal expansion coefficients of the substrate and GaN layer. Therefore, high defect density is obtained in the layer. Heteroepitaxial GaN layers have been grown mainly by MOVPE [43], HVPE [69] and MBE [42].

Nucleation and growth of the thin films occur due to different mechanisms. Depending on both the interaction energy and the structural layer-substrate relation (adhesion and surface energy) . They can be classified as:

- Island growth (Volmer-Weber), which is also called three dimensional growth (3D). This growth occurs when the deposited atoms are more strongly bound to each other than they are to the substrate, small clusters are nucleated on the substrate and grow into islands, which in turn coalesce to form a continuous film.
- Layer by layer growth (Frank van der Merwe), which is also called two dimensional

growth (2D). It occurs when the atoms of the film are more strongly attracted to the substrate than they are to each other, and they form initially a monolayer.

- Growth via the layer by layer followed by island growth (Stranski-Krastanov). It occurs when the initial layer, growing on the substrate, tries to fit the substrate as closely as possible straining itself until the strain energy increases beyond a certain critical value as the layer thickness increases. At the critical thickness the island growth becomes energetically favorable.

The most common method to grow GaN films on sapphire is to utilize the layer by layer growth (2D), and island growth followed with layer by layer growth ($3D \rightarrow 2D$) [70, 71]. The 3D growth is used as a nucleation layer that improves the surface morphology reducing the dislocation density buffer layer [72]. The nucleation layer is commonly grown by MOCVD at low temperature in order to improve the quality of the layer [73]. Large islands are required in the nucleation layer in order to reduce the dislocation density [74], because the dislocations are created during the coalescence of the islands as suggested by Nigth et al. [75]. They showed that threading dislocations are formed during the coalescence of GaN islands which have small misorientations relative to the sapphire substrate. The dislocation density increases abruptly when the thickness of the layer is larger that the critical thickness. Olivier et al. [70] described the 2D and $3D \rightarrow 2D$ growths in GaN films, the 2D growth mode results with a high dislocation density ($5 \times 10^9\, cm^{-2}$), and the $3D \rightarrow 2D$growth mode allows a reduction of threading dislocation density ($1.1 \times 10^8\, cm^{-2}$).

Defects can be originated during the deposition of the buffer layer on sapphire by:

- Substrate surface damage and impurities (nitridation). Due to these imperfections and impurities basal stacking faults are created at the GaN/sapphire interface.

- Thermal stress due to the cooling at the end of the growth process. Because the thermal expansion coefficients of sapphire are larger of those of GaN, the lattice of the sapphire contracts more than that of the GaN during the cooling. Therefore, a compressive stress exists in the GaN layers. This stress contributes an increase of the dislocation density.

- Lattice mismatch induces high dislocation density. This mismatch between the GaN and sapphire decreases through the generation of crystalline defects such as dislocations, stacking faults, cracks, etc. If the layer thickness is larger than the critical thickness, the defect density at the interface increases abruptly.

3.1.3 Substrates for GaN thin films

GaN films have been grown on several substrates such as sapphire (Al_2O_3) [31,32], silicon carbide (SiC) [33], silicon (Si) [31, 34], $GaAs$, lithium gallate ($LiGaO_2$) [35] and $\gamma - LiAlO_2$ [37]. The most popular and widely used substrates are sapphire and SiC.

Sapphire ($\mathbf{Al_2O_3}$) — Sapphire, single Al_2O_3 crystal, has the space group $R\bar{3}c$ ($no.163$). Some important properties of sapphire such as lattice constants and thermal expansion coefficients are given in Table 3.1. The sapphire lattice can be described by a rhombohedral or hexagonal unit cell. The hexagonal unit cell consist of 12 Al^{3+} and 18 O^{2-} ions, which means 30 ions in total.

Property	Value	Reference
Structure	Rhombohedral or hexagonal	
Lattice constant (nm)	a=0.4765 c=1.2982	[76]
Thermal expansion coefficient (K^{-1})	$a = 7.5 \times 10^{-6}$ $c = 8.5 \times 10^{-6}$	[16]
Thermal expansion coefficient (K^{-1})	$a = 5.0 \times 10^{-6}$ $c = 6.7 \times 10^{-6}$	[77]

Table 3.1: *Sapphire properties. Different thermal expansion coefficients are given in the literature and information provided by Crystal-GmbH [77].*

Sapphire presents several orientations favorable to use as a substrate. These orientations

are c-(0001), m-(1$\bar{1}$00), (11$\bar{2}$0)a- and (1$\bar{1}$02)r- planes [31, 32, 78]. c-plane sapphire is the most common orientation for GaN epitaxy.

3.2 Growth techniques

Different techniques are used to grow GaN thin films on substrate materials. The MOVPE, HVPE and MBE techniques are described in the following paragraphs.

3.2.1 MOVPE

MOVPE is the main technique used to grow epitaxial layers and to develop semiconductor devices based on GaN. With MOVPE, the deposition of GaN is possible over a wide range of conditions at $\approx 800°C$. The growth rate increases when the V/III ratio increases. The formation reaction for nitride compounds is given by Equation 3.1 [79]:

$$III(g) + \frac{3}{2}NH_{3(g)} \rightarrow III - N(s) + \frac{3}{2}H_{2(g)} \tag{3.1}$$

where III is the element of the III-nitrides group.

The heteroepitaxial GaN layers grown on sapphire by MOVPE have a huge density of dislocations ($\approx 10^{10}\, cm^{-2}$ [12]), allowing the fabrication of the highly efficient optoelectronic devices. MOVPE low temperature deposition layer is used as nucleation layer to improve the quality of the layer and to get a sharp interface. However, the high temperature of deposition introduces thermal stresses and defect accumulation at the interface [80]. Films grown by MOVPE-ELO have good quality even at high growth rates, thus they are used to fabricate LEDs and LDs [81].

3.2.2 HVPE

HVPE was the earliest method developed to produce GaN epitaxial layers. It is a successful technique which has been used to grow thick layers without too many defects at

high growth rates ($30 - 100\mu m/h$) [82]. However, cracks can occur in thick GaN layers ($> 20\mu m$) on sapphire. The growth rates of the GaN layers depend on the V/III ratios. HVPE can be used to grow high quality GaN layers on *c*-plane sapphire substrates using a two step process similar to that of MOVPE [83]. However, there is not much literature on *a*-plane GaN layers grown on *r*-plane sapphire by HVPE and the growth conditions are still a subject of intense research [69, 84], because a-GaN thick films made by HVPE can be used as substrates to grow homoepitaxial GaN layers.

HVPE growth is a chemical vapor deposition process, where $GaCl$ and NH_3 react to produce GaN. $GaCl$ is synthesized in situ by flowing HCl over liquid metallic Ga according to the following reaction [85]:

$$2HCl_{(g)} + 2Ga \leftrightarrow 2GaCl_{(g)} + H_{2(g)} \tag{3.2}$$

$GaCl$ and NH_3 are mixed above the substrate at $\approx 900°C$. Thermodynamically, the most probable reaction is [85]:

$$GaCl(g) + NH_{3(g)} \leftrightarrow GaN(s) + HCl(g) + H_{2(g)} \tag{3.3}$$

HVPE growth — The standard method to obtain good quality of GaN films is the growth of a nucleation layer at low temperature by MOCVD followed by HVPE [72]. In contrast, in this thesis a-GaN thick films (both the nucleation layer and the GaN film) are grown by HVPE at constant temperature; the pressure is varied during the growth (from 400 mbar to 100 mbar) in order to improve the quality of the GaN layer (as is explained later).

Samples *a*-plane GaN on *r*-plane sapphire were prepared by the Laboratory of Advanced Semiconductors for Photonics and Electronics (LASPE) at the Institute of Quantum Electronics and Photonics (IQEP) at EPFL using the HVPE-ELO process in a commercial Aixtron horizontal HVPE reactor (Figure 3.1), which was equipped with a in-situ reflectance monitoring apparatus [86]. It is a hot-wall reactor with a main reaction tube. The gas inlets are located on the left side of the reactor. There are two upper sources tubes with shower heads above the rotating substrate holder. One is a gallium source and

contains the boat with liquid gallium and HCL diluted in N_2 flowing over the gallium to form $GaCl$ in situ. The other is the ammonia source from which N_2 is obtained. Mixing occurring close to the substrate is crucial to prevent prereactions in the vapor phase and avoid parasitic deposition.

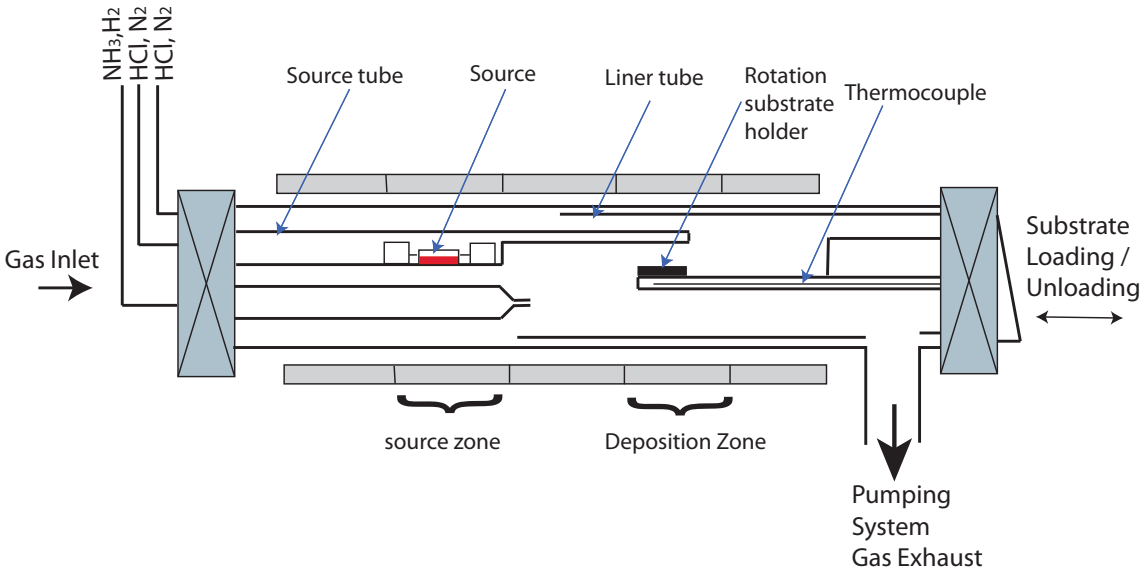

Figure 3.1: *Schematic diagram of the horizontal HVPE reactor [87]*

HVPE-ELO method — A conventional ELO two step growth procedure similar to MOVPE was applied at constant temperature, which consists of (Figure 3.2):

1. Nitridation
2. The growth of the nucleation layer at high pressure.
3. The growth of the buffer layer.
4. The deposition of a SiO_2 mask and etching.
5. GaN growth at low pressure.

The nitridation process consists of the incorporation of N atoms near of the surface of the substrate [88]; with the aim of modifying the surface energy, in order to reduce the dislocation density in the GaN layer. The results of nitridation are sensitive to parameters such as time, temperature, nature of the nitrogen source, gas flow, etc [89, 90]. A

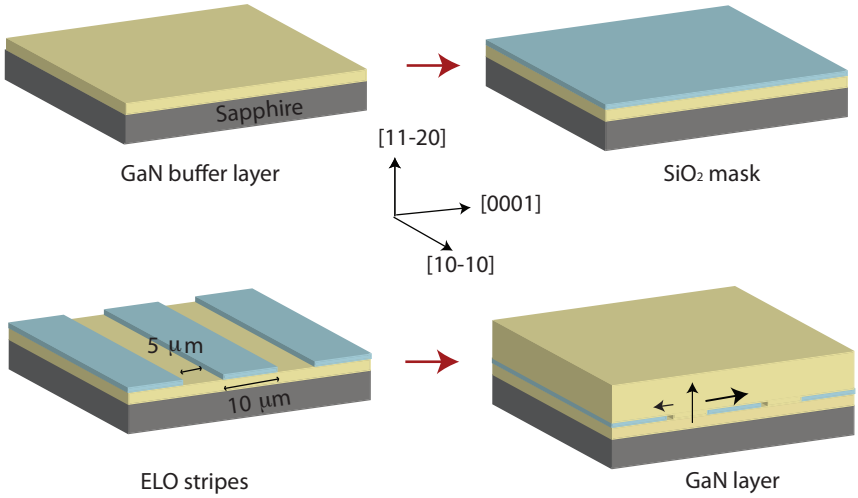

Figure 3.2: *ELO two steps: nitridation, growth of GaN buffer layer, deposition of the mask, etching and the regrowth of the GaN.*

buffer layer is also used to reduce the dislocation density. A ELO SiO_2 mask (200 nm) is deposited onto the buffer layer or the sapphire by plasma enhanced chemical vapor deposition (PECVD). The mask is etched by standard lithography in order to open windows (window 5μm and mask 10μm). The stripes are aligned along [1$\bar{1}$00] direction. A second GaN growth favoring lateral growth is performed in the windows. When the GaN film reaches the SiO_2 mask, it starts growing laterally until the two fronts coalesce forming a flat and full coalesced layer.

SEM Analysis — Several samples are analyzed by SEM in order to find the growth conditions necessary to form a square ELO stripe morphology. Temperature, pressure and H_2 flow are the growth parameters varied during this study. With these conditions, GaN samples are grown until the full coalescence of the film and with a flat surface.

TEM Analysis — In this work, two different types of samples are studied by TEM in this work: without ($S1$) and with GaN buffer layer ($S2$). Samples without buffer layer are grown at constant temperature ($\approx 1090°C$) and growth rate $\approx 20\,\mu m/hr$. The nitridation is performed for 10 minutes at a growth pressure (P_g) $p_g = 970\ mbar$ and a 200 nm thick SiO_2 mask is deposited onto the sapphire substrate (Figure 3.2b). The mask is etched

using standard lithography to form windows, with a window and mask width $5\mu m$ and $10\mu m$, respectively (Figure 3.2c). The stripes are aligned along $[1\bar{1}00]$ direction. The nucleation GaN layer is deposited on sapphire under $p_g = 400$ mbar for two minutes. At this pressure, the GaN grows as large non coalesced islands [91]. This step is followed by a growth of the GaN islands at p_g= 100 mbar for 50 minutes. The growth pressure is reduced in order to allow 2D growth and to obtain a faster lateral growth which improved the surface morphology and optical properties. The surface morphology is smoother when p_g is decreased below 200 mbar [91].

GaN samples with a GaN buffer layer are grown using the same mechanisms as GaN without a buffer layer. After the deposition of the nucleation layer the growth pressure is reduced to 100 mbar and the buffer layer starts to grow. The SiO_2 mask is deposited and patterned along the $[1\bar{1}00]$ direction. It is followed by a regrowth of the GaN in the window areas. The details about the growth conditions for these samples are given in Table 4.1.

Sample	Buffer layer	SiO_2 mask	ELO growth
1	T=1080^oC P_g=400 mbars (1'15") P_g=100 mbars (15')	Thickness=200 nm Openings= 5μm windows=45μm	T= 1087-1075^oC P_g=100 mbars (1h)
2	T=1080^oC P_g=400 mbars (2'23") P_g=100 mbars (30')	Thickness=200 nm Openings= 5μm windows=10μm	T= 1087-1075^oC P_g=100 mbars (1h)
3	T=1080^oC P_g=400 mbars (1'15") P_g=100 mbars (20')	Thickness=200 nm Openings= 5μm windows=10μm	T= 1087-1075^oC P_g=100 mbars (1h)

Table 3.2: *Growth condition for HVPE samples with buffer layer with a growth rate of* $\approx 20\,\mu m/h$.

3.2.3 MBE

MBE is a low temperature growth technique that uses ammonia. The ammonia is a common source for nitrogen which is stable at low temperature. The following reaction takes place in this technique [92]:

$$Ga(g) + NH_3(g) = GaN + \frac{3}{2}H_2 \tag{3.4}$$

where the typical temperature used to grow the GaN films ranges from 960 to 1040^{o}C.

High quality GaN films are obtained using MBE technique for III-nitrides epilayers. However, lower temperatures are required for the growth of a buffer layer. Therefore, low growth rates are obtained due to the low decomposition of the ammonia [1]. MBE is the best technique to produce high quality homoepitaxial layers. MBE process can be described in three steps: nitridation (200°C), low temperature (LT) GaN deposition (650°C) and high temperature (HT) GaN growth ($\sim$ 820°C) [81].

MBE samples — In order to prove the absence of polarization and quantum confined stack effects in a-GaN samples, a single GaN quantum well (SQW) is deposited on the HVPE templates. The growth of a single quantum well is the first necessary step to produce advanced optoelectronic devices (fabrication of microcavities, and finally, the polariton lasers).

HVPE a-GaN samples (described in Table 4.1) are used as templates to grow the MBE layers. They are introduced in a Riber compact 21 MBE chamber [93] to deposit the $Al_{1-x}Ga_xN$/GaN /$Al_{1-x}Ga_xN$ single quantum wells (SQWs). In the Riber chamber, NH_3 is used as a nitrogen source and the growth temperature are between 800 and 820 ^oC. Three sets of two samples are characterized using different Al content ($\approx 5, 10$ and 20%). Table 4.4 shows the growth conditions of the MBE layers grown on the HVPE template. In each set of samples, the $Al_{1-x}Ga_xN$ deposition temperature varies (805, 810 and 820^oC). The two samples in each set vary in the SQW thickness (2 and 5 nm).

Sample	Thickness of the layers nm	Temperature ^oC	Al composition Atomic%
1	GaN=≈800	800	
	$Al-1-xGa_xN$=≈ 200	820	5
	GaN=≈ 2 and 5	800	
	$Al-1-xGa_xN$=≈ 50	820	
2	GaN=≈800	800	
	$Al-1-xGa_xN$=≈ 200	810	10
	GaN=≈ 2 and 5	800	
	$Al-1-xGa_xN$=≈ 50	810	
3	GaN=≈800	800	
	$Al-1-xGa_xN$=≈ 200	805	20
	GaN=≈ 2 and 5	800	
	$Al-1-xGa_xN$=≈ 50	805	

Table 3.3: *Growth condition of the MBE layers (using the growth conditions that in c-GaN).*

3.3 Growth of GaN on sapphire

3.3.1 c-plane GaN

GaN can grow on sapphire in several orientations. The most common is c-plane GaN on c-plane sapphire where the film exhibits a smooth and flat surface [42]. The epitaxial orientation of the c-GaN and c-sapphire layers is shown in Figure 3.3 [31, 94].

The quality of the interface is an important parameter in heteroepitaxial growth. The mismatch between c-GaN and c-sapphire in the epitaxial relationship $(0001)[11\bar{2}0]_{Sapphire} \| (0001)[10\bar{1}0]_{GaN}$ [93, 95] is 16.07% [44, 95]. The misfit depends on the temperature due to the thermal expansion coefficients. Low misfit is a prerequisite for epitaxial growth (about 15%).

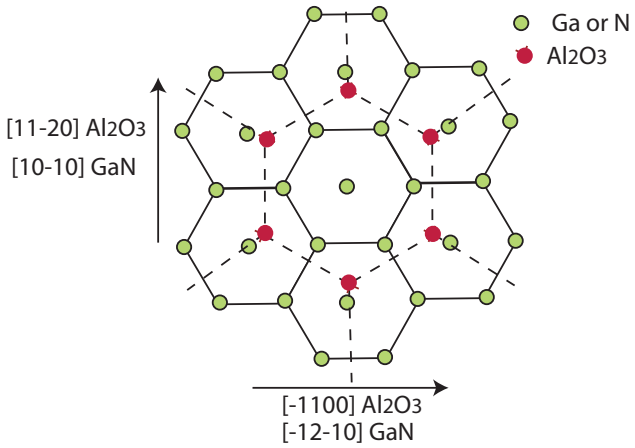

Figure 3.3: *Epitaxial orientation of* $c-(0001)$ *plane GaN on* $c-(0001)$ *plane sapphire.*

The deposition of GaN on c-plane sapphire results in c-plane oriented films rotated by 30^o along the c axis, which makes the directions of $[\bar{1}100]$ GaN and $[\bar{1}2\bar{1}0]$ sapphire parallel . The 30^o rotation from the GaN with respect to the sapphire results in a reduction of the lattice mismatch, which is 16% instead of 32% without this rotation [76].

3.3.2 a-plane GaN on r-plane sapphire

a-GaN is also grown on r-sapphire in order to reduce polarization effects. The epitaxial relationship between the a-plane GaN and r-plane sapphire is shown in Figure 3.4.

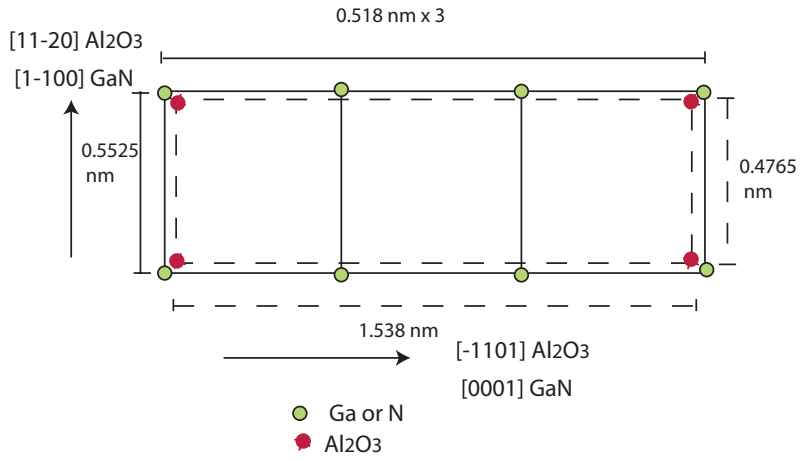

Figure 3.4: *Epitaxial relationship of* $a-(11\bar{2}0)$ *plane GaN on* $r-(1\bar{1}02)$ *plane sapphire.*

The epitaxial relationship of $(11\bar{2}0)$ a-GaN and $(1\bar{1}02)$ r-sapphire is $[0001]_{GaN}\|[\bar{1}101]_{sap}$ and $[1\bar{1}00]_{GaN}\|[11\bar{2}0]_{sap}$ [46, 96]. The lattice mismatch in this relationship is 16% and 1.2% respectively.

3.4 Defects in the crystalline structures

Defects in a crystalline structure can be defined as imperfections or mistakes in the regular arrangement of atoms. They can be classified according to geometric features as point, linear, planar and volume defects. They all have an important effect on material properties.

Dislocations, which are linear defects, can be characterized by their Burgers vector $\vec{b}$ and dislocation line $\vec{u}$. They are edge ($\vec{b} \perp \vec{u}$ or $\vec{b}.\vec{u} = 0$), screw ($\vec{b} \parallel \vec{u}$ or $\vec{b}.\vec{u} = \pm\vec{b}$) and mixed dislocations.

3.4.1 Dislocation in the hexagonal crystal

In hexagonal crystals, the most closely packed plane is the (0001) basal plane and the close packed directions are $< 11\bar{2}0 >$. The most common slip system in the hexagonal crystal occurs on the (0001) basal plane in the $< 11\bar{2}0 >$ direction by the movement of dislocations with Burgers vector $\vec{b} = \frac{1}{3} < 11\bar{2}0 >$. Dislocations can climb to a non basal slip such as prism slip $< 11\bar{2}0 > \{1\bar{1}00\}$ and pyramidal slip $< 11\bar{2}0 > \{10\bar{1}1\}$ which may occur when the basal plane is restricted either by an obstacle or an unfavorable stress field.

The different types of dislocations in the hexagonal structure are described using a representation similar to that given by Thompson for the face centered cubic (f.c.c), but instead of a pyramid, a bipyramid is used in the hexagonal lattice as is shown in Figure 3.5 [97].

The analysis of the bipyramid leads to the following types of dislocations in the hexagonal

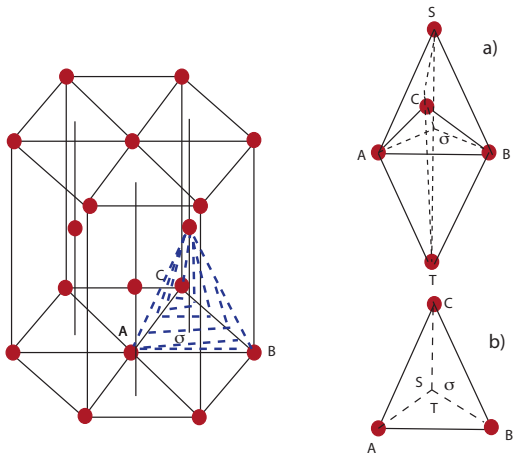

Figure 3.5: *Burgers vector in the hexagonal lattice: a) bipyramid for hexagonal lattice and b) bipyramid projection [97].*

lattice:

- Six perfect dislocations with Burgers vector in the basal plane along the triangular base ABC of the pyramid. They are $\boldsymbol{AB}$, $\boldsymbol{BC}$, $\boldsymbol{CA}$, $\boldsymbol{BA}$, $\boldsymbol{CB}$ and $\boldsymbol{AC}$.
- Perfect dislocations with one of the two Burgers vectors perpendicular to the basal plane, represented by the vectors $\boldsymbol{ST}$ and $\boldsymbol{TS}$.
- Twelve perfect dislocations of the type $\frac{1}{3}[11\bar{2}3]$, whose Burgers vectors are represented by symbols such as $\boldsymbol{SA}/\boldsymbol{TB}$.
- Imperfect dislocations perpendicular to the basal plane, $\sigma\boldsymbol{S}$, $\sigma\boldsymbol{T}$, $\boldsymbol{S}\sigma$ and $\boldsymbol{T}\sigma$.
- Imperfect dislocations of the Shockley partial type $\boldsymbol{A}\sigma$, $\boldsymbol{B}\sigma$, $\boldsymbol{C}\sigma$, $\sigma\boldsymbol{A}$, $\sigma\boldsymbol{B}$ and $\sigma\boldsymbol{C}$.
- Imperfect dislocation which are a combination of the latter two types given by $\boldsymbol{AS}$, $\boldsymbol{BS}$, etc.

The properties of these dislocations in terms of lattice parameters are listed in Table 3.4.

There are three types of perfect dislocations in the hexagonal crystal: a-type, with a Burgers vector $\vec{b} = \frac{1}{3} < 11\bar{2}0 >$, $a+c$ type, with $\vec{b} = \frac{1}{3} < 11\bar{2}3 >$ and c-type, with $\vec{b} =< 0001 >$. They are often referred as edge (a-type), mixed (a+c-type) and screw

Type	AB	ST	SA/TB	Aσ	σS	AS
Direction	$[11\bar{2}0]$	$[000\bar{1}]$	$[11\bar{2}3]$	$[\bar{1}100]$	$[0001]$	$[20\bar{2}3]$
Magnitude	a	c	$\sqrt{c^2+a^2}$	$\frac{a}{\sqrt{3}}$	$\frac{c}{2}$	$\sqrt{(\frac{a^2}{3}+\frac{c^2}{4})}$
Energy $\propto$	a^2	$c^2=\frac{3}{8}a^2$	$\frac{11}{3}a^2$	$\frac{1}{3}a^2$	$\frac{2}{3}a^2$	a^2

Table 3.4: *Dislocations in hexagonal structures [97].*

(c-type) dislocations [98].

Any perfect dislocation can split in two, and the created dislocations are called partial dislocations. They can be Shockley or Frank partial dislocations depending on the SFs type, orientation and interaction [99]. When the Burgers vector is lying on plane of stacking faults the dislocation is Shockley partial. If the Burgers vector is perpendicular to the stacking faults plane the dislocation is Frank partial. For both partial dislocations the Burger vectors are $\vec{b} = \frac{1}{3} < 10\bar{1}0 >$ and $\vec{b} = \frac{1}{6} < 20\bar{2}3 >$respectively. Partial dislocations can have an influence on the optoelectronic properties when the density of SF is large [99, 100].

3.4.2 Stacking faults in hexagonal crystal

A stacking fault (SF) is a displacement of the crystal below the planar defect with respect to the top, thus the regular stacking sequence has been interrupted. In the close-packed hexagonal crystal, the positions of the atoms are shown in Figure 3.6a where A is the reference position and one of the two B or C positions are possible. The normal stacking sequence is $ABABABAB$.. along the c direction (Figure 3.6b) which can be altered with the intersection of an extra layer in C position creating a stacking fault.

Basal stacking faults in the hexagonal structure can be divided into two types: intrinsic (I_1 and I_2) and extrinsic (E). I_1-BSFs can be formed during the growth by removing one plane followed by a shear. It has a stacking sequence $AaBbAaBbCcBbCc$... (Figure 3.7a) with a displacement vector $\vec{R} = \frac{1}{6} < 20\bar{2}3 >$. I_2-BSFs can be formed directly by a shear with a stacking sequence $AaBbAaBbCcAaCc$... (Figure 3.7b) and a displacement vector

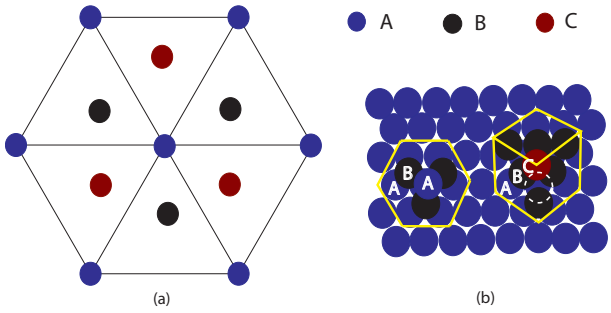

Figure 3.6: *Hexagonal crystal: a) describes atomic positions, A the bottom layers, B the second layer and C is empty and b) describes the normal atomic position and the introduction of extra layer in C-position producing a stacking fault.*

$\vec{R} = \frac{1}{3} < 10\bar{1}0 >$. Finally, E (Figure 3.7c) is formed by inserting an extra plane into the normal stacking sequence and its stacking sequence is $AaBbAaBbCcAaBb...$ with a displacement vector $\vec{R} = \frac{1}{2} < 0001 >$.

Stacking faults also can be found in $\{11\bar{2}0\}$-prismatic plane, which are called *prismatic stacking faults* ($PSFs$) (Figure 3.7d). They have a displacement vector $\vec{R} = \frac{1}{2} < 1\bar{1}01 >$.

A stacking fault is created between two partial dislocations, when a perfect dislocation is dissociated into partial dislocations in order to minimize its line energy. The stacking fault energy provides a force tending to pull the dislocations back together. The stacking faults have a characteristic energy, depending on the changes in the second neighbor sequence of the plane. There is one change for I_1, two for I_2 and three for E.

The width of the stacking fault is given by the spacing between the two partial dislocations and is determined by the stacking fault energy of the crystal [56]. The force γ_1 necessary to satisfy the equilibrium condition for the two partials having a distance d is:

$$\gamma_1 = \frac{\mu}{2\pi d}[(\vec{b}_2.\xi_2)(\vec{b}_3.\vec{u}_3) + \frac{(\vec{b}_2 \times \vec{u}_2).(\vec{b}_3 \times \vec{u}_3)}{1-\nu}] \tag{3.5}$$

where μ shear modulus and ν Poisson's ratio.

The stacking faults in the basal plane have the lowest energy. It has been shown that $\gamma_{I_1} < \gamma_{I_2} < \gamma_E$, where I_1-BSF is the most probable fault to be formed.

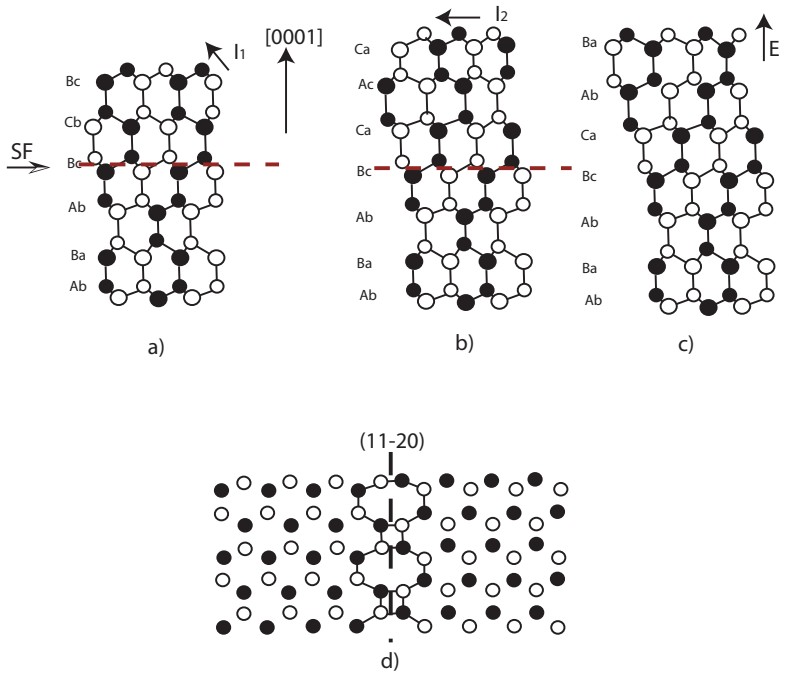

Figure 3.7: *Stacking faults in hexagonal crystal: a) Intrinsic* (I_1) *with* $\vec{R} = \frac{1}{6} < 20\bar{2}3 >$*, b) intrinsic* (I_2) *with* $\vec{R} = \frac{1}{3} < 10\bar{1}0 >$*, c) extrinsic* (E) *with* $\vec{R} = \frac{1}{2} < 0001 >$ *and d) prismatic stacking fault* (PSF) *with* $\vec{R} = \frac{1}{2} < 1\bar{1}01 >$*.*

3.5 Defects in epitaxial GaN layers

In heteroepitaxial layers, defects may be related with small or large misfit strain between the film and substrate. The defects in the heteroepitaxial growth are vacancies and defects produced by the condensation of vacancies during the deposition. Dislocations, twins and stacking faults are formed at the interface when the epilayer grows with the island mechanism (Volmer-Weber mechanism) [101].

Heteroepitaxial layers have a high dislocation density due to the difference of the lattice parameters and thermal coefficients between the film and substrate. The majority of defects in GaN are threading dislocations (TDs), with a dislocation density in the order of 10^{10} cm^{-2} [11]. Stacking faults, inversion domain boundaries and nanopipes [98, 102] are also observed. Optical properties of the heteroepitaxial layers are poor as a result of the high defect density. These defects are non-uniformed and anysotropic [103].

The analysis of defect is important for the study of GaN films because we can understand how defects affect the optical properties. Growth of the films, analysis of defects and the analysis of the optical properties have to be analyzed together in order to improve the quality of the GaN film by varying the growth conditions or taking advantage of new techniques such as ELO. For example, threading dislocations have been found to act as non radiative recombination centers, and stacking faults shift the energy resulting in emission at different energy and limiting the device efficiency.

3.5.1 Defects in ELO grown a-plane GaN

a-GaN layers have a high threading dislocation density of the order of 2 to 4×10^{10} cm^{-2} [14, 51, 104]. In order to reduce the dislocation density, different techniques have been implemented, such as epitaxial lateral overgrowth (ELO) [47, 105, 106] , pendeo-epitaxy (PE) [51], the surface preparation (nitridation) [107] and the low temperature buffer layer (AlN or GaN) [36]. ELO is the most common and successfully reduces the dislocation density by 2 orders of magnitude ($1 \times 10^8 cm^{-2}$ [11, 14, 51]). The threading dislocations under the SiO_2 mask are block as is shown in Figure 3.8. Only in the window areas, the dislocations propagate torwards the surface. During the lateral growth, new defects are formed in the overgrown areas.

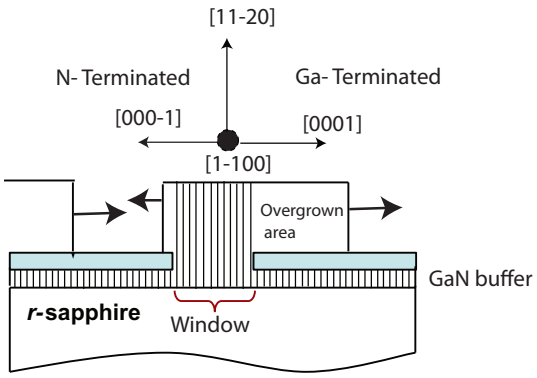

Figure 3.8: *Schematic picture of the ELO pattern. The blue region represents SiO_2 masks and overgrown area is above the SiO_2 masks.*

Some causes for the formation of defects in the overgrown areas are:

- The cooling of the growth process due to the thermal expansion coefficients differences between the SiO_2 and the GaN.
- Imperfections in the SiO_2 mask contribute to the formation of stacking faults.
- Impurities above the SiO_2 mask can create stacking faults and voids.
- Residual strain coming from the window areas.
- The coalescence of the two meeting fronts, the [0001] and [000$\bar{1}$] directions.
- Strain accumulated during the lateral growth.

The reduction of the defect density in the ELO areas improves the surface morphology and luminescence [14]. In *a*-GaN layers, TDs have their dislocation line parallel to the growth direction ([11$\bar{2}$0]) with a Burgers vector $\vec{b} = \frac{1}{3} < 11\bar{2}0 >$ [47].

In a-plane ELO structure (Figure 3.8), the vertical sidewalls of the stripes are $\{0001\}$*c*-plane facets with opposite polarities while the top horizontal facet is the non polar (11$\bar{2}$0) growth surface [96]. The difference of growth rates of polar surfaces introduces an asymmetry of the lateral overgrowth. The (0001) surface, identified as Ga face, grow faster than the (000$\bar{1}$) as N face [104]. Polarity has strong influence on the defect reduction in the lateral region, since Ga terminated regions have less defects than N terminated regions [96].

The orientation of the SiO_2 stripes is an important factor during the overgrowth. It has an influence on the nature of the defects and the morphology of the GaN layer. In the [1$\bar{1}$00] direction, the TDs originating at the GaN/sapphire interface go straight to the surface and do not propagate to the ELO area (Figure 3.9a). On the other hand, when the stripes are aligned in [0001] direction (Figure 3.9b), the TDs in the window area bend and propagate to the overgrown area increasing the dislocation density [47, 108]. Threading dislocations do not bend 90^o or more like in c-plane GaN [109,110]. They bend approximately 30^o, therefore, the threading dislocations go through the layer towards the surface, that results in a small reduction of the dislocation density in the window areas and a small increment in the overgrown areas.

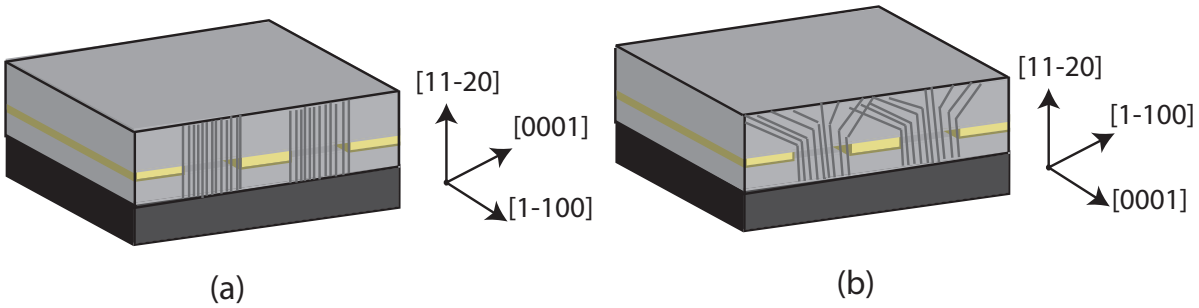

Figure 3.9: *Behavior of defects with the stripes alignment: a) along* $[1\bar{1}00]$ *direction; dislocations cross the layer towards the surface, and b) along* [0001] *direction; dislocations bend* 30^o *to the overgrown areas.*

a-plane GaN has a tendency to contain higher SF density than c-plane GaN, impairing the optical properties [11]. The stacking faults in *a*-plane GaN have their origin at the sapphire/buffer layer interface and propagate to the GaN surface, while in c-plane they are parallel to the c-direction [111], and remain in the vicinity of GaN/SiO_2 interface. The SF density is reduced from $10^6\,cm^{-1}$ in the window areas to $10^4\,cm^{-1}$ in the overgrowth areas [112]. Basal and prismatic stacking faults are found in *a*-GaN with displacement vectors $\vec{R} = \frac{1}{6}[\bar{2}0\bar{2}3]$ and $\vec{R} = \frac{1}{2}[10\bar{1}\bar{1}]$ respectively [33,113]. Zakharov et-al and Hankell et al. [33,69] found I_1-BSFs bounded by two glissile Shockley partial dislocations of Burgers vector $\vec{b} = \frac{1}{3} < 1\bar{1}00 >$. They are thought to result of strain relaxation in the layer.

Photoluminescence studies of a-plane GaN films show an improvement of the optical properties in the overgrown areas [114]. Chitnis et al. [2] and Chen et al. [3] reported the feasibility of the fabrication of non-polar visible light emitting devices free of polarization effects. Non-polar heterostructures thin films (a-GaN/AlGaN) [115], show an improvement of the optical and structural properties. These films are candidates for the development of high efficiency ultraviolet light emitters [116,117].

Chapter 4

Analysis of results and discussion

Defect in a-$(11\bar{2}0)$ plane GaN on r-$(1\bar{1}02)$ plane sapphire substrates grown by hydride vapor phase epitaxy (HVPE) and epitaxial lateral overgrowth (ELO) techniques are studied by electron microscopy. TEM analysis reveals that the majority of defects in the GaN layers are threading dislocations and basal stacking faults. Furthermore, other varieties of stacking faults are also observed in the a-GaN samples. The Burgers vector $\vec{b}$ and the displacement vector $\vec{R}$ are determined using the invisibility criterion ($\vec{g}.\vec{b} = 0$ and $2\pi\vec{g}.\vec{R} = 0$ or $2\pi n$). We find that some dislocations have been dissociated into two Shockley partial dislocations with a short I_2 intrinsic fault between them. Liquid helium temperature cathodoluminescence and μ-photoluminescence techniques have been used to analyze the influence of structural defects on the optical properties of a-GaN films.

4.1 Defects structure of a-plane GaN films

Defects play an important role in device applications due to their influence on the optical and electrical properties of semiconductors. *a*-plane GaN specimens were grown by HVPE-ELO on r-plane sapphire by LASPE-IQEP. ELO was used in order to reduce the dislocation density and to improve the quality of the film. It is observed that a-plane GaN films have a higher defect densities than c-plane GaN layers, despite the fact that *c*-plane GaN has a higher lattice mismatch (c-GaN 16% and a-GaN 1.2%). Threading disloca-

tions (TDs) and stacking faults (SFs) are the main defects found in the a-GaN layers. Furthermore, it is found by scanning electron microscopy (SEM) that the morphology of the GaN stripes depends on the growth conditions. No dislocation bending, such as that occurring in *c*-plane GaN [110], is observed.

4.2 Influence of the growth parameters on the GaN stripes' morphology.

The growth conditions of a-GaN grown by HVPE-ELO have a strong influence on GaN stripe morphology since they control the development of facets. Figure 4.1 shows schematically the different morphologies of the GaN stripes obtained in this study. It shows the different surface facets oft the stripes. The facets' orientations are influenced by the temperature and the gas flow. The optimization of the growth parameters of *a*-plane GaN samples was made in order to obtain a GaN stripe morphology with a flat surface (Figure 4.1) and a fully coalesced layer.

The growth conditions for a-GaN HVPE-ELO samples are shown in Table 4.1. The GaN morphology is sensitive to temperature (°C), H_2 flow rate (sccm[1]) and V/III=ratio. Both factors affect the vertical and horizontal growth rates, and therefore yielding different stripes' geometries (Figure 4.2).

Morphology	Temperature (°C)	H_2 (sccm)	Pressure (mbar)	V/III ratio
Triangular	1090	1500	100	100
Trapezoidal	1060	3000	100	200
Rectangular	1090	3000	100	200

Table 4.1: *Morphology of a-GaN stripes as a function of growth conditions.*

Cross-sectional micrographs of the morphologies of the a-GaN stripes are shown in Figure

[1]Common unit in gas flow. sccm standard cubic centimeters per minute ($T = 0^o$ and 1 atm).

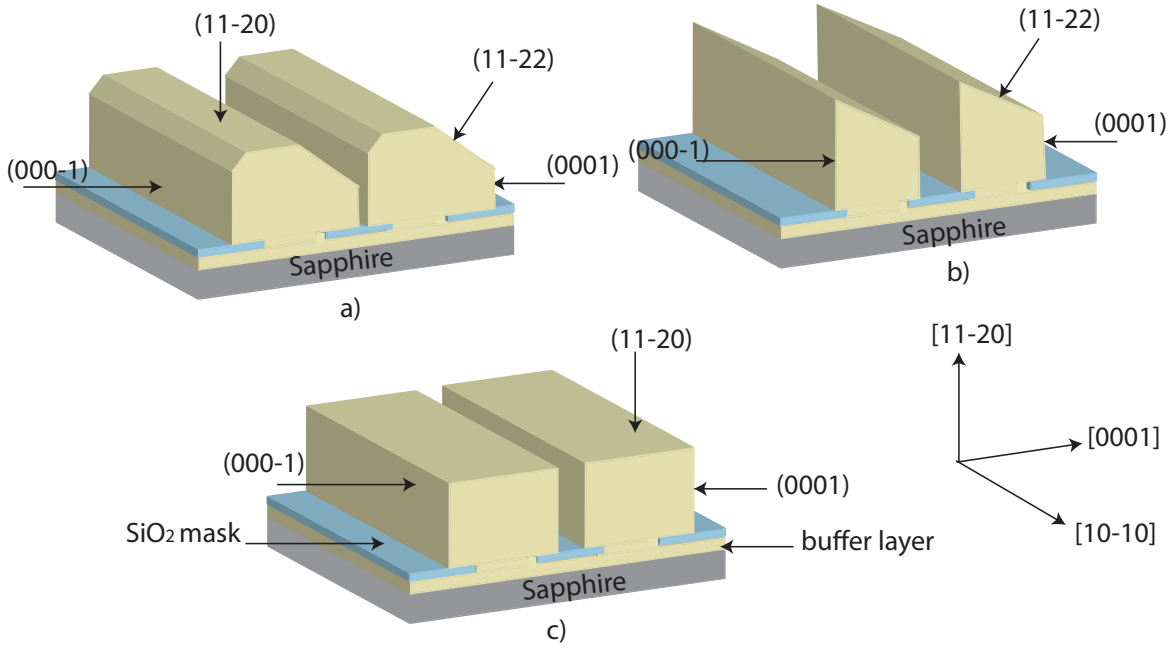

Figure 4.1: *Scheme of a-GaN stripes morphology depending on the growth parameters of temperature, gas flow and pressure: a) trapezoidal, b) triangular and c) rectangular. The* $(11\bar{2}0)$ *facet is sensitive to the growth parameters such as temperature and gas flow. The stripes always are limited by* (0001), $(000\bar{1})$ *facets and, for the triangular and trapezoidal morphologies, with inclined* $(11\bar{2}2)$ *facets.*

4.2 for the different growth parameters of Table 4.1. In each SEM micrograph, the a-GaN stripes are always limited by (0001) and $(000\bar{1})$ vertical facets, conventionally called Ga- and N- faces, respectively. The lateral growth rate of the Ga-face is approximately 5 times larger than that of the N-face due to their different polarity. Figure 4.2(a) shows an a-GaN layer of triangular morphology. The angle between the $\{11\bar{2}0\}$ top facet and the inclined facet is $\approx 31^o$. At this angle, the corresponding facet is the $\{11\bar{2}2\}$. An example of trapezoidal morphology with inclined $\{11\bar{2}2\}$ facets (the angle remains $\approx 31^o$) and horizontal $\{11\bar{2}0\}$ facets is shown in Figure 4.2(b). Figure 4.2(c) shows a rectangular morphology with horizontal $\{11\bar{2}0\}$ facets, this is the optimal morphology to growth a-GaN.

a-GaN films have a narrow growth window (range of parameters) and, therefore , any small variation in the growth conditions affects the ELO stripe morphology. For the rectangular

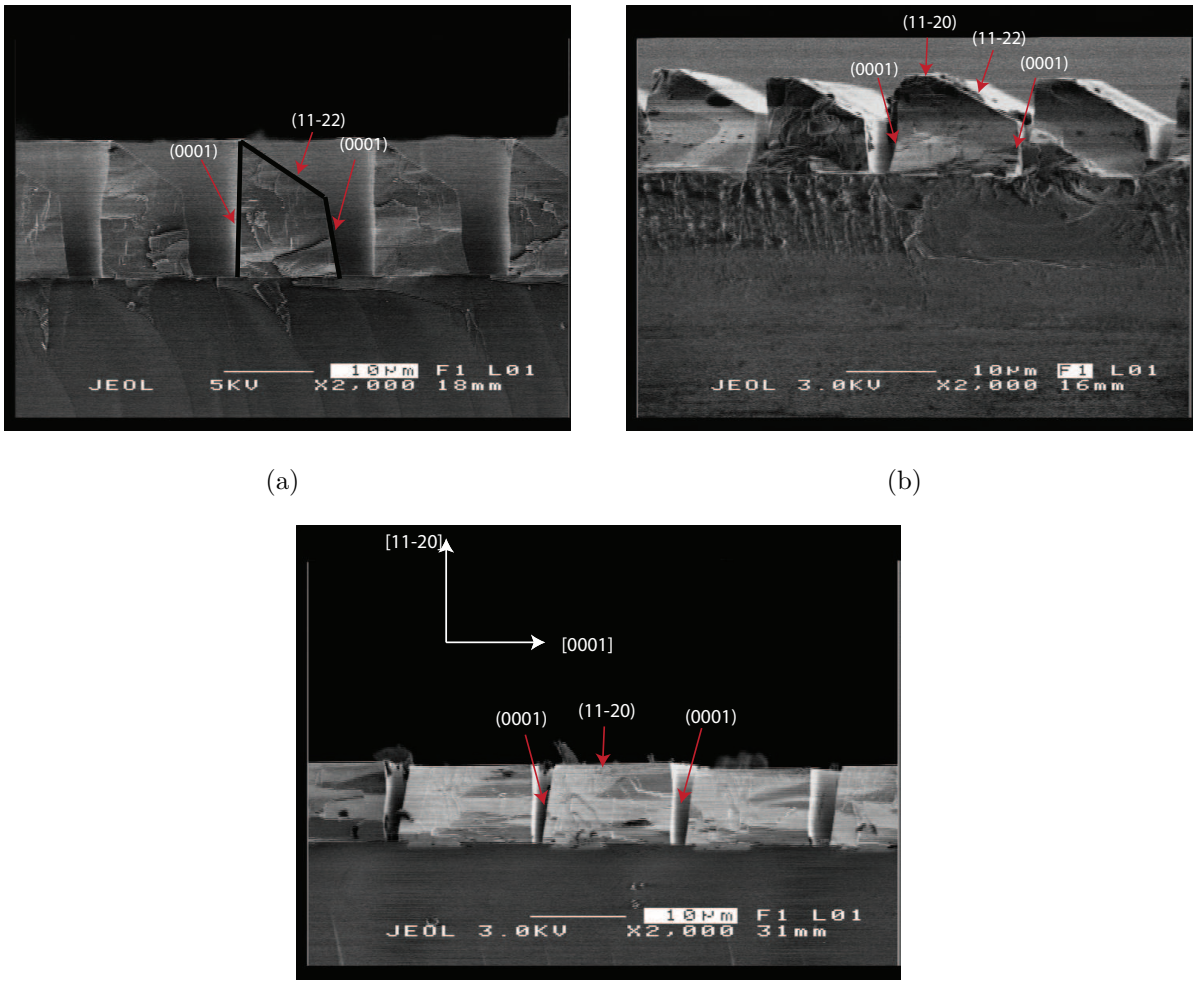

(a) (b)

(c)

Figure 4.2: *SEM images of the cross sectional morphology of a-GaN films grown by ELO-HVPE. The morphology depends on the growth parameters (Table 4.1). a) triangular, b) trapezoidal and c) rectangular. These morphologies are limited horizontally by* (0001) *and* $(000\bar{1})$ *vertical facets. The triangular and trapezoidal stripes present* $(11\bar{2}2)$ *diagonal facets. The trapezoidal and rectangular stripes are also limited by* $(11\bar{2}0)$ *horizontal facet (top). The rectangular morphology is the optimal morphology to obtain a full and coalesced layer.*

and trapezoidal morphologies, the pressure and the V/III ratio are constant, at 100 mbar and 200 respectively. When the growth temperature is decreased from 1090 to 1060^{o}C, the ELO morphology changes from rectangular to trapezoidal due to the preferential growth of the $\{11\bar{2}2\}$ plane. This means that, at the lower temperature, the vertical growth is dominant, and the ratio of lateral to vertical growth rate is less than 1. When the temperature increases, the ratio becomes larger, due to the improvement of the lateral growth from the (0001) facet. The growth at lower temperatures delays the coalescence of the lateral growth fronts. For this reason, a thicker film must be grown in order to obtain full and flat coalesced films.

When the temperature and pressure remain constant and the V/III ratio changes from 200 to 100, a triangular ELO morphology is obtained. The vertical growth rate is faster than the lateral growth rate, resulting in the formation of inclined $\{11\bar{2}2\}$ facets. The vertical growth rate in the triangular morphology is much larger than in the trapezoidal morphology (Figures 4.2(a), and 4.2(b)); under such conditions the growth of the $\{11\bar{2}0\}$ facet stops. The lateral to vertical growth rate in the triangular morphology is smaller than in the trapezoidal morphology. Another parameter that affects the $\{11\bar{2}0\}$ facet is the growth pressure. At high pressure (>200 mbar), the $\{11\bar{2}0\}$ facets are rough; they become smoother with the reduction of the pressure [91].

4.2.1 Discussion

The first part of this thesis is the analysis of the ELO stripe morphology. It has been demonstrated that small variations of the growth conditions change the growth rates and morphology of the ELO stripes. In order to obtain a flat and full coalesced GaN layer, the growth conditions were analyzed.

The following growth facets were obtained with various temperatures and V/III ratio: $\{0001\}$, $\{11\bar{2}0\}$ and $\{11\bar{2}2\}$. The $\{11\bar{2}2\}$ facet appears when the vertical growth is faster than the lateral one. The corresponding atomic configuration with dangling bonds and surface polarity is shown in Figure 4.35. When the growth parameters are changed fa-

vorably to obtain a trapezoidal or a triangular morphology, the $\{11\bar{2}2\}$ facet grows with N-polarity and a high number of dangling bonds. This facet has the possibility of N- or Ga- polarities on the surface. The surface with N-polarity tends to appear because surface nitrogen atoms are stabilized under the growth condition of high V/III ratio at high pressure or low temperature [118]. Therefore, at high temperature, the growth rate of $\{11\bar{2}2\}$ facets becomes slower, improving the $\{11\bar{2}0\}$ top facet. On the contrary, with a low V/III ratio, the $\{11\bar{2}2\}$ facet becomes larger.

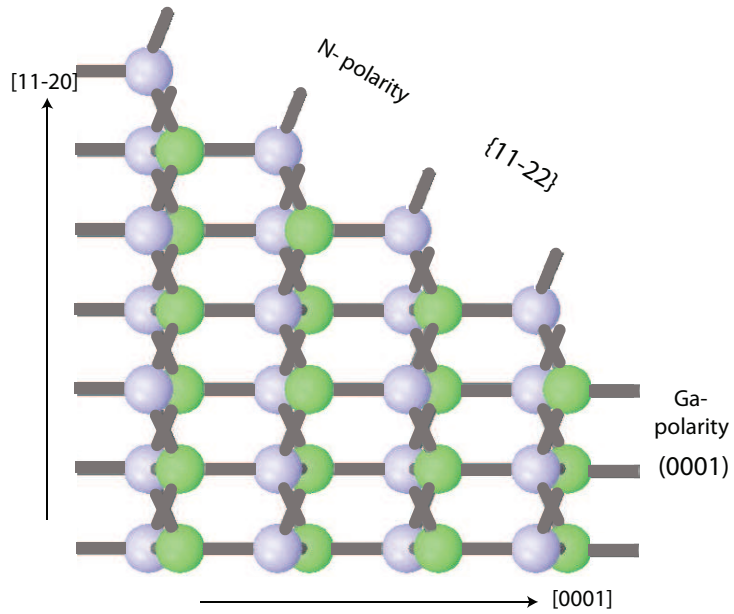

Figure 4.3: *Schematic representation of the configuration of GaN planes.*

We conclude that, in order to obtain a fully coalesced layer with a flat surface, a high temperature, a high H_2 flow rate and a low pressure are required (rectangular morphology Figure 4.2(c)). In the rectangular morphology, the required growth time is smaller than that of the other morphologies. In a-GaN layers, the free surface of the layers is rough due to its high content of defects which propagate through the layer. *a*-GaN layers with threading dislocations have the tendency to form pits on the top GaN $\{11\bar{2}0\}$ surface. A higher TD density means a higher pit density, and consequently a rougher surface.

4.3 The epitaxial relationship between the a-plane GaN and r-plane sapphire

The epitaxial relationship between the a-plane GaN and r-plane sapphire was obtained by TEM. Figure 4.4(a) shows a selected area (SAED) diffraction pattern from the a-GaN/r-sapphire interface, where the $[10\bar{1}0]$ direction in a-GaN (red circles) corresponds to the $[11\bar{2}0]$ direction in r-sapphire (grey circles). From the two spots indicated by the arrow *1* of Figure 4.4(a), we measured a $6^o \pm 0.5$ inclination of the $(1\bar{1}04)_{sapphire}$ plane with respect to the $(0002)_{GaN}$ plane. When the $\{11\bar{2}0\}_{GaN}$ plane is parallel to $\{1\bar{1}02\}_{sapphire}$ plane, a small misorientation between the $\{0002\}_{GaN}$ and $\{1\bar{1}04\}_{sapphire}$ planes occurs. The diffraction pattern in Figure 4.4(b) was obtained by JEMS [119] for the same relationship of GaN/sapphire. The red spots are the diffraction pattern of the GaN and the gray spots are the diffraction pattern of the sapphire. The planes from the point 2 (Figure 4.4(b) are parallel ($\{1\bar{2}10\}_{GaN}$ and $\{1\bar{1}02\}_{sapphire}$) and they are closely aligned to each other in order to obtain the $[11\bar{2}0]$ growth direction. For this reason the planes in the point 1 ($\{0002\}_{GaN}$ and $\{1\bar{1}04\}_{sapphire}$) have a small inclination with respect to each other.

The epitaxial relationship in this orientation, deduced from the SAED from Figure 4.4(a), is:

$$(0002)[10\bar{1}0]_{GaN} \parallel (1\bar{1}04)[11\bar{2}0]_{sapphire} \tag{4.1}$$

With this orientation relationship, the lattice mismatch between the a-GaN and r-sapphire was calculated using the interplanar spacings $d_{0002} = 0.25925\,nm$ and $d_{1\bar{1}04} = 0.25510\,nm$, GaN and sapphire respectively. Taking the 6° inclination into account, the $d_{1\bar{1}04}$ interplanar distance changes to $d_{1\bar{1}04}/cos6^\circ = 0.2565\,nm$. The calculated lattice mismatch, $\frac{d_{GaN}-d_{sapphire}}{d_{sapphire}}$, is $\approx 1.1\%$.

To allow full relaxation, this lattice mismatch is accommodated by the formation of misfit dislocations (MDs). In this case, there should be an extra half plane either in the substrate or in the epilayer every n planes. In our case, a full relaxation would be obtained when the number of planes between misfit dislocations in GaN, $n = \frac{d_{sapphire}}{d_{GaN}-d_{sapphire}}$ [44], is ≈ 93

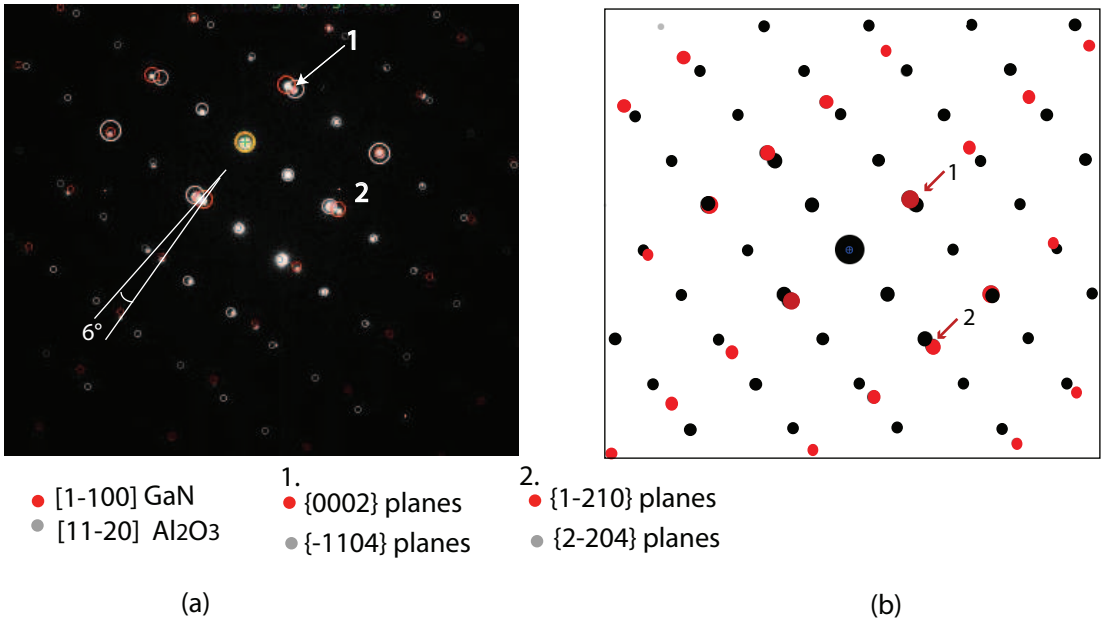

Figure 4.4: *Epitaxial relationship between a-GaN and r-sapphire: (a) experimental diffraction pattern observed by SAED; red circles shows the* $[10\bar{1}0]$ *zone axis of GaN and gray circles the* $[11\bar{2}0]$ *zone axis of sapphire. The sapphire planes are rotated* 6^o *from the growth* $[11\bar{2}0]$*-direction. (b) diffraction pattern of a-GaN and r-sapphire obtained by JEMS, where the sapphire planes (black spots) are tilted to respect the growth direction. Red arrows are pointed the GaN plane (red spots).*

or the distance between them is 23.5 nm ($d_{MDs} = \frac{d_{GaN}}{f}$ [120]).

A HRTEM micrograph of a-GaN/r-sapphire interface taken along the $[10\bar{1}0]$ GaN and the $[11\bar{2}0]$ sapphire zone axes is shown in Figure 4.5(a). A step at the interface is observed in this figure where the atomic interfacial structure cannot be clearly determined by HRTEM experiments. These stepped interfaces may be a result of the nitridation on the sapphire [44].

The sapphire substrates used for the HVPE experiments initially have with a flat and smooth surface, with roughness of approximately one atomic layer. The steps observed in the GaN/sapphire interface (Figure 4.5(a)) are created during the nitridation (10 minutes). These steps consist of several atomic layers which are difficult to distinguish because the HRTEM micrograph shows a projection of the interface.

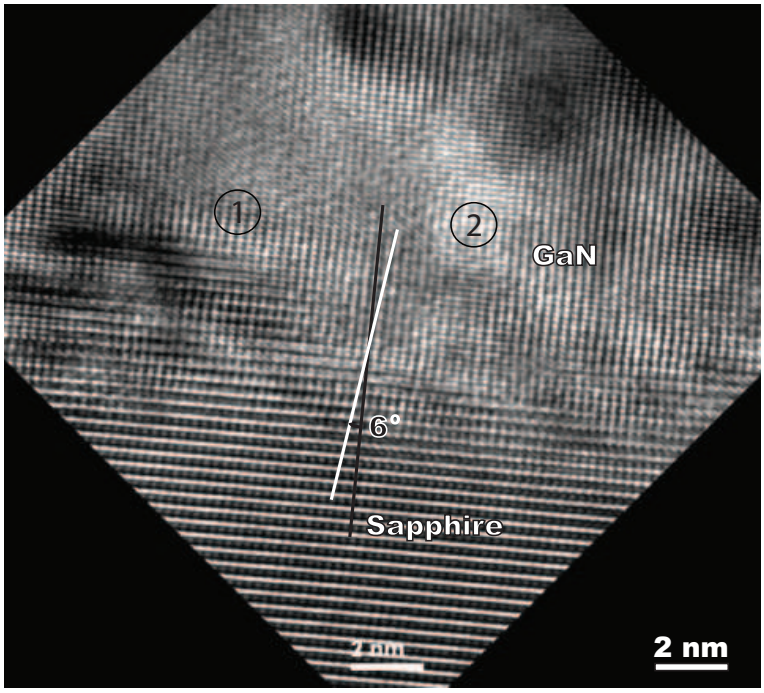

(a)

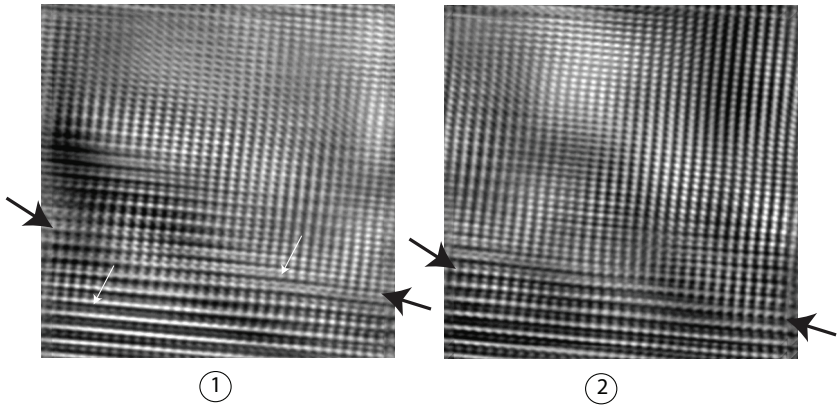

(b)

Figure 4.5: *HRTEM Micrographs: a) a-GaN/r-sapphire interface along the* $[10\bar{1}0]$ *zone axis GaN and* $[11\bar{2}0]$ *zone axis sapphire: black and white lines show the inclination* (6^o) *between sapphire planes with respect GaN planes. b) Magnified images of the interface from both sides of the lines in Figure 4.5(a) are marked by* 1 *and* 2*. Black arrows point the position of the interface and white arrows point the misfit dislocations at the interface (it is difficult to define the GaN/sapphire interface due to the roughness of the sapphire).*

The inclination of the sapphire planes with respect to the a-GaN planes can be clearly observed in Figure 4.5(a) where the black line indicates the (0002) planes in GaN and the white one the $(1\bar{1}04)$ sapphire plane. Figure 4.5(b) shows magnified images from both sides of the lines marked by *1* and *2* (Figure 4.5(a)). The black arrows in both images show the position of the GaN/sapphire interface, while white arrows show the position of extra planes in GaN layer. The extra planes are located in the magnified image labelled by *1* in Figure 4.5(b). Experimentally, we observe that in GaN films, the number of misfit dislocations in Figure 4.5(b) is different than the one theoretically calculated above. The spacing between the extra planes is ≈ 5 times smaller than that predicted. It is also observed that the measured misfit dislocation number is not consistent from area-to-area.

4.3.1 Discussion

It has been shown that for epitaxial a-GaN layers, the $\{11\bar{2}0\}_{GaN}$ planes are parallel to $\{1\bar{1}02\}_{sapphire}$ planes (Figure 4.4). As a consequence, the $\{1\bar{1}04\}_{GaN}$ planes have an inclination of $\approx 6^o$ with respect to $\{11\bar{2}0\}_{GaN}$ planes (growth direction).

The epitaxial interface between a-GaN and r- sapphire has steps (Figure 4.5), because of the rough r-sapphire surface that results from the nitridation process [44]. According to Hashimoto et al. [121] and Uchida et al. [90], the sapphire surface is affected by the nitridation conditions such as time, temperature, gas flow, etc. A short nitridation time (< 3 min) results in sapphire with smooth surface, while a longer nitridation time (i.e. 10 min), introduces stress which induces protrusions. Dwikusuma et al. [122] studied the nitridation as a function of time and NH_3 partial pressure (p_{NH_3}), but they did not find protrusions in the sapphire after long nitridation time.

The epitaxial relationship obtained by SAED in this system is $(0002)[10\bar{1}0]_{GaN} \parallel (1\bar{1}04)$ $[11\bar{2}0]_{sapphire}$, resulting in a lattice mismatch of $\approx 1.1\%$. Despite the smaller lattice mismatch in a-GaN layers compared to that measured in c-GaN layers, a high defect density has been observed. This could be due to the imperfections introduced during the nitrida-

tion and cooling steps in the growth.

The poor interface quality, a consequence of the imperfections and impurities on the sapphire, may be responsible for the high defect density, mainly SFs. A high SF density is observed at the a-GaN/r-sapphire interface in Figure 4.6. This high density originates from the imperfections on the sapphire surface; the GaN planes have to fit between these imperfections, thus creating the SFs. Figure 4.6 shows that stacking faults are formed at the a-GaN/r-sapphire, even if we cannot see the substrate since the sample was inclined by 30^o for the observation. In the interface of Figure 4.6, we can observe protrusions with approximately 4 nm width. Protrusions have a clear correlation with the SFs.

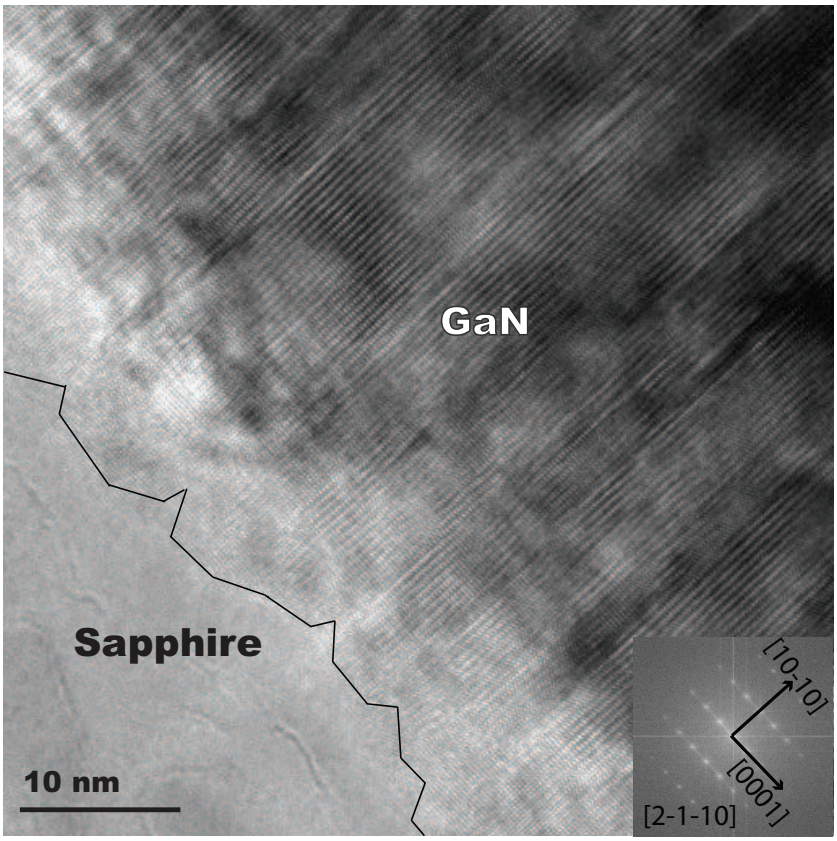

Figure 4.6: *HRTEM micrographs taken along* $[2\bar{1}\bar{1}0]$ *zone axis GaN of basal stacking faults originated at the a-GaN/r-sapphire interface. The a-GaN sample is inclined* 30^o.

4.4 Dislocations in a-plane GaN layers

The optical properties in GaN layers are improved by the reduction of dislocation density because dislocations are non-radiative recombination centers. In order to reduce the dislocation density of a-GaN layers, techniques like ELO have to be implemented in the growth process.

The analysis of dislocations has been performed in three areas defined by the ELO morphology (Figure 4.7) of a fully coalesced layer:

1. Window areas (or openings) where the GaN film grows from sapphire.

2. Overgrown areas (above the SiO_2 mask) where the growth is vertical and lateral.

3. Coalesced areas which are the areas where two fronts meet.

Two types of samples,those without (identified as $S1$) and with (as $S1$) buffer layer were studied.

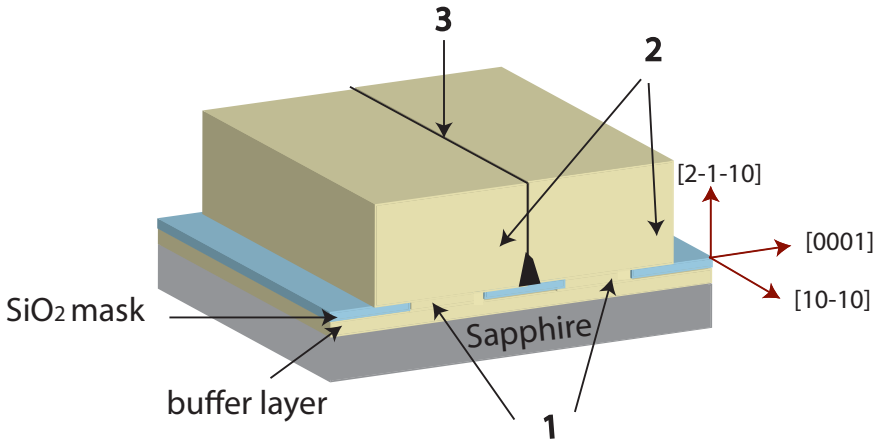

Figure 4.7: *ELO morphology scheme of a fully coalesced GaN layer (see details in the text).*

4.4.1 Dislocations in window areas

Threading dislocations (TDs) are the most common defects observed in the GaN films. They have their dislocation lines parallel to the $[2\bar{1}\bar{1}0]$ growth direction. The threading dislocations are due to both lattice mismatch and island coalescence in the nucleation layer.

High threading dislocation density is found in the window areas in both $S1$ and $S2$ samples. A micrograph taken close to $[10\bar{1}0]$ zone axis shows threading dislocations crossing the thickness of the film from the GaN/sapphire interface to the surface (Figure 4.8). The SiO_2 mask stops the threading dislocations as well as the SFs from the buffer layer and, therefore, the overgrown areas are almost free of defects.

The dislocation density of $S1$ and $S2$ samples was measured and compared. They are equal and are of the order of $\approx 1 \times 10^{10}\ cm^{-2}$. These dislocation densities are in the same order that those obtained by MOCVD [104] and HVPE [14]. The TDs that their Burgers vector is perpendicular to the c direction and parallel to the $< 2\bar{1}\bar{1}0 >$ direction are in contrast under $\vec{g} = (1\bar{2}10)$ and are out of contrast under $\vec{g} = (0002)$ diffraction conditions. Their Burgers vector $\vec{b}$ is $\frac{1}{3}[\bar{2}110]$ and their dislocation line ($\vec{u}$) is parallel to the $[2\bar{1}\bar{1}0]$ direction. They have a screw character. The threading dislocations that are visible under $\vec{g} = (0002)$ and $\vec{g} = (1\bar{2}10)$ diffraction conditions have $\vec{b} = \frac{1}{3} < 11\bar{2}3 >$.

The density of TDs with Burgers vector $\vec{b} = \frac{1}{3}[11\bar{2}3]$ in the window areas is small compared to their overall density, and is of the order of $1 \times 10^{9}\ cm^{-2}$. A plan-view DF micrograph under $\vec{g} = (0002)$ diffraction condition, taken between the window and ELO areas, is shown in Figure 4.9. Under this condition, the dislocations with Burgers vector $\vec{b} = \frac{1}{3}[11\bar{2}0]$ are not visible, and only the dislocations with Burgers vector $\vec{b} = \frac{1}{3}[11\bar{2}3]$ are visible. The dislocation with Burgers vector $\vec{b} = \frac{1}{3}[11\bar{2}0]$ leave traces when they intercept the surface; these traces are indicated by red arrows in Figure 4.9.

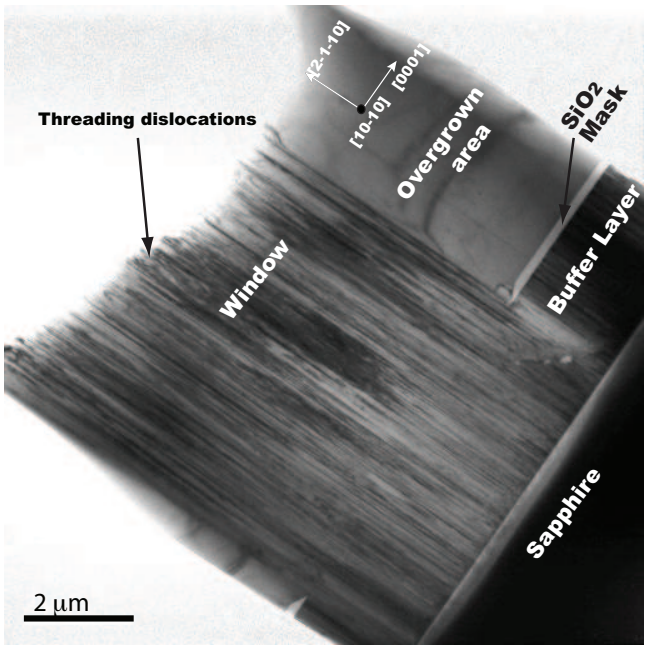

Figure 4.8: *Micrograph under* $[10\bar{1}0]$ *zone axis: high threading dislocation density is observed in the window areas.*

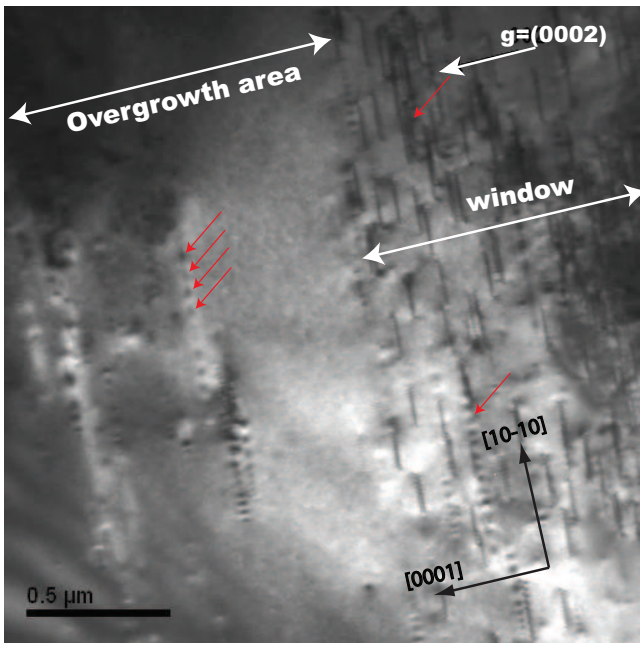

Figure 4.9: *Plan-view DF micrograph under* $\vec{g} = (0002)$ *diffraction condition of the window and overgrown areas: high density of* $\vec{b} = \frac{1}{3}[11\bar{2}3]$ *dislocations is observed in the window areas. Traces of the interception of the dislocations with the surface are indicated by red arrows.*

4.4.2 Dislocations above the SiO_2 mask (overgrown area)

When the GaN film reaches the level of the SiO_2 mask, it starts growing laterally in both [0001] and [000$\overline{1}$] directions. It is thus expected that the overgrown areas must be free of dislocations, because the threading dislocations in the window areas propagate straight towards the film surface. However, dislocations are observed in these areas.

TEM observations show that the overgrown areas in both samples ($S1$ and $S2$) contain a dislocation density in the range 3×10^8 to $1 \times 10^9\, cm^{-2}$, depending on the area of analysis. A higher dislocation density is found closer to the SiO_2 mask that closer to the top surface of the layer (Figure Figure 4.10). For $S1$ samples, the high dislocation density close to the SiO_2 mask reduces after $\approx 1.5\,\mu m$ distance from the mask. At the top surface, the dislocation density reduces to $3 \times 10^8\, cm^{-2}$.

The distribution of the dislocations in both window and overgrown areas is shown in the BF micrographs under $\vec{g} = (1\overline{2}10)$ and $\vec{g} = (0002)$ diffraction conditions in Figure 4.10.

The defects in the left part of Figure 4.10(a) are threading dislocations coming from the window areas and propagating towards the top film surface. Dislocations in the overgrown areas, which are visible under $\vec{g} = (1\overline{2}10)$ diffraction condition (Figure 4.10(a)) and invisible under $\vec{g} = (0002)$ diffraction condition (Figure 4.10(b)), have a Burgers vector $\vec{b} = \frac{1}{3} < 11\overline{2}0 >$.

We can conclude that:

1. Threading dislocations with dislocation line ($\vec{u}$) parallel to the growth direction ([$2\overline{1}\overline{1}0$]) in the openings and overgrown areas have screw characters with Burgers vector $\vec{b} = \frac{1}{3}[11\overline{2}0]$.

2. There are dislocations lying parallel to the SiO_2 mask (i.e. along [0001] direction). These are located within $\approx 1.5\,\mu m$ of the SiO_2 mask in Figure 4.10(a), and are out of contrast when $\vec{g} = (0002)$ and have a Burgers vector $\vec{b} = \frac{1}{3} < 2\overline{1}\overline{1}0 >$. Since their dislocation line direction is parallel to the [0001] direction, they have an edge character.

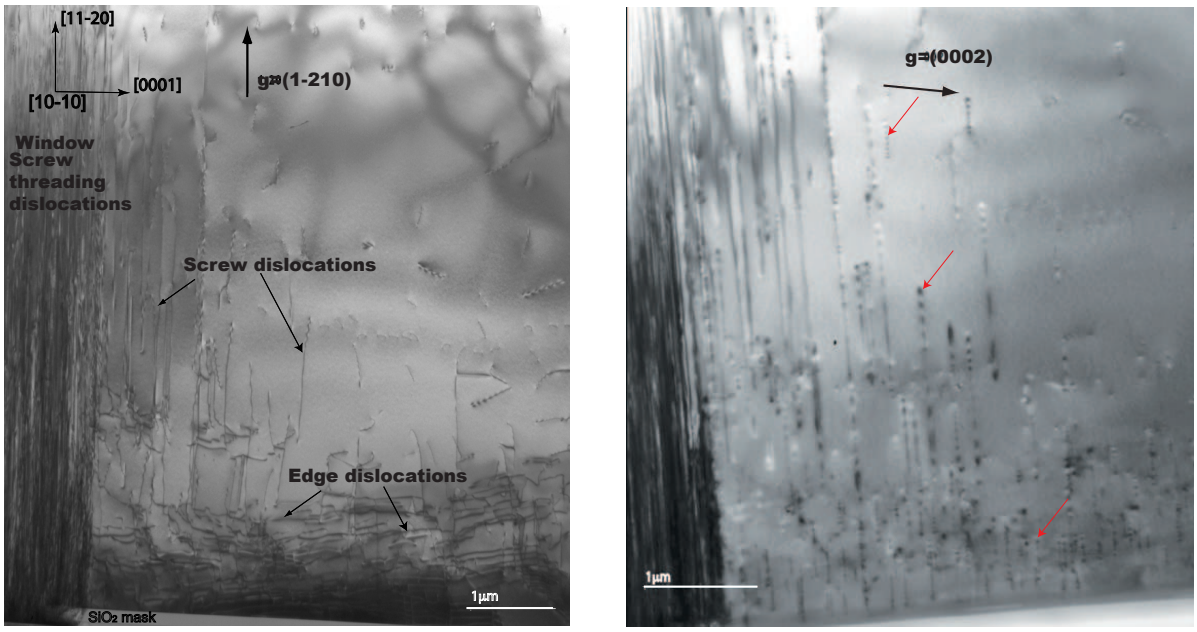

(a) (b)

Figure 4.10: *BF TEM micrographs of the distribution of dislocations in the window and overgrown areas. a) Image under* $\vec{g} = (1\bar{2}10)$ *diffraction condition shows a high dislocation density in both areas close to the* SiO_2 *mask. b) Under* $\vec{g} = (0002)$ *diffraction condition, the dislocations are not visible in the overgrown area, leaving some residual contrast (red arrows). According to the invisibility criterion their Burgers vector is* $\vec{b} = \frac{1}{3} < 11\bar{2}0 >$.

These dislocations are only found in sample $S1$. They increase the dislocation density in the vicinity of the SiO_2 mask. They are not observed in sample $S2$.

3. Since the overall dislocation density of $S2$ is lower than $S1$, it is preferable to deposit the SiO_2 mask onto the buffer layer and not directly on the sapphire.

Analysis of dislocations — The characterization of dislocations in the overgrown areas is made with the identification of their Burgers vector and the determination of the dislocation line ($\vec{u}$). For the identification of the Burgers vector, we need at least three micrographs with different reflections, where in two of them the dislocations have to be out of contrast. Figure 4.11 shows a set of micrographs under different diffraction condi-

tions.

The identification of the Burgers vector is determined for the four types of dislocations shown in Figure 4.11(a). Under $\vec{g} = (0002)$ diffraction condition, all the dislocations are not visible (Figure 4.11(b)), because they have their Burgers vector perpendicular to the c direction and they belong to in the $\vec{b} = \frac{1}{3} < 11\bar{2}0 >$ family. Table 4.2 shows the invisibility criterion of these dislocations $(\vec{g}.\vec{b})$.

$\vec{b}/\vec{g}$	$\frac{1}{3}[11\bar{2}0]$	$\frac{1}{3}[\bar{2}110]$	$\frac{1}{3}[1\bar{2}10]$
$(1\bar{2}10)$	$\bar{1}$	$\bar{1}$	2
(0002)	0	0	0
$(0\bar{1}11)$	1	0	1
$(\bar{1}101)$	0	1	$\bar{1}$
$(10\bar{1}\bar{3})$	1	$\bar{1}$	0

Table 4.2: *Invisibility criterion of dislocations in the overgrown areas $(\vec{g}.\vec{b})$.*

The dislocations marked with "1" and "4" are out of contrast with $\vec{g} = (0002)$ and $\vec{g} = (10\bar{1}\bar{3})$ reflections, and thus its Burgers vector $\vec{b}is\frac{1}{3}[1\bar{2}10]$. The dislocation number "2" is out of contrast under $\vec{g} = (0002)$ and $\vec{g} = (0\bar{1}11)$ diffraction conditions, and its $\vec{b}is\frac{1}{3}[\bar{2}110]$. Finally, the dislocation marked with "3" is out of contrast under $\vec{g} = (0002)$ and $\vec{g} = (\bar{1}101)$ diffraction conditions and its $\vec{b}is\frac{1}{3}[11\bar{2}0]$. The Burgers vector can also be determined by $\vec{g}_1 \times \vec{g}_2$, as is done below.

In order to determine the directions of the dislocation lines, the sterographic projection was used following the procedure described by Head [123]. To apply this method, at least two micrographs of defects are necessary under different diffraction conditions. In the micrographs, the $\vec{g}$ vector, the beam direction (B) and the projection of $\vec{u}$ have to be identified. The orientation map is given in Figure 4.12. The red crosses indicate the different reflections used for the identification of the dislocation line direction. The dislocation number "1" from the determination of the Burgers vector was used to give this example. This example is given in three indices, which can be changed to four indices using the equations from the Appendix D.

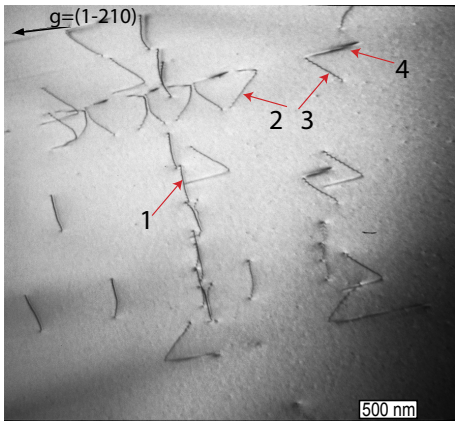

(a)

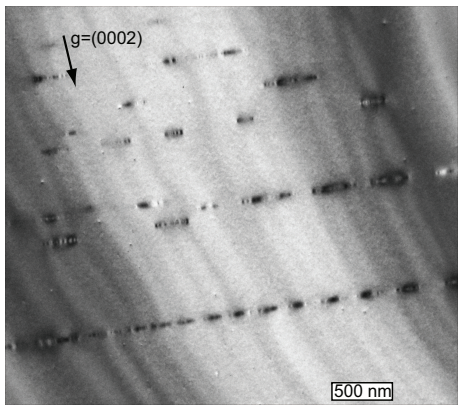

(b)

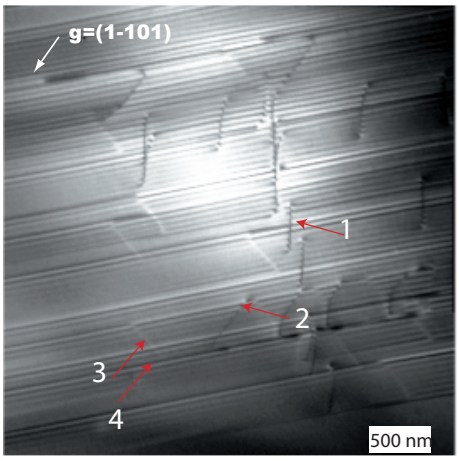

(c)

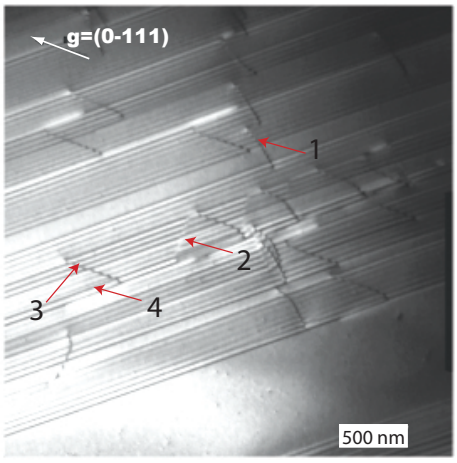

(d)

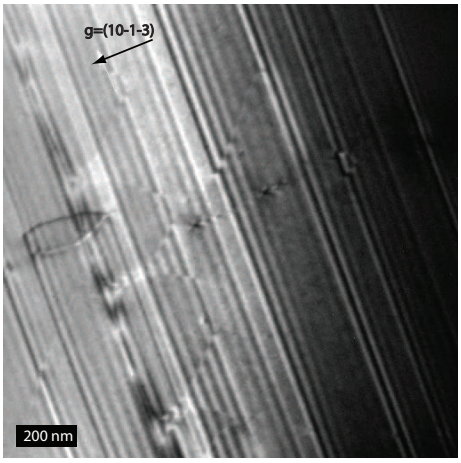

(e)

Figure 4.11: *Identification of the Burgers vector using the invisibility criterion. DF micrographs under several diffraction conditions: a)* $\vec{g} = (1\bar{2}10)$*, b)* $\vec{g} = (0002)$*, c)* $\vec{g} = (\bar{1}101)$*, d)* $\vec{g} = (0\bar{1}11)$ *and e)* $\vec{g} = (10\bar{1}\bar{3})$*.*

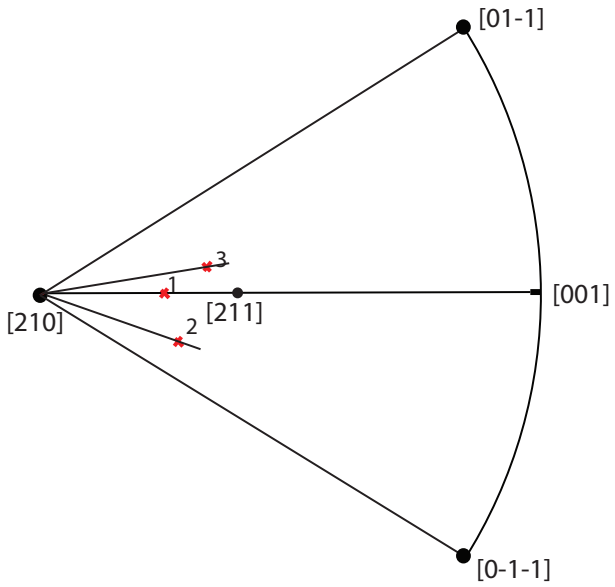

Figure 4.12: *Orientation map indicating the three reflections used to take the micrographs for the dislocation* "1".

In Figure 4.13 a set of micrographs and diffraction patterns is given. The direction of the $\vec{g}$ vector and the beam direction are obtained using the diffraction patterns. Each micrograph shows the dislocation (red ellipse), the $\vec{g}$ vector, the $\vec{u}$ projection (dashed line) and the beam direction of each diffraction pattern. In order to identify the direction of the $\vec{g}$ vector the diffraction pattern is rotated with respect to the micrographs, where the rotation depends on the magnification and the camera length. The diffraction patterns are taken with Kikuchi lines in order to index them and to find the beam direction. The transmitted beam is marked by x in the diffraction pattern of Figure 4.13. The dislocation line projection is taken from the dislocation in the micrographs. The angles between the dislocation line projection and the $\vec{g}$ vector for each micrograph are also shown in Figure 4.13.

In the stereographic projection shown in Figure 4.14, the great circles, corresponding to the $\vec{g}$ planes and the beam directions are shown. The beam direction are marked by 1, 2 and 3 which correspond to $B = [10\,5\,3]$, $B = [7\,2\,\overline{2}]$ and $B = [8\,5\,\overline{3}]$, respectively. For each plane the projected dislocation line is marked with a purple start at the corresponding angle from the diffracting vector.

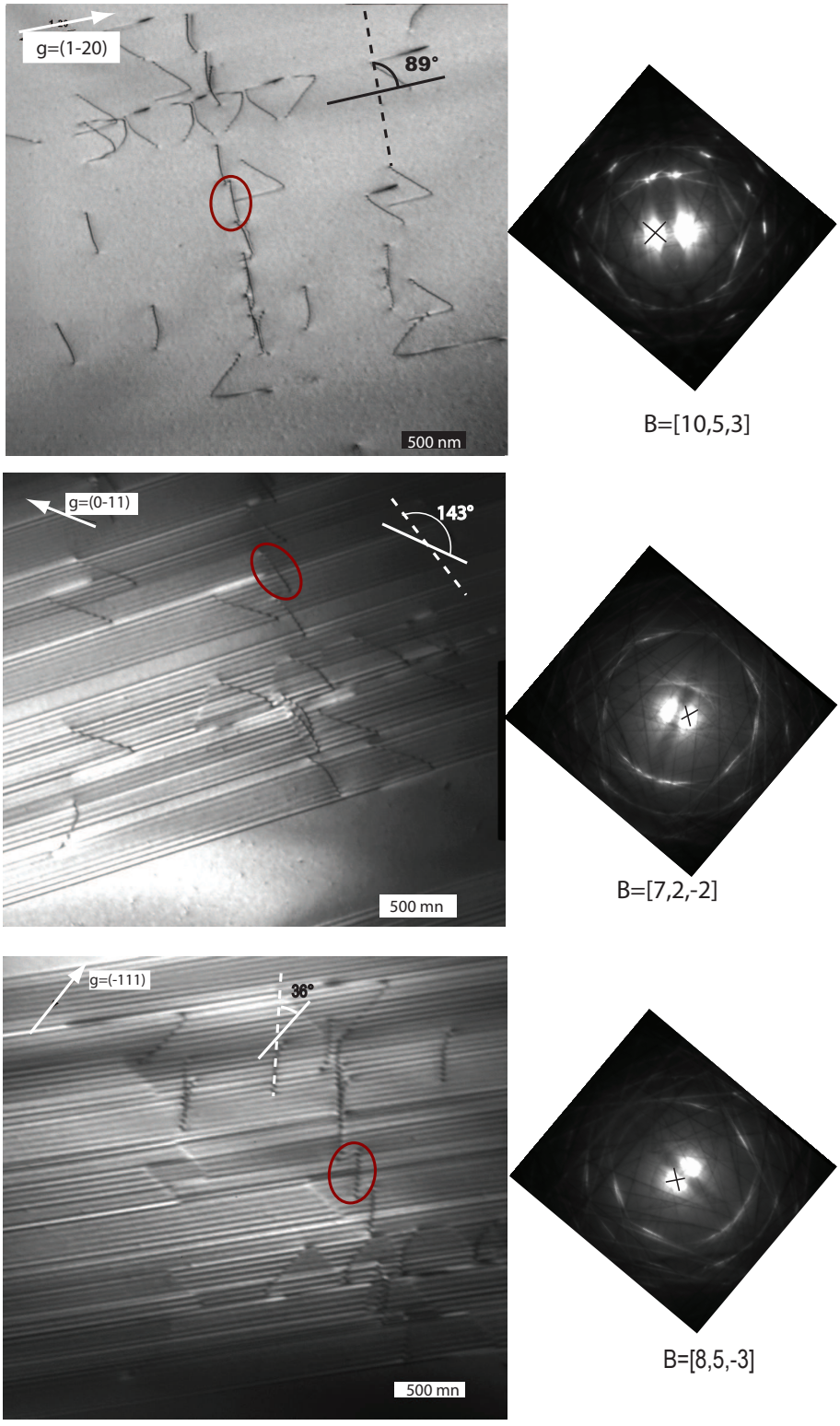

Figure 4.13: *Images of dislocations and diffraction patterns under different diffraction conditions: (a)* $\vec{g} = (1\bar{2}0)$ *and* $B = [10\,5\,3]$*, (b)* $\vec{g} = (0\bar{1}1)$ *and* $B = [7\,2\,\bar{2}]$*, and (c)* $\vec{g} = (\bar{1}11)$ *and* $B = [8\,5\,3]$*.*

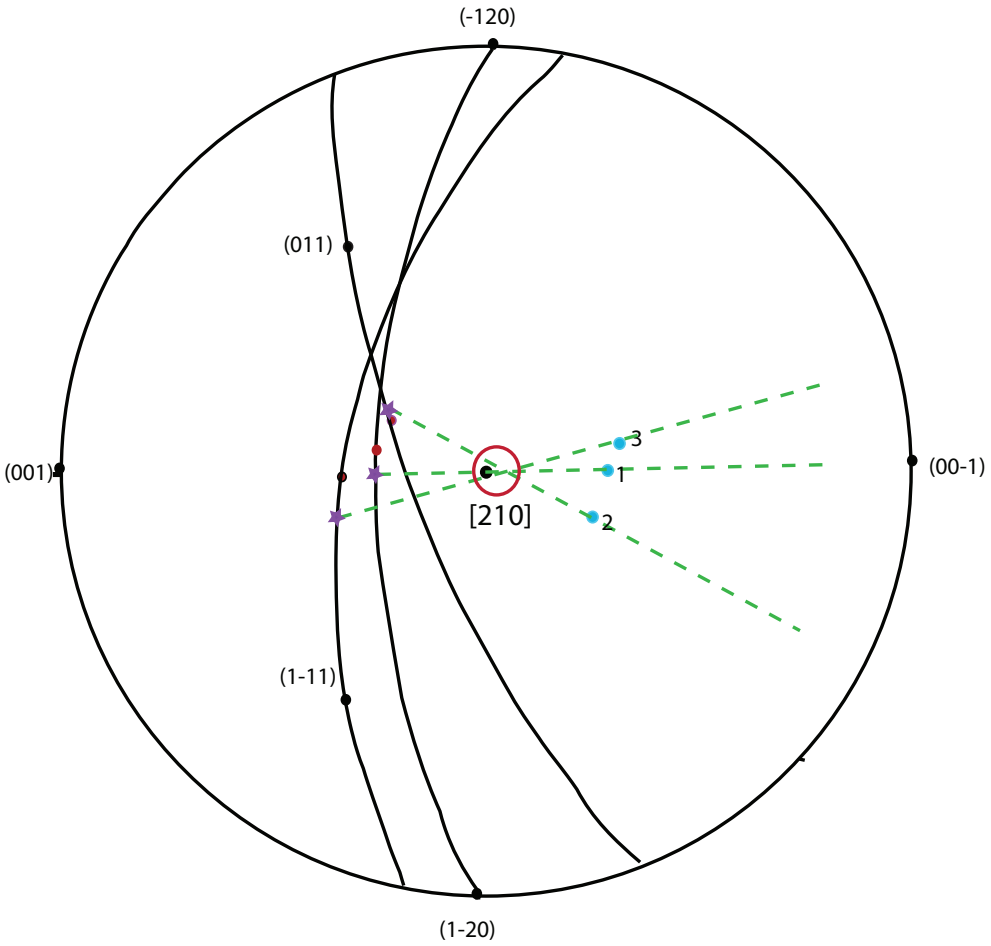

Figure 4.14: *Stereographic projection to illustrate the determination of the dislocation line: the blue points* 1, 2 *and* 3 *are the beam direction that correspond* $B = [10\,5\,3]$, $B = [7\,2\,\overline{2}]$ *and* $B = [8\,5\,\overline{3}]$ *respectively.*

The direction of $\vec{u}$ must lie in the plane containing the beam direction and the projection of $\vec{u}$ on that beam direction. This plane is constructed for each beam direction by drawing a circle containing the projected **u** and the beam direction (dashed lines). The area of intersection of the three circles defines the direction $\vec{u}$ (red circle).

The dislocation line of this kind of dislocations is close to [210] . Using the invisibility criterion in three different reflections, these dislocations are visible when $g_1 = (1\overline{2}0)$ and invisible when $g_2 = (002)$ and $g_3 = (10\overline{3})$. The direction of the Burgers vector is obtained

by the cross product of $\vec{g_2} \times \vec{g_3}$:

$$\mathbf{b} = \begin{pmatrix} h & k & l \\ 0 & 0 & 2 \\ 1 & 0 & \overline{3} \end{pmatrix} = [020]$$

The Burgers vector of these dislocations is $\vec{b} = [010]$. The Burgers vector is perpendicular to the dislocation line and therefore, we can conclude that these dislocations have an edge character.

Using the same procedure with the dislocation the other three dislocations of Figure 4.11, the characters have been identified as:

1. Dislocation "2": $\vec{b} = [\overline{1}00]$ and $\vec{u} = [12\overline{1}]$. The angle between $\vec{b}$ and $\vec{u}$ is 90^o and consequently, it has edge character.
2. Dislocation "3": $\vec{b} = [110]$ and $\vec{u} = [1\overline{11}]$. They are perpendicular to each other and hence, it has edge character.
3. Dislocation "4". It has screw character, because $\vec{u} = [010]$ is parallel to $\vec{b} = [010]$.

All the dislocations of the micrographs in this section are of one type of these four dislocation types. The dislocation line direction of the dislocations "2" and "3" have the same family of direction and they are 60^o to each other.

4.4.3 Dislocations in the coalesced areas

During the growth of the *a*-GaN film, the growth fronts coalesce above the SiO_2 mask forming a grain boundary. When two overgrowth fronts meet, a large void is formed above the mask (Figure 4.15). Though iit is believed that the formation of these voids is related to impurity accumulation at the meeting fronts [124], EDS chemical analysis performed around these voids has demonstrated that the impurity concentration was below the detection limit. BF micrograph taken under $\vec{g} = (1\overline{2}10)$ diffraction condition (Figure 4.15) close to the $[10\overline{1}0]$ zone axis shows a $\approx 3.5 \times 1\,\mu m$ void above the SiO_2 mask. Figure 4.15 shows a high dislocation density around the void and that the front

growing in $[000\bar{1}]$ direction is vertical. The material contamination observed inside the void most likely results of the deposition of some material during polishing.

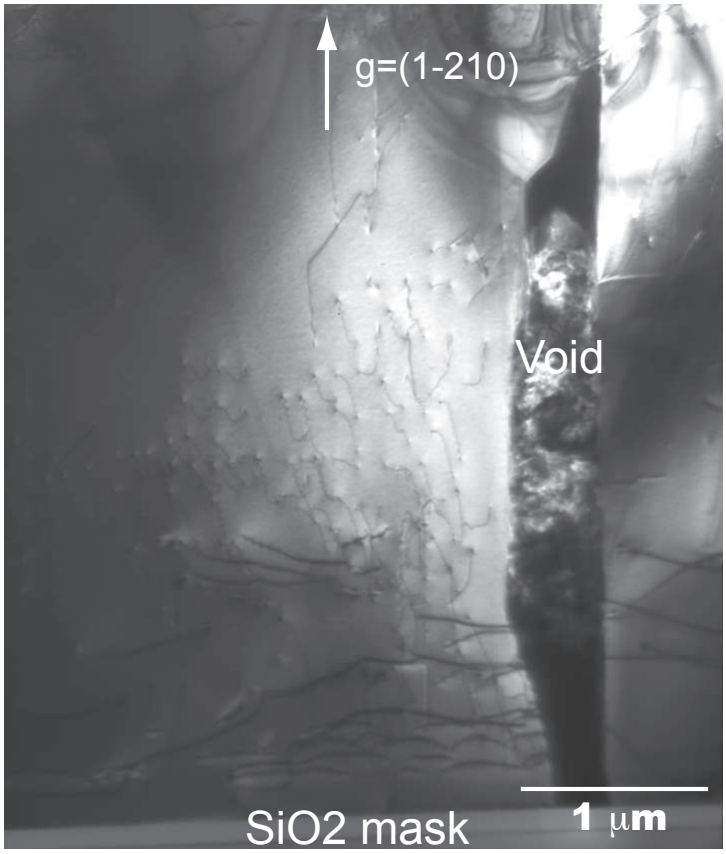

Figure 4.15: *BF micrograph under $\vec{g} = (1\bar{2}10)$ diffraction condition of a void above the SiO_2 mask which is originated during the coalescence of the two fronts in a-GaN layer. High density of dislocation is found around the void.*

The grain boundary formed at the meeting fronts above the SiO_2 mask is shown in Figure 4.16. It has been observed by SAED that this area is distorted. This distortion is due to the strain attributed to the formation of the grain and/or of the new dislocations around the void. A small misorientation of $1 - 2^o$ between the two meeting growth fronts was observed using diffraction patterns taken on both sides of the grain boundary. This misorientation was also found in c-GaN films by Gradecak [55]. The grain boundary consists of a network of dislocations as shown in the magnified image of Figure 4.16. In this image, one can observe a difference in contrast between the two grains, due to their small misorientation.

High dislocation density has been observed in the grain boundary area. TEM observations have shown that dislocations with a Burgers vector $\vec{b} = \frac{1}{3} < 11\bar{2}0 >$ and $\vec{b} = \frac{1}{3} < 11\bar{2}3 >$ are present in the meeting front areas. The dislocations with $\vec{b} = \frac{1}{3} < 11\bar{2}0 >$ are invisible under $\vec{g} = (0002)$ diffraction condition and the dislocations with $\vec{b} = \frac{1}{3} < 11\bar{2}3 >$ are visible under $\vec{g} = (1\bar{2}10)$ and $\vec{g} = (0002)$ diffraction conditions.

Dislocations pointed by black arrows (Figure 4.16), have a Burgers vector $\vec{b} = \frac{1}{3}[\bar{1}2\bar{1}0]$. They are visible under $\vec{g} = (1\bar{2}10)$ diffraction condition and invisible under $\vec{g} = (0002)$ and $\vec{g} = (10\bar{1}3)$ diffraction conditions.

The growth front directions have been determined by comparing experimental and simulated convergent beam electron diffraction (CBED) patterns (Figures 4.16(b) and 4.16(c)). The experimental CBED pattern was taken on the right side of the grain boundary where $[10\bar{1}0]$ zone axis has been used to study the sense of the *c*-direction. A good match with the experimental and the simulated CBED patterns is obtained when the film thickness is 183 nm.

Thickness fringes are not observable in Figure 4.16 because their periodicity corresponds to an extinction distance of 220 nm at $\vec{g} = (1\bar{2}10)$ (JEMS [119]). The thickness of the sample is smaller than the extinction distance at this particular Bragg diffraction condition. The extinction distance is larger that the thickness of the sample that no fringes can be observed in the film. For this reason, the $\vec{g} = (1\bar{2}10)$ is the most common reflection used to obtain a clear image without fringes.

4.4.4 Discussion

The dislocation analysis of the two types of samples of this work has shown a high threading dislocation density in the window areas, $1 \times 10^{10}\, cm^{-2}$ (mask aligned parallel to the $[10\bar{1}0]$). They have screw and mixed characters with Burgers vector $\vec{b} = \frac{1}{3}[11\bar{2}0]$ and $\vec{b} = \frac{1}{3}[11\bar{2}3]$ respectively. The threading dislocations in the window areas do not bend to the lateral overgrown as they do in c-GaN [110] . They go straight torwards the surface. When the SiO_2 mask is aligned along [0001] direction, the threading dislocations in the

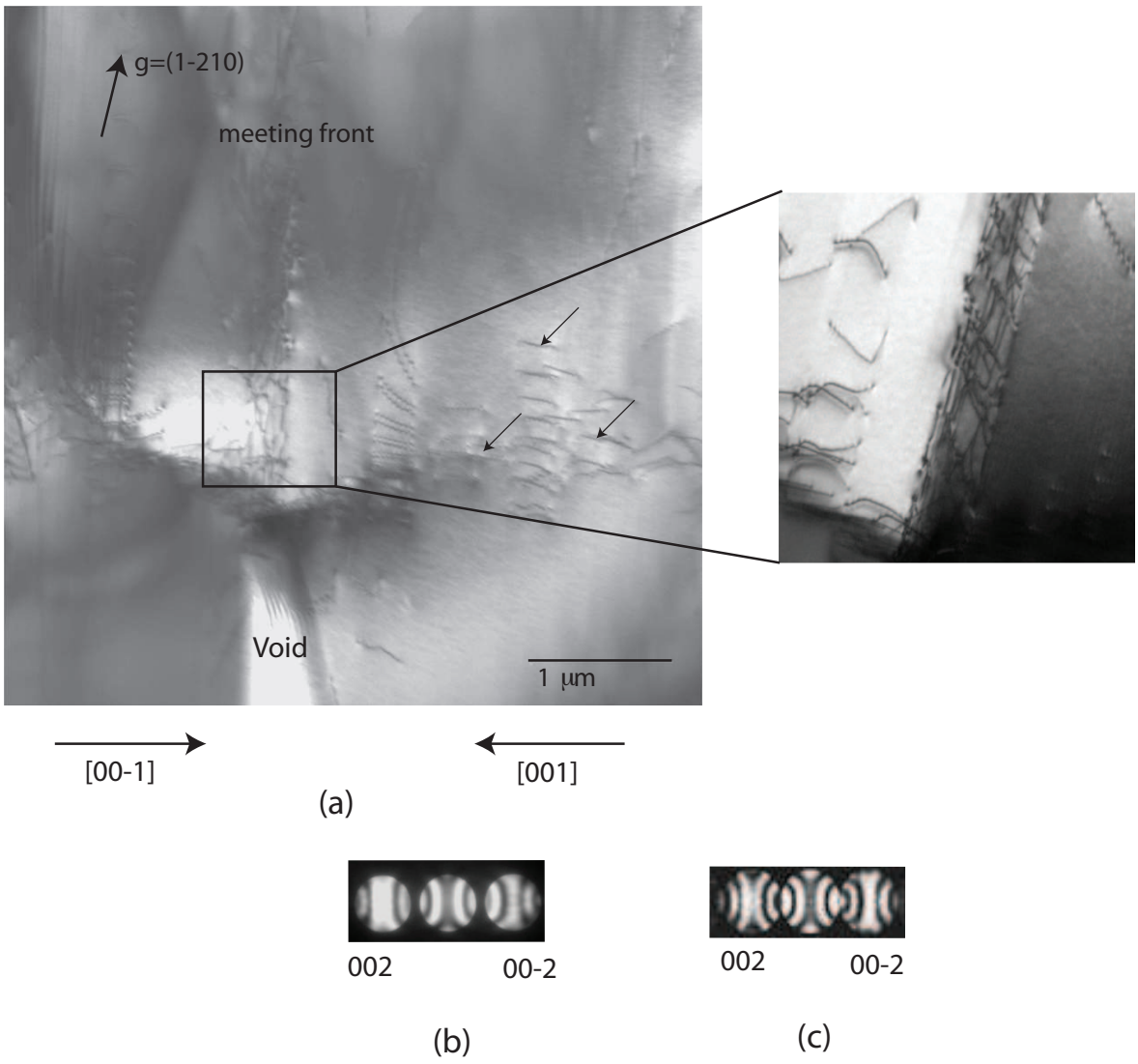

Figure 4.16: *a) BF micrograph under* $\vec{g} = (1\bar{2}10)$ *diffraction condition of the grain boundary on the meeting fronts. The inset shows the network of dislocations and the change in contrast is due to a small misorientation. Black arrows show dislocations with* $\vec{b} = \frac{1}{3}[\bar{1}2\bar{1}0]$. *b) and c) experimental and simulated CBED patterns give the sense of the growth directions, they fit for a thickness of 183nm.*

window areas bend only 30^o to the lateral areas as is described by Haskell et al. [125]. For this reason, the dislocation density in window areas is reduced from $10^{10}\,cm^{-2}$ to $10^7\,cm^{-2}$, but in the lateral areas the dislocation density is increased from $10^6\,cm^{-2}$ to $10^9\,cm^{-2}$. Bending dislocations phenomena cannot be used in the growth of a-GaN layers, because the dislocations in a-GaN do not bend 90^o like they do in c-GaN films.

In this section it has been shown that the quality in the overgrown areas has been improved with the implementation of the ELO technique, which allows the reduction of the dislocation density from 1×10^{10} to $\approx 3 \times 10^8\,cm^{-2}$. This is in a good agreement with MOCVD-ELO results obtained by Chen et al. [11], the dislocation densities are $1 \times 10^{10}\,cm^{-2}$ and $1 \times 10^8\,cm^{-2}$, window and overgrown areas respectively.

Haskell et al. [14] obtained a lower dislocation density of a-GaN films grown on r-sapphire by HVPE-ELO at $\approx 1040\,^oK$ and $V/III = 40$. These densities are $\approx 9 \times 10^9\,cm^{-2}$ and $5 \times 10^6\,cm^{-2}$, window and overgrown areas respectively. The order of magnitude can change depending on the thickness of the layer. In this work the thickness of GaN layers was $\approx 20\,\mu m$ and for Haskell was $\approx 53\,\mu m$. Therefore, depending on the thickness of the layer, the dislocation density varies.

Different dislocations have been found in the lateral areas. They are in the basal plane and have different characters: screw character with $\vec{b} = \frac{1}{3}[11\bar{2}0]$, edge character with $\vec{b} = \frac{1}{3}[2\bar{1}\bar{1}0]$, edge character with $\vec{b} = \frac{1}{3}[\bar{1}2\bar{1}0]$, Shockley partial dislocations with $\vec{b} = \frac{1}{3} < 10\bar{1}0 >$ and Frank partial dislocations with $\vec{b} = \frac{1}{6} < 20\bar{2}3 >$.

In the coalesced areas, a low angle grain boundary is formed when the two fronts meet with a small misorientation of 1 to 2^o like it occurs in c-GaN [55]. The grain boundary is a network of dislocations with Burgers vector $\vec{b} = \frac{1}{3}[11\bar{2}0]$ and $\vec{b} = \frac{1}{3}[11\bar{2}3]$. A void is observed under the meeting fronts due to the high dislocation density originated in this area, but the incorporation of impurities above the mask could not be confirmed.

According to the results obtained from the comparison of the overgrown areas of the two types of samples ($S1$ and $S2$), the deposition of the buffer layer is of significant importance in order to avoid the formation of dislocations near the SiO_2.

4.5 Planar defects and partial dislocations in a-plane GaN films.

Planar defects such as basal stacking faults (BSFs), prismatic stacking faults (PSFs), inversion domain boundaries (IDBs) and $(10\bar{1}0)$-stacking faults have been observed in GaN specimens. The analysis of the partial dislocations has been done together with the analysis of the SFs in order to identify these SFs. a-plane GaN films have a higher BSFs density compared to c-GaN. These BSFs propagate towards the surface and are not parallel to the GaN/sapphire interface like they are in *c*-plane GaN. A detailed analysis of SFs has to be carried out in order to know how they affect the optical properties, contrary to c-GaN where SFs are rarely observed and are parallel to the SiO_2 mask.

4.5.1 Basal stacking faults and their related partial dislocations

BSFs are formed at the GaN/sapphire and GaN/SiO_2 interfaces. In the window areas, SFs are created by the coalescence of the growth islands and imperfections or obstacles on the sapphire substrate. In this work, we have shown that the sapphire has imperfections that create steps and stacking faults at the interface. The basal stacking fault density was measured in both the window and overgrown regions of the $S1$ and $S2$ types of samples. In the window areas, in all the samples the SF density is of the order of $1 \times 10^6\, cm^{-1}$. In the overgrown areas, the staking fault densities of the $S1$ and $S2$ samples are $6 \times 10^4\, cm^{-1}$ and $4 \times 10^4\, cm^{-1}$ respectively. The density of the $S2$ samples is slightly smaller than that of the $S1$ samples.

According to the classification of stacking faults in GaN wurtzite structure (Section 3.4.2), the basal stacking faults are either I_1, I_2, I_3 or E type. The I_3-BSFs ($ABABCBAB$), first reported by Stampfl et al. [126], has the second lowest energy and can be formed by a combination of two I_2 BSFs. These BSFs are not observed in this work.

The stacking faults in GaN films can be considered as the wurtzite-zincblende transitions, where the wurtzite structure has one atomic layer of zincblende for I_1, two for I_2 and three

for E. For the determination of the displacement vector $\vec{R}$ of these BSFs, the invisibility criterion $2\pi\vec{g}.\vec{R} = 0\, or\, 2n\pi$ $(n \in integer)$ is used.

BSFs in the a-GaN films are visible under $\vec{g} = (0\bar{1}11)$ diffraction condition (Figure 4.17(a)) , but they are out of contrast under $\vec{g} = (0002)$ and $\vec{g} = (1\bar{2}10)$ diffraction conditions (Figures 4.17(b) and 4.17(c) respectively).

Frank partial dislocations are associated with I_1-BSFs and Shockley partial dislocations are associated with I_2-BSFs which can result in strain relaxation. The invisibility criterion for both types of BSFs (I_1 and I_2) is similar, and consequently it cannot be used as a criterion to distinguish them. In order to distinguish I_1 or I_2 BSFs, the identification of the I_2-partial dislocations is required.

I_1-BSFs have a lower stacking fault energy than the other stacking faults of the basal plane. I_1-BSFs have a displacement vector $\vec{R} = \frac{1}{6} < 20\bar{2}3 >$ and are bounded by Frank partial dislocations with Burgers vector $\vec{b} = \frac{1}{6} < 20\bar{2}3 >$. Drum [127] found that I_1-BSFs give contrast with $\vec{g} = (01\bar{1}0)$ and $\vec{g} = (02\bar{2}0)$ reflections, but they are out of contrast with $\vec{g} = (03\bar{3}0)$ reflection (Figure 4.18). In Figure 4.18(c), the contrast observed is due to the fact that the planes $(01\bar{1}0)$, $(02\bar{2}0)$ and $(03\bar{3}0)$ are close to each other and they both contribute to the contrast.

I_1-BSFs can end at either Frank partial dislocations or prismatic stacking faults. These two defects are observed in Figure 4.18. The partial dislocation is marked by 1 and the PSF by 2, where the PSF is found at the end of two I_1-BSFs.

The identification of I_1-BSFs using the invisibility criterion (two beams condition), was confirmed by HRTEM. Figure 4.19 shows an atomic resolution micrograph of a BSF taken along the $[2\bar{1}\bar{1}0]$ zone axis. The normal stacking sequence $ABABABAB\ldots$ of the wurtzite structure switches to the I_1 intrinsic BSF $ABABCBCB\ldots$. I_1-BSFs have a larger probability of formation because they have lower energy than I_2-BSFs and E-BSFs [128].

I_2-BSFs are observed in a-GaN layers, which are bounded by two Shockly partial dislocations. A HRTEM micrograph of I_2-BSF taken in $[2\bar{1}\bar{1}0]$ zone axis is shown in Figure

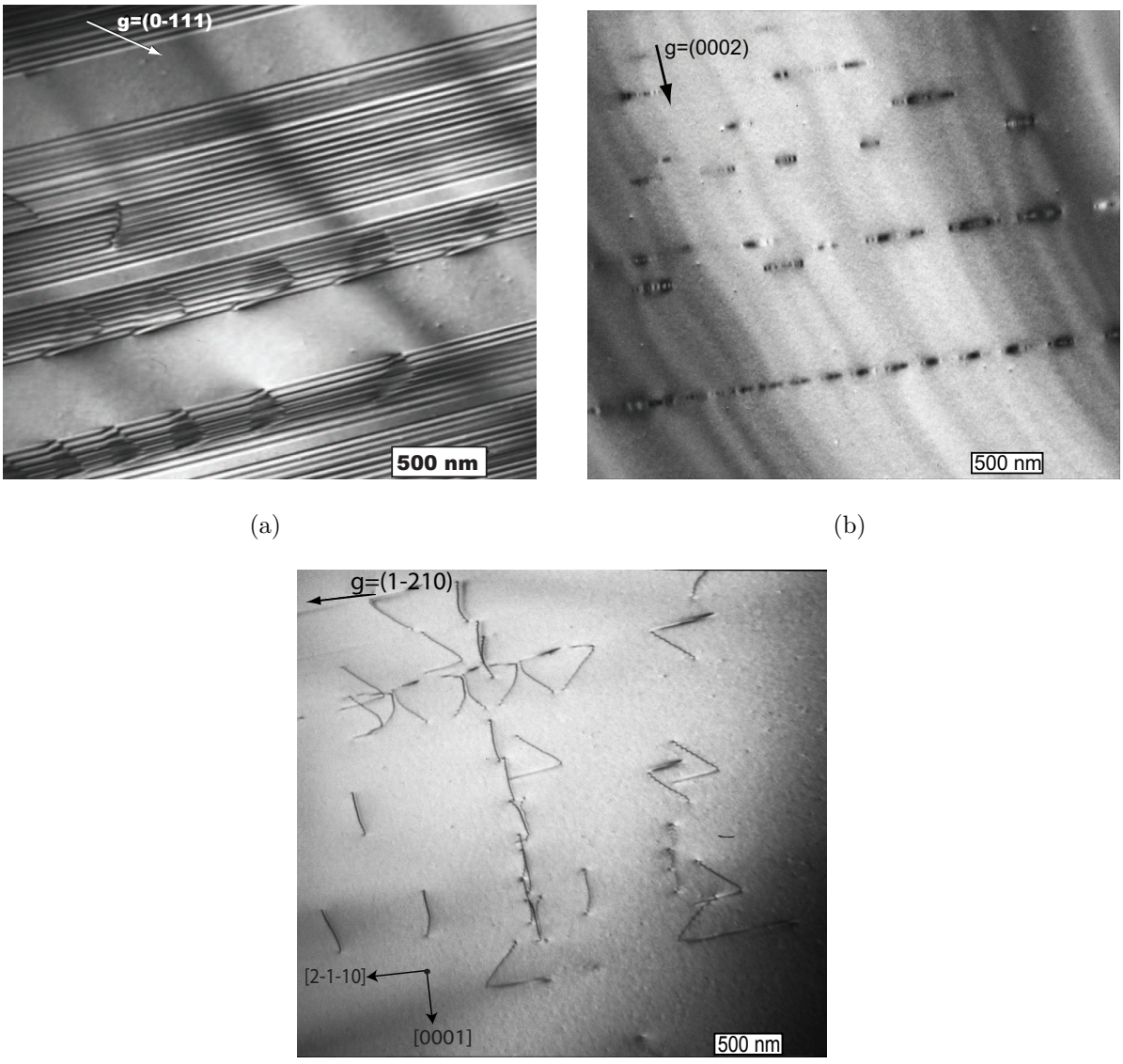

Figure 4.17: *The stacking faults in a typical overgrown area are identified using the invisibility criterion: a) DF micrograph under* $\vec{g} = (0\bar{1}11)$ *diffraction condition, b) DF micrograph under* $\vec{g} = (0002)$ *diffraction condition and c) DF micrograph under* $\vec{g} = (1\bar{2}10)$ *diffraction condition.*

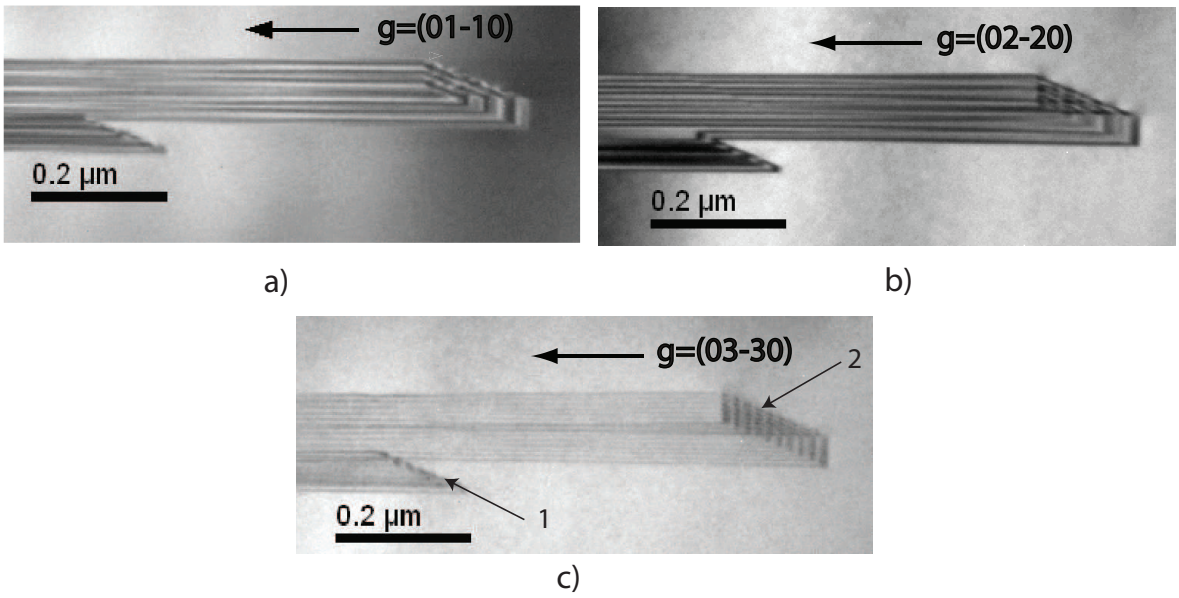

Figure 4.18: *Identification of the I_1 basal stacking faults: a) $\vec{g} = (01\bar{1}0)$, b) $\vec{g} = (02\bar{2}0)$ and $\vec{g} = (03\bar{3}0)$. "1" is a Frank partial dislocation and "2" is a PSF.*

4.20(a). The I_2-BSFs are observed with a displacement vector of $\vec{R} = \frac{2}{3} < 10\bar{1}0 >$ (Figure 4.20(b)), and are bounded by two Shockley partial dislocations with Burgers vector $\vec{b} = \frac{1}{3} < 1\bar{1}00 >$. The stacking sequence changes from $ABABAB\ldots$ (wurzite structure) to $ABABCACAC\ldots$ (I_2-BSF). The white lines and points in this figure show the position of the partial dislocations and the stacking sequence, respectively. A magnified and filtered portion of Figure 4.20(a) is shown in Figure 4.20(b). It shows the Burgers circuits (black spots) around the partial dislocations. These circuits indicate the direction of the Burgers vectors. The distance between the partial dislocations is ≈ 5 nm. It was calculated with the number of planes between the partial dislocations (18) multiplied by the interplanar spacing of the $(1\bar{1}00)$ planes (0.2761 nm).

The Burgers vector $\vec{b}$ of the perfect dislocation is $\frac{1}{3} < 11\bar{2}0 >$ and of the Shockley partial dislocation is $\frac{1}{3} < 10\bar{1}0 >$. Equation 4.2 gives a Burgers vector reaction of the dissociation of a perfect dislocation $\vec{b} = \frac{1}{3} < 11\bar{2}0 >$ into two Shockley partials of type $\vec{b} = \frac{1}{3} < 10\bar{1}0 >$ [128]:

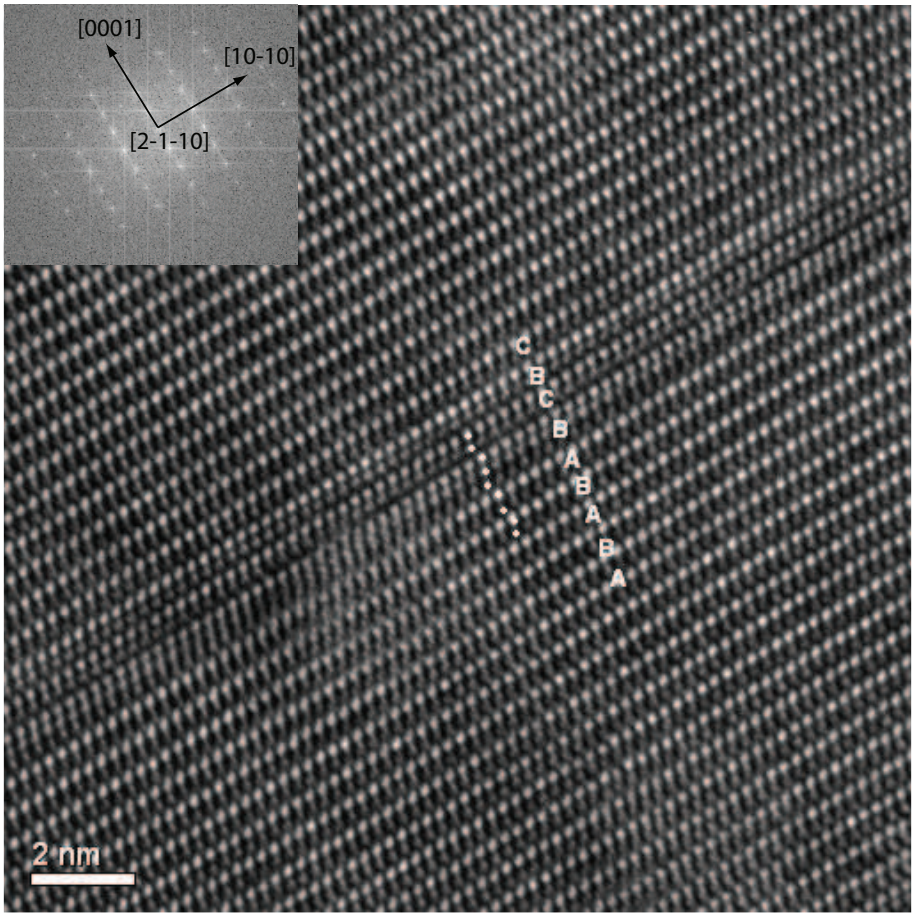

Figure 4.19: *HRTEM micrograph of a-GaN taken along the* $[2\bar{1}\bar{1}0]$ *zone axis.* I_1 *basal stacking fault originated during the growth at the interface. The stacking sequence along the* [0001] *direction is ABABABCBCB... where the positions are shown with white points.*

$$\frac{1}{3}[1\bar{2}10] \rightarrow \frac{1}{3}[1\bar{1}00] + \frac{1}{3}[0\bar{1}10] \tag{4.2}$$

The Burgers vectors of the Shockley dislocations are oriented 60^o to each other (Figure 4.21), at $\pm 30^o$ of the Burgers vector of the perfect dislocation. In order to know if the splitting reaction (Equation 4.2) is energetically favorable, we applied the Franks rule. Franks rule states that $b^2 > {b_1}^2 + {b_2}^2$, where b^2 is the energy of the perfect dislocation which is a^2 and ${b_1}^2 + {b_2}^2$ is the sum of the energies of the two partial dislocations which is $\frac{2a^2}{3}$. The dissociation involved in this reaction is favorable, since $a^2 > \frac{2a^2}{3}$.

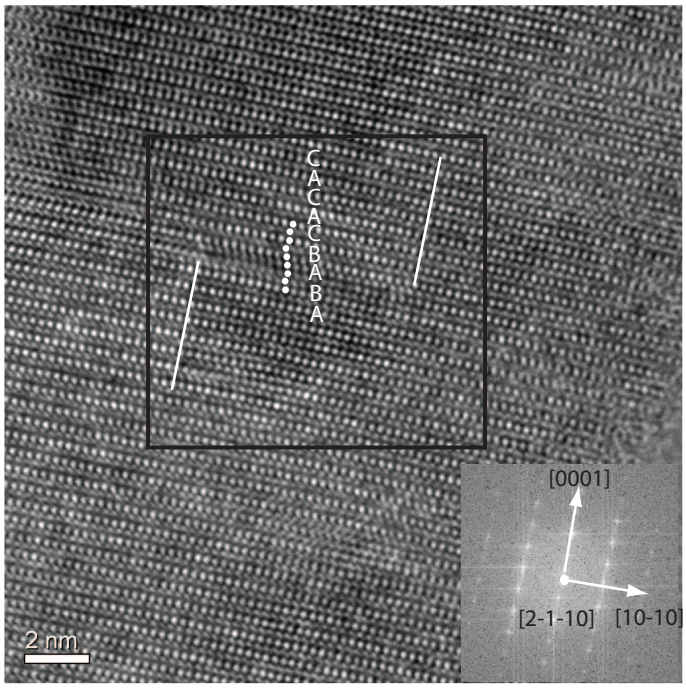

(a)

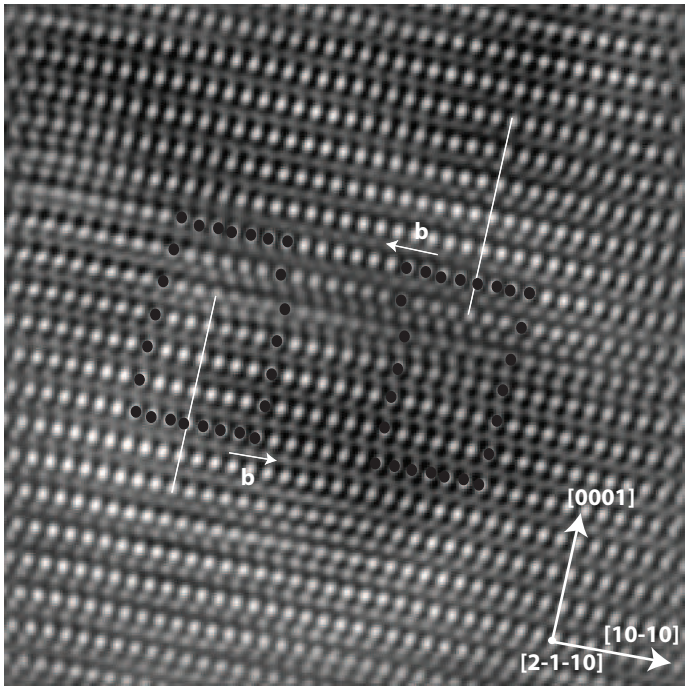

(b)

Figure 4.20: *HRTEM micrographs of I_2 basal stacking fault bound by two partial dislocations; a) the stacking sequence changes along the* [0001] *direction to $ABABCACAC$ and b) magnified and filtered portion of Figure 4.20(a), showing the direction of the Burgers vectors of the Shockley partials. The distance between dislocations is $\approx 5\,nm$.*

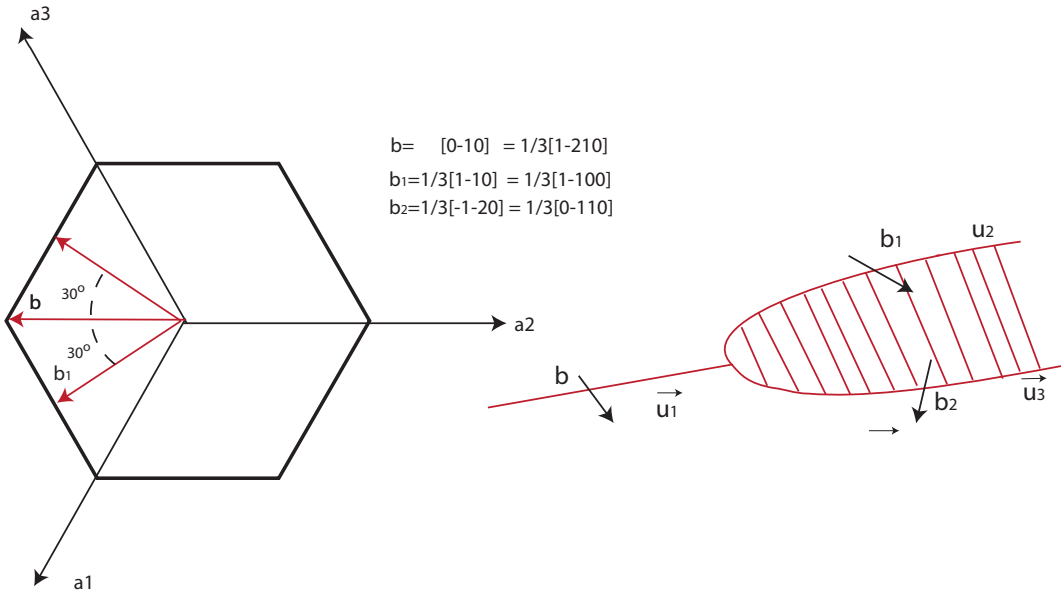

Figure 4.21: *A perfect dislocation* $\vec{b} = \frac{1}{3}[1\bar{2}10]$ *is dissociated into two Shockley partial dislocation with* $\vec{b} = \frac{1}{3}[1\bar{1}00]$ *and* $\vec{b} = \frac{1}{3}[0\bar{1}10]$ *respectively in the basal plane, where* $\vec{b} = \vec{b}_1 + \vec{b}_2$. *The angle between the two partials is* 60^o.

Assuming that the equilibrium is reached, it is possible to estimate the stacking fault energy γ using the measured distance between the two partial dislocations. Because the basal plane in hexagonal system is isotropic, a good approximation [128] is given by the equation 4.3:

$$\gamma = \frac{\mu b^2}{4\pi d} = \frac{\mu a^2}{12\pi d} \tag{4.3}$$

where μ is the shear modulus, $b^2 = \frac{a^2}{3}$ for Shockley dislocations, $a = 0.319\ nm$ is the lattice constant of GaN and d is the distance between the two partials. Using different shear modulus available from the literature, the stacking energy γ was calculated using the distance measured ($d = 5nm$) of Figure 4.20. It ranges from 43 to 56 erg/cm^2. Table 4.3 shows the different energies calculated with the different shear modulus μ.

These results compare well with reported values given in the literature by Zakharov et al. [33].

μ (GPa)	γ in this work (erg/cm^2)	γ [33] (erg/cm^2)
81.4 exp. [129]	43.66	40
91 cal. [130]	48.81	46.7
95 cal. [131]	50.96	
105 exp. [132]	56.33	52

Table 4.3: *Shear modulus and calculated I_2 stacking fault energies*

4.5.2 $(11\bar{2}0)$-Prismatic stacking faults

$(11\bar{2}0)$-prismatic stacking faults (PSFs) have been observed in a-GaN films. It has been observed that they are located at the end of two I_1-stacking faults [127]. The atomic arrangement between the two basal stacking faults forms the $(11\bar{2}0)$-stacking fault (Figure 4.22), where the PSFs are tilted 60^o from the surface normal [33].

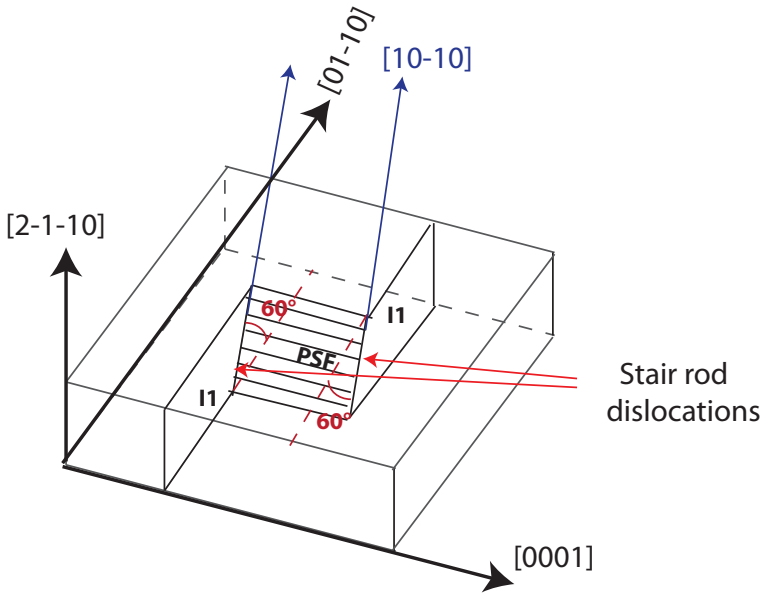

Figure 4.22: *Schematic representation of a PSF which is located at the end of two I_1-basal stacking fault.*

A bright field micrograph obtained under $\vec{g} = (1\bar{2}10)$ diffraction condition for a PSF is shown in Figure 4.23(a). Using the invisibility criterion, this prismatic fault has a

displacement vector $\vec{R} = \frac{1}{2}[1\bar{1}01]$. The PSFs give contrast, when reflections like $\vec{g} = (1\bar{2}10)$, $\vec{g} = (01\bar{1}0)$ and $\vec{g} = (03\bar{3}0)$ are selected and they are invisible under $\vec{g} = (0002)$ and $\vec{g} = (02\bar{2}0)$ diffraction conditions.

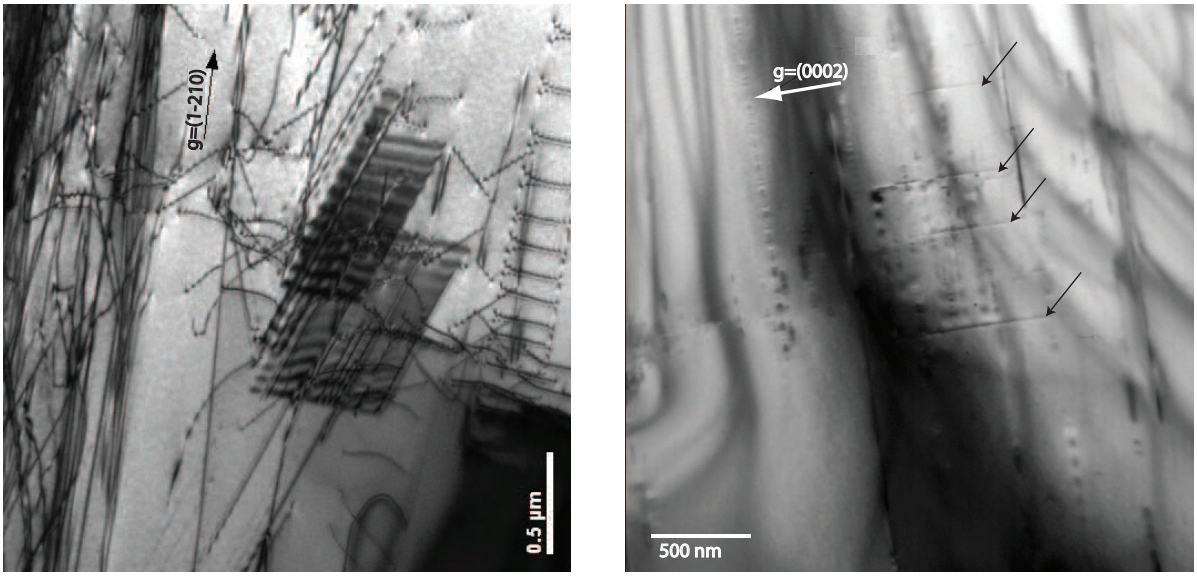

(a) (b)

Figure 4.23: $(11\bar{2}0)$*-prismatic stacking faults: a) BF micrograph under* $\vec{g} = (1\bar{2}10)$ *diffraction condition shows PSFs and b) BF micrograph under* $\vec{g} = (0002)$ *diffraction condition shows stair rods dislocations pointed by black arrows which are visible. PSFs are not visible in this diffraction condition.*

Since the displacement vectors from the I_1-BSFs and PSF are different, a stair rod dislocation (SRD) is expected to be formed at the intersection of the two faults. SRDs give contrast like a straight dark line (Figure 4.23(b)) under $\vec{g} = (0002)$ diffraction condition. The Burger vector of the stair rod dislocations is obtained by the difference between the displacement vector of the I_1-BSF ($\vec{R} = \frac{1}{6} < 20\bar{2}3 >$) and the $(11\bar{2}0)$-PSF ($\vec{R} = \frac{1}{2} < 1\bar{1}01 >$) [33]. The Burgers vector of the stair rod dislocations is $\vec{b} = \frac{1}{6} < 10\bar{1}0 >$ which has screw orientation.

A HRTEM micrograph of a PSF along the $[2\bar{1}\bar{1}0]$ zone axis is shown in Figure 4.24. The prismatic stacking fault is located at the end of the two I_1-BSFs. The inset of Figure 4.24 shows a Fourier filtered magnified image of the faulted area. The atomic arrangement

in the PSF looks like hexagonal contrast [33] with a stacking sequence of $ACACAC\ldots$. In the magnified image, the hexagonal contrast (red hexagon) is easily observed, which confirms that it is a PSF.

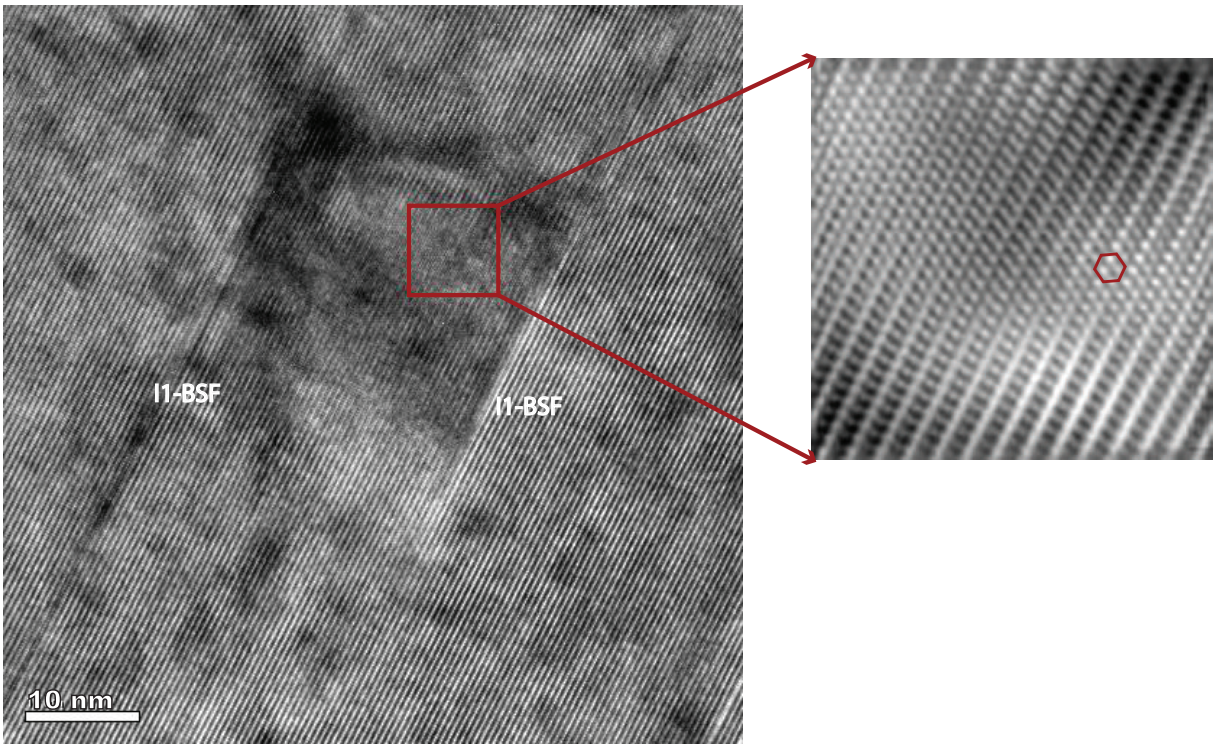

Figure 4.24: *HRTEM micrograph along* $[2\bar{1}\bar{1}0]$ *zone axis of a PSF bounded by two* I_1*-BSFs. The inset is a magnified image inside of the prismatic stacking fault which gives a hexagonal contrast (ACAC..).*

4.5.3 Domains boundaries in a-GaN thin films.

A plan-view DF micrograph taken under $\vec{g} = (0002)$ diffraction condition is shown in Figure 4.25. It shows a domain located in the window area from the $S2$ samples. The domain is not visible under $\vec{g} = (1\bar{2}10)$ and $\vec{g} = (02\bar{2}0)$ diffraction conditions and presents a strong contrast under $\vec{g} = (0002)$ diffraction condition. This domain is parallel to the 0001 direction.

Domains in GaN films are inversion domain boundaries or stacking domains. The domain

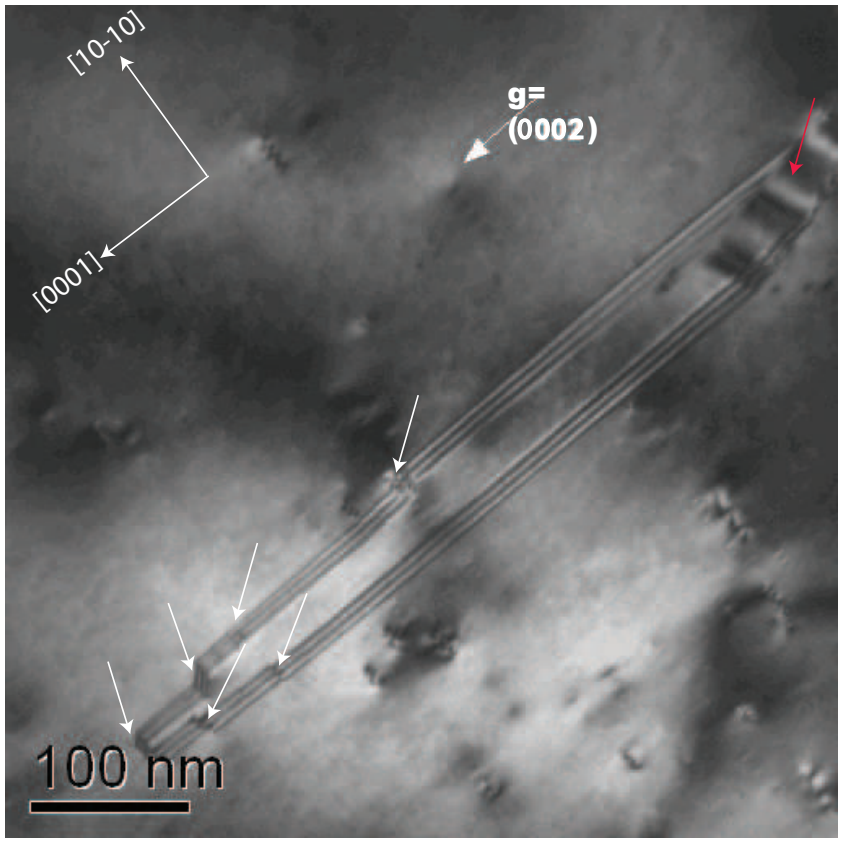

Figure 4.25: *DF micrograph taken under* $\vec{g} = (0002)$ *diffraction condition of a domain along* [0001] *direction. White arrows show the position of basal stacking faults and red one prismatic stacking fault.*

shown in Figure 4.25 was suspected to be a IDB and therefore, multiple dark beam (MDB) and CBED were carried out.

Inversion domain boundaries (IDB) are typical defects for non-centrosymmetric crystals and are formed during the growth of the GaN layer on sapphire [24, 133]. The cation and anion positions are interchanged in the IDBs. In materials with wurtzite structure, two kinds of domains boundaries have been observed on $\{10\bar{1}0\}$ and $\{11\bar{2}0\}$ planes [134–136]. The inversion domains in the $\{11\bar{2}0\}$ plane are also called prismatic stacking faults which have been described in the previous section (Section 4.5.2). Inversion domain boundaries in the $\{10\bar{1}0\}$ plane originate at the epilayer/substrate interface, and go along [0001] direction parallel to the sapphire [135, 136]. They are obtained by interchanging the chemical identity of atoms on one side of the $(11\bar{2}0)$ plane followed by a translation of the

inverted region by $\vec{R} = \frac{1}{3}[0001]$.

Multiple beam dark field (MDF) is a technique used to study IDBs in GaN films. It presents complementary contrast for $+\vec{g}$ and $-\vec{g}$ reflections [137]. A plan-view MDF micrographs close to the $[2\overline{1}\overline{1}0]$ zone axis, under $\vec{g} = (0002)$ and $\vec{g} = (000\overline{2})$ diffraction conditions, are presented in Figures 4.26(a) and 4.26(b) respectively. They show a domain which intercepts many BSFs. The micrographs from this figure do not have a complementary contrast indicating that this defect could not be an inversion domain.

Convergent beam electron diffraction (CBED) was used to confirm if there is a polarity change between the matrix and the domain. For CBED, $[10\overline{1}0]$ zone axis was used because it allows $\vec{g} = (0002)$ and $(000\overline{2})$ reflections to be distinguished. The experimental CBED patterns were taken in two places: in the matrix at position *1* and in the domain at position *2* (Figure 4.26(a)). The CBED experimental patterns taken at position *1* and *2* and the simulated CBED pattern are shown in Figure 4.26(c). A polarity change appears when there is a contrast inversion in the CBED patterns. The experimental CBED patterns in the two positions show a difference in contrast between them. Comparing the experimental with the simulated CBED patterns, the difference in contrast is given for a thickness variation. In position 1 and 2, the experimental CBED patterns fit with the simulated patterns for a thickness of 180 nm and 130 nm respectively. Therefore, this domain is not an inversion domain boundary. Since matrix and domain have the same polarity, the defect is a closed stacking fault which lies in $(10\overline{1}0)$-prismatic plane. These defects, occasionally observed in the GaN films, form closed domains and are called stacking mismatch boundary [138].

At the stacking mismatch boundary, the stacking sequence of the atomic layers is reversed ($ABCBCB$...), but Ga and N are not interchanged. This change leads to significant disruption in the bounding at the boundary [138]. The boundary lies in $(10\overline{1}0)$-plane and connects two stacking faults on the left or right side of the boundary (Figure 4.27). The bond length between the Ga and N in the boundary is 1.81 Å, i.e. a contraction of 7% compared to the bulk bond length.

The stacking fault domain of Figure 4.25 is formed by three different stacking faults, those

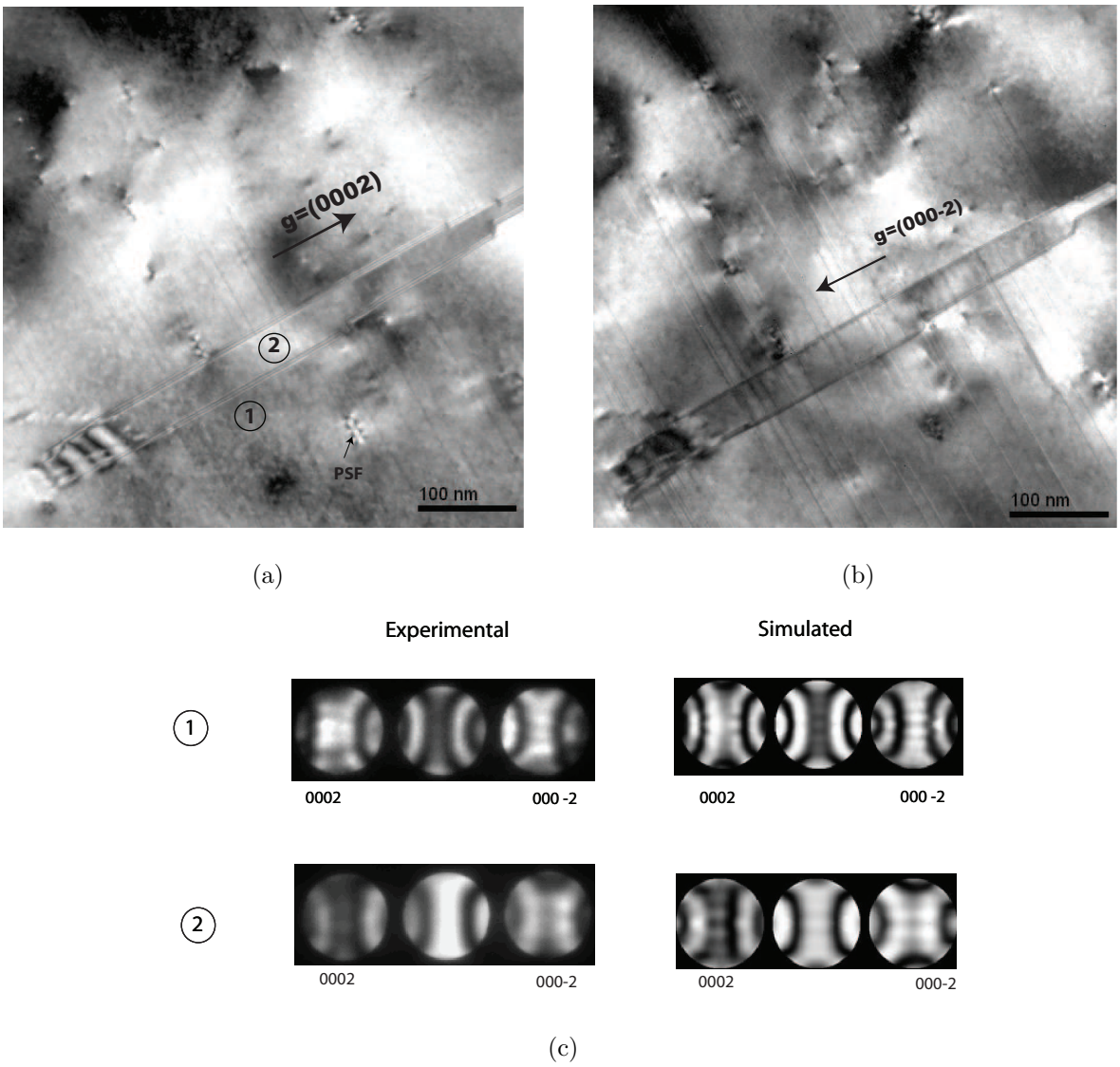

Figure 4.26: *Multiple dark beam images close to the* $[2\bar{1}\bar{1}0]$ *zone axis for the defect identification: a) under* $g = (0002)$ *diffraction condition, b) under* $g = (000\bar{2})$ *diffraction condition. The contrast difference of these two images is not large enough to conclude that this domain is an IDB. c) experimental and simulated CBED patterns taken at position* ***1*** *and* ***2*** *respectively (Figure 4.26(a)). The experimental patterns fit for thicknesses of 180 and 130 nm, respectivelly. Therefore, the defect is not an IDB, but a* $(10\bar{1}0)$ *stacking fault.*

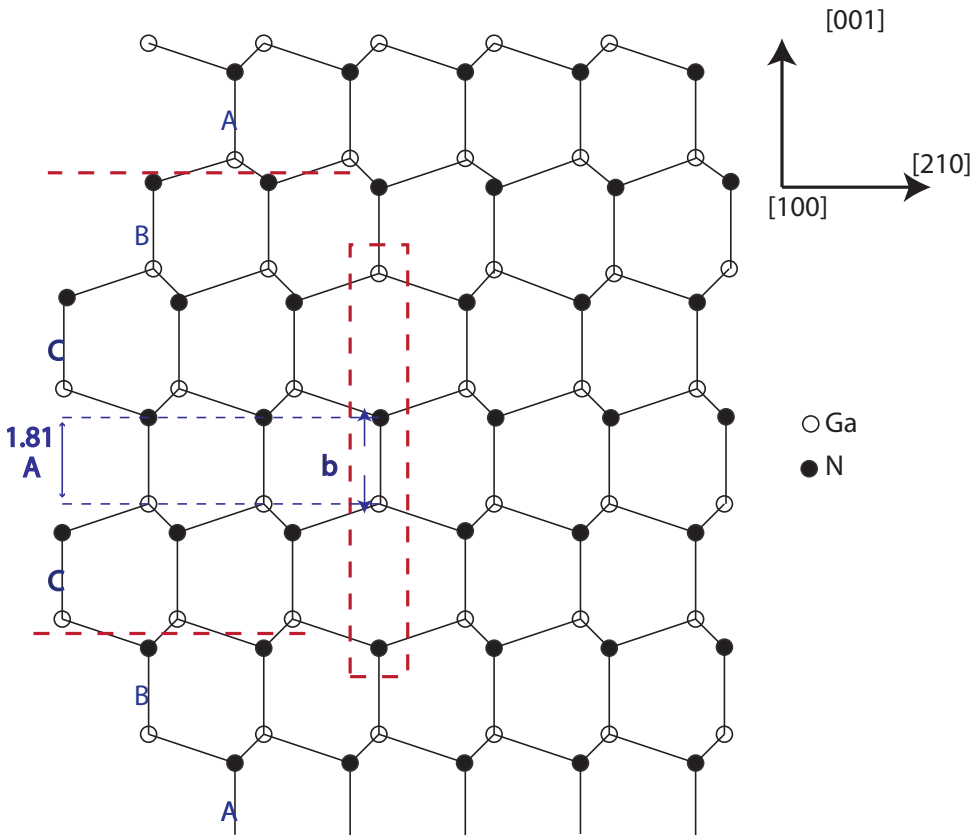

Figure 4.27: *The stacking fault boundary lies in the* $(10\bar{1}0)$*-plane and connects two stacking faults at the left of the boundary.* $b = 1.81\,\text{Å}$ *is the distance between the Ga and N in the boundary [138]. The boundary start when a SF occurs on the left and ends when the second SF occurs.*

which lie in $(10\bar{1}0)$-plane and those which are pointed with white and red arrows. White arrows show the position of BSFs which are connected by the $(10\bar{1}0)$-SFs. The red arrow points a prismatic stacking fault which is the boundary between the two $(10\bar{1}0)$-stacking faults.

4.5.4 Discussion

Stacking faults

High stacking fault density has been observed in both window and overgrown areas, $1 \times 10^6\,cm^{-1}$ and $4 \times 10^4\,cm^{-1}$ respectively. These stacking fault densities are larger than

those obtained by Haskell et al. [14] ($4 \times 10^5\, cm^{-1}$ and $3 \times 10^3\, cm^{-1}$) and slightly smaller than those observed by Chen and et al. [11] ($1 \times 10^6\, cm^{-1}$ and $3 \times 10^5\, cm^{-1}$). In this work, the high density of stacking faults observed in the window areas is attributed to the imperfections on the sapphire surface due to the long nitridation time. Reducing the nitridation time is expected decrease the stacking fault density. In the overgrown areas, the stacking faults results of the fast lateral growth rate and the accumulation of point defects or impurities.

Basal stacking faults

I_1 and I_2 -BSFs observed in the overgrown areas have displacement vectors $\vec{R} = \frac{1}{6} < 20\bar{2}3 >$ and $\vec{R} = \frac{1}{3} < 1\bar{1}00 >$ respectively. Shockley partial dislocations with Burgers vector $\vec{b} = \frac{1}{3} < 10\bar{1}0 >$ bounding the I_2-BSFs have been observed. The measured I_2 stacking fault energy, γ, is 50 erg/cm^2 in average (Table 4.3), which is slightly larger than the theoretically calculated estimated by Stampfl et al. and Wright et al. ($\approx$ 43.4 and 40 erg/cm^2) [126, 139]. It is closer to the experimental value determined by Zakharow et al. [33] where they measured a 5.5 nm partials' separation (Table 4.3).

Prismatic stacking faults

PSFs are also observed in a-GaN films with displacement vector $\vec{R} = \frac{1}{2}[\bar{1}\bar{1}01]$, they are located at the end of two I_1- BSFs. The mechanism of the prismatic stacking fault formation was described first by Drum [127]. Figure 4.28 shows the arrangement of the atoms along [0001] direction where the perfect stacking sequence is $ABABABAB\ldots$. When the first I_1-BSF is created, the stacking sequence changes to $ABABACACAC\ldots$ and is equivalent to $ABABCBCBC\ldots$. When the second stacking fault occurs, the stacking sequence changes to $ACACACBABA\ldots$. These PSFs result of the fact that the crystal grows faster laterally than vertically, and consequently when steps are created between two I_1-BSFs, the crystal grows with discontinuities forming the PSFs.

The Burgers vector of the stair rod dislocations (SRDs) is the difference between the displacement vector of both faults the PSF ($\vec{R} = \frac{1}{2}[1\bar{1}01]$) and the I_1-BSFs ($\vec{R} = \frac{1}{6} < 20\bar{2}3 >$) [33]. According to the I_1-BSFs displacement vector $\vec{R}$, the Burgers vector $\vec{b}$ of SRDs can have different configurations. The SRDs' configuration with the smaller energies

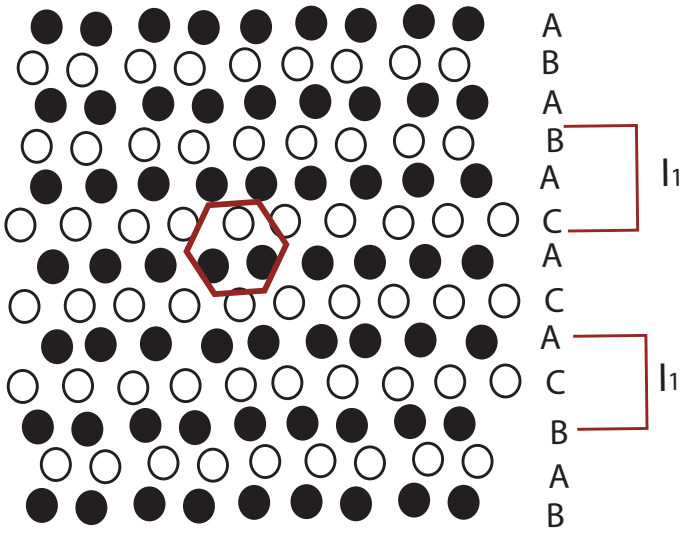

Figure 4.28: *Mechanism of the stacking sequence [127] for the formation of a prismatic stacking fault between two I_1-basal stacking faults, where the arrangement of the atoms gives hexagonal contrast (red hexagon).*

are given in the following reaction:

$$\frac{1}{2}[1\bar{1}01] \rightarrow \frac{1}{6}[2\bar{2}03] + \frac{1}{6}[1\bar{1}00] \qquad b^2 = \frac{a^2}{12} \tag{4.4}$$

$$\frac{1}{2}[1\bar{1}01] \rightarrow \frac{1}{6}[20\bar{2}3] + \frac{1}{6}[1\bar{3}20] \qquad b^2 = \frac{7a^2}{12} \tag{4.5}$$

$$\frac{1}{2}[1\bar{1}01] \rightarrow \frac{1}{6}[0\bar{2}33] + \frac{1}{6}[3\bar{1}\bar{2}0] \qquad b^2 = \frac{7a^2}{12} \tag{4.6}$$

The Burgers vector of Equation 4.4 has the smallest energy. Therefore, it is the most probable to be formed.

Closed domains

Closed domains are found in a-GaN films which consist in three different SFs. This domains are not often observed in a-GaN films. The stacking domain is formed by $(10\bar{1}0)$-SFs (stacking mismatch boundary) which are connected to BSFs folding the domain, and to a $(11\bar{2}0)$-PSF. $(10\bar{1}0)$-stacking faults have been also found by Zhou et al. [140]. They

can form closed domains with other stacking faults which involves stairs rods partial dislocations. This kind of stacking faults is found connected with basal stacking faults as is observed in Figure 4.25.

4.6 Optical properties in a-GaN films

Defects have a strong influence on the optical properties on either a- or c- GaN films. Previous studies of GaN layers have shown that threading dislocations are non-radiative recombination centers and that stacking faults shift the light emission. In this work, the optical properties were analyzed using SEM-cathodoluminescence (CL) and microphoto-luminescence (μ-PL) techniques.

4.6.1 Cathodoluminescence

The catholuminescence experiments of a-GaN show emissions that are not typical in c-GaN. A typical CL spectrum recorded at ~ 5°K and 10 keV incident electron energy features 4 main emission peaks at 3.48, 3.42, 3.3 and 3.21 eV (Figure 4.29). The emissions from 3.29 to 3.42 eV are not observed for c-plane GaN [141, 142]. The dominant emission line in the spectrum is at 3.42 eV, it has been attributed to I_1-BSFs [113, 143–145]. Since the BSF density is higher in a-GaN films than in c-GaN films, a stronger emission is obtained in a-GaN films. At 3.48 eV, the GaN NBE is observed in all GaN films [113, 141, 145]. The emissions observed at 3.29 eV and 3.21 eV are generally attributed to donor acceptor pairs (DAP) and recombination vacancy oxygen complexes [145, 146] respectively. Therefore, the emissions at 3.42, 3.29 and 3.21eV are associated to structural defects.

A secondary electron (SE) image of a cross sectional a-GaN film grown by ELO-HVPE without buffer layer is shown in Figure 4.30, where the window (*1*), the overgrown (*2*) and the void (*3*) areas are easily identified. The voids are the result of the asymmetric growth rates of the N and Ga faces as described in Section 4.4.

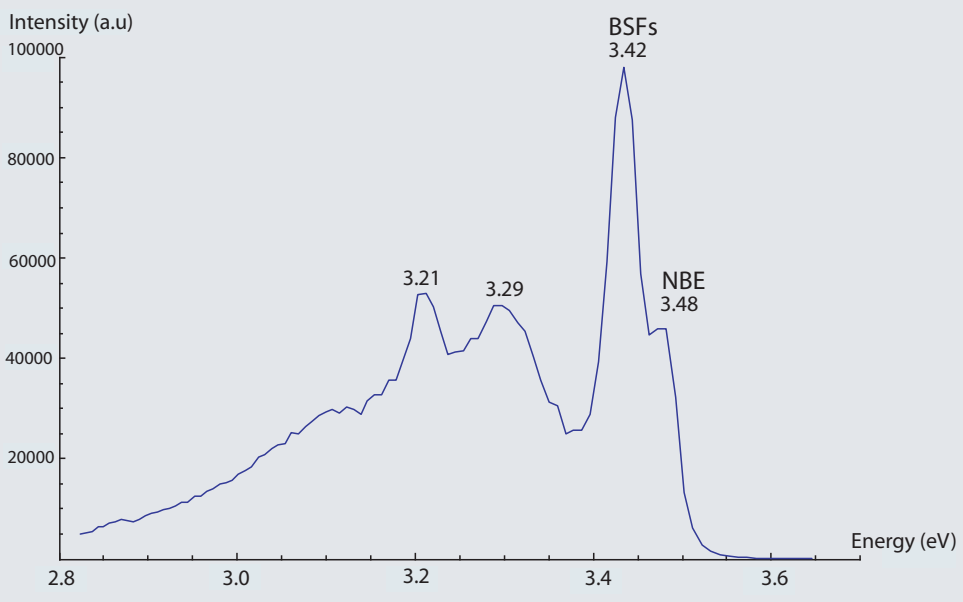

Figure 4.29: *a-plane GaN CL spectrum at 5^{o}K. The NBE peak at 3.48 eV and the dominating peak at 3.42 eV are shown. The emission at 3.42 eV is associated with BSFs.*

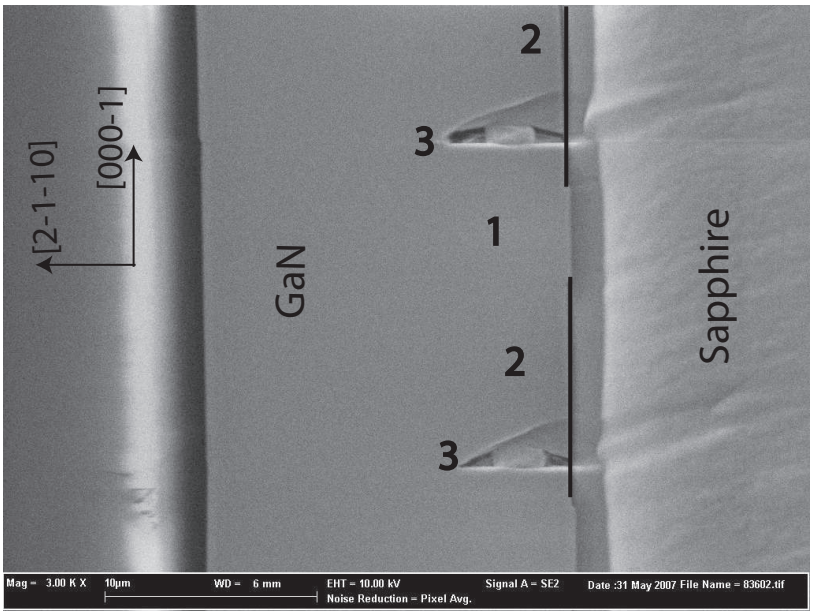

Figure 4.30: *Secondary electrons image of a full coalesced a-GaN film, prepared for cross sectional TEM observations. The three different areas can be observed: 1) windows, 2) overgrown and 3) voids.*

A CL image taken at 3.48 eV (NBE emission) is shown in Figure 4.31(a). This emission in the GaN layer is not uniform. It is weaker in the window (1) and the void (3) areas than in the overgrown areas (2). Since threading dislocations are non-radiative recombination centers and their density in the window areas is high ($\approx 10^{10}\, cm^{-2}$), the CL intensity in this area is low. In the overgrown areas, the emission increases due to the implementation of the ELO method that reduces the dislocation density. In this image, one can also observe the growth fronts, where the lateral rate was faster than the vertical one, producing a triangular shape until the coalescence of the fronts. The dark lines observed in the overgrown areas are related to the stacking faults, which do not emit light at 3.48 eV.

A CL image at 3.42 eV is shown in Figure 4.31(b). The CL emission is more homogeneous in the window areas (1) than in the overgrown areas (2), where the I_1-BSF density is higher in the window areas than in the overgrown areas and therefore the I_1-BSFs are shifting 0.06 eV from the NBE emission (3-48 eV). This is no surprise since BSFs can be considered as a thin zinc-blende quantum well embedded in the wurtzite matrix [126]. In the overgrown areas, black areas (non emission) are observed, which are free of I_1-BSFs. Around the void areas, there are no emission at 3.42 eV and at 3.48 eV (Figure 4.31(a)) and therefore, different defects affect these areas.

CL emission at 3.29 eV is observed around the voids and locally in the window areas (Figure 4.31(c)). This emission is usually attributed to structural defects, surface defects and impurities [11, 143, 146]. This emission in the window areas of a-plane GaN could be correlated to PSF (at 3.33 eV [113, 144]), partials dislocations (at 3.30 eV [113]) and stairs-rod dislocations (at 3.29 eV [144, 145]). At 3.21 eV, the emission is located around the voids (Figure 4.31(d)). This emission has been associated to recombination vacancy oxygen complexes [145, 146].

4.6.2 Micro-photoluminescence

The structural characterization and cathodoluminescence experiments of a-GaN layers are compared with the μ-PL experiments. μ-PL observations were carried out in coalesced

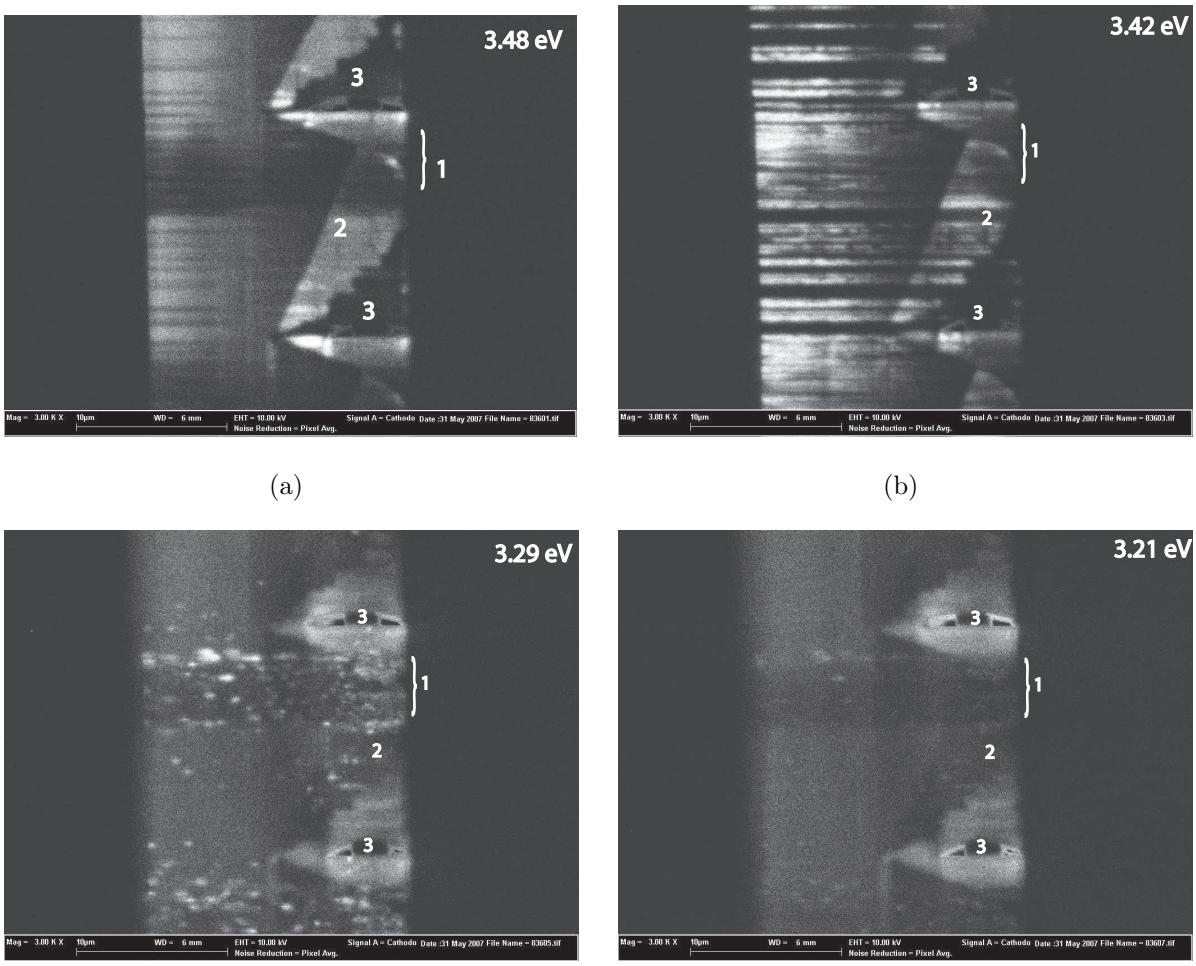

(a) (b)

(c) (d)

Figure 4.31: *Cross sectional SEM-cathodoluminescence images at* $\sim 5°K$ *and 10 kV: a) at 3.48 eV (NBE), b) at 3.42 eV (BSFs), c) at 3.29 (partial dislocations and PSF) and c) at 3.21 (vacancy oxygen complexes).*

a-GaN samples in collaboration with LASPE-IQEP.

Low temperature ($T = 4^oK$) μ-PL spectra are shown in Figure 4.32. Optical quality between the window (red curve) and the overgrown (black curve) areas are plotted.

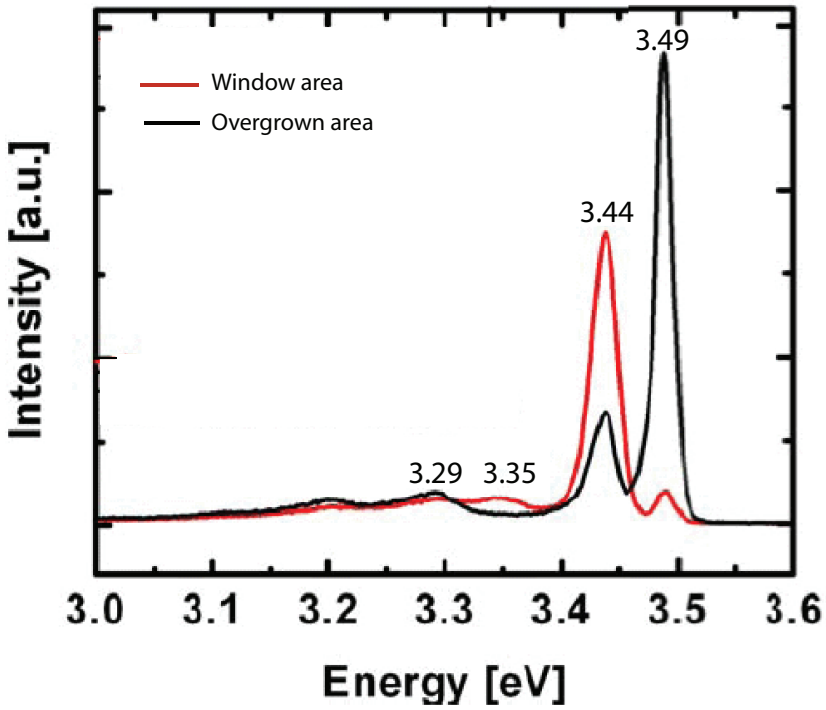

Figure 4.32: *Low temperature (T=4K) μ-PL spectra of HVPE-ELO GaN in both window (red curve) and overgrown (black curve) areas.*

Window and overgrown areas have emission peaks at 3.44 eV and 3.49 eV, respectively. The near band emission (NBE), at 3.49 eV, has a larger intensity in the overgrown areas than in the window areas because according to TEM observations the threading dislocation and stacking fault densities are reduced in the overgrown areas. In CL spectrum, the NBE is located at 3.48 eV and in μ-PL spectra at 3.49 eV. This small shift is because in CL the NBE is found as a shoulder of the 3.42 eV that shift the energy of the NBE. The intensity of the peak at 3.44 eV is higher in the window areas than in the overgrown areas, because the stacking fault density is reduced in the overgrown area from 1×10^6 cm^{-1} to 4×10^4 cm^{-1}.

In the window areas, there is a broad peak of low intensity near 3.35 eV, which is normally

associated with structural defects. These defects could be either I_2-BSFs or PSFs [147]. In CL experiments, this peak is also found at 3.36 eV with low intensity and as a shoulder of 3.29 eV emission.

In the overgrown areas (above the mask), two peaks of low intensity at 3.20 and 3.29 eV are observed. These emissions are related to structural defects such as partial dislocations, PSFs and vacancy oxygen complexes. In μ-PL spectra these peaks has low intensity than in CL spectrum because the μ-PL spectra were performed in a small area of the window and overgrown areas and CL experiments were performed in the bulk material. For this reason, stronger intensity is observed in the CL spectrum.

4.6.3 Discussion

Cathodoluminescence

The CL-spectrum of a-GaN gives 4 different emissions and three of them are not observed in c-GaN layers. The NBE is located at 3.48 eV and the other emissions are associated with structural defects. The dominant emission is 3.42 eV which is related with BSFs as was confirmed by Liu et al. [113]. According to the literature, the other two emissions at 3.29 and 3.21 eV are also attributed to structural defects. At 3.29 eV, the emission is attributed to PSFs, partial dislocations and stair rod dislocations [113, 144, 145] and at 3.21 eV to vacancy oxygen complexes [145, 146]. Our experiments confirm that defects affect the optical properties and the main defects are TDs and BSFs.

The image in Figure 4.33(a) combines two CL images, one (blue) taken at 3.48 eV and the other (green) at 3.42 eV. One observes that the BSF emission at 3.42 eV is complementary to that at 3.48 eV. This means that, the regions which are emitting at 3.48 eV, are not emitting at 3.42 eV. This happens because these regions are free of BSFs. According to the analysis of defects of the a-GaN samples, the defects emitting at 3.42 eV are I_1-BSFs that cross the film from the interface towards the surface, these areas correspond to 3.42 eV.

Figure 4.33(b) shows an image that combines two CL images, one at 3.42 eV (green) and

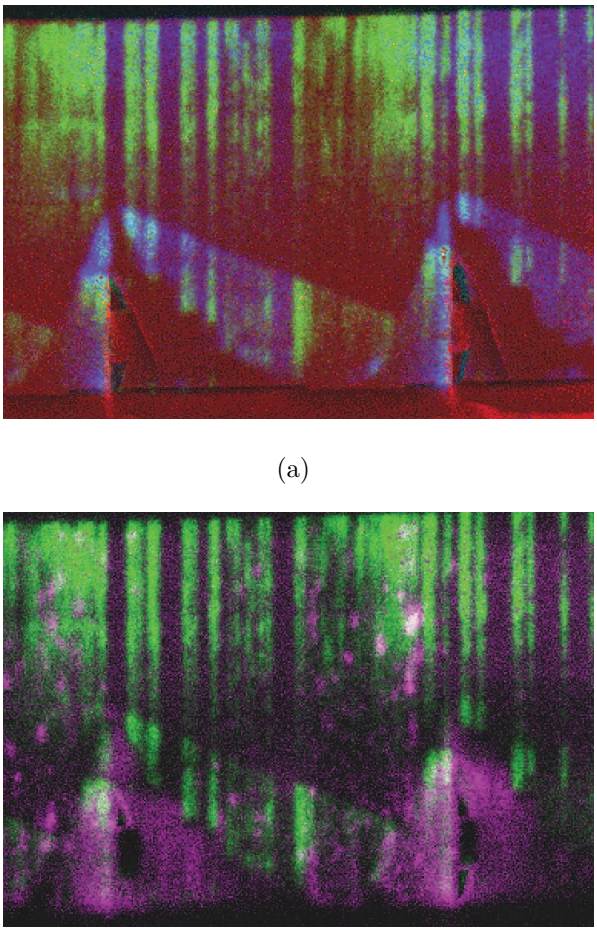

(a)

(b)

Figure 4.33: *False color CL images: a) at 3.48 (blue) and 3.42 (green) eV, they are complementary to each other and b) at 3.42 and 3.29 (purple) eV, they are associated with structural defects.*

the other at 4.29 eV (purple). Both emissions are associated with structural defects. The green emission is characteristic of I_1-BSFs and the purple emission of PSFs, partial dislocations and impurities. Purple emission is located mainly in the highly faulted window areas and around the void where is characteristic of impurities, in which the figure does not show emission from the stacking faults. In Figure 4.33(b), one can observe that the structural defects in a-GaN have an effect on the optical properties giving emission at different energies that the NBE.

Furthermore, we have observed light emissions around the voids at 3.29 eV and 3.21

eV which are also associated to Si and O impurities and oxygen complexes. A possible explanation is as follow: GaN grows in two directions, c- direction Ga-polarity where there is only one dangling bond, and $-c$-direction N-polarity with three dangling bonds (Figure 4.34). The Si or O impurities are incorporated to the dangling bonds in c-direction reducing the lateral rate until the growth stops, creating a void. Consequently, saturation of the Ga-polar direction occurs much earlier than in N-polar direction. The formation of voids is the result of the incorporation of impurities along the SiO_2 mask.

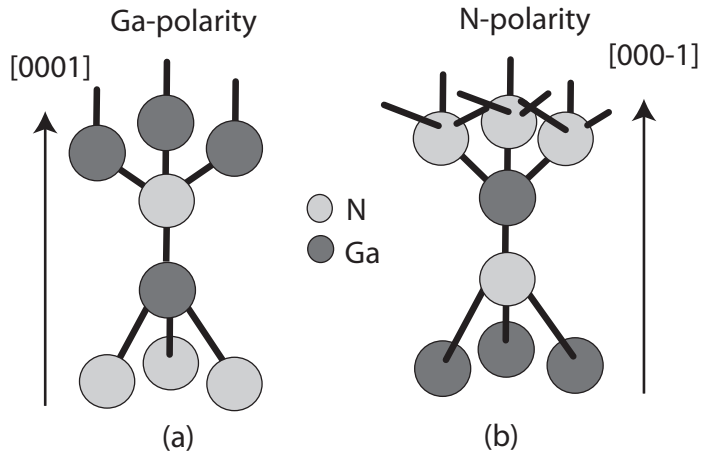

Figure 4.34: *Representation of GaN bond for Ga- and N- polarities. Ga-polarity has one dangling bond and N-polarity has three dangling bonds.*

μ-Photoluminescence

μ PL-spectra shows also 4 emissions where the dominant are at 3.44 eV for the window and at 3.49 eV for the overgrown areas respectively. In the window areas, the high emission at 3.44 eV is due to the presence of BSFs where the density is larger than that obtained in the overgrown areas. In the overgrown areas the dominant emission is at 3.49 eV (NBE) since the stacking fault density is reduced in these areas, as measured by TEM (Section 4.5.1).

We can conclude that:

1. ELO technique improves the quality of the a-GaN, because in the overgrown areas the intensity of the NBE is much more intensive than in the window areas. Therefore, a reduction of defect density was obtained.

2. The stacking fault density gives emission at different energy that the NBE. This emission is reduced in the overgrown areas demostrating a large improvement in the quality of the a-GaN layer.

3. Structural defects give emission at differents energies (3.29 and 3.35 eV). These defects are PSFs and partial dislocations in the window areas, and the formation of vacancy oxygen complexes in the overgrown areas.

4. The μ.PL experiments are in agreement with our CL results, where the optical quality of the overgrown areas is improved with respect to the window areas.

We come to the conclusion that, the main defects which affect the optical properties are the threading dislocations and the stacking faults.

4.7 Analysis of defects of GaN films with and without buffer layer.

The two types of GaN samples ($S1$ and $S2$) were characterized in order to compare their structural quality. In the analysis of defects of both types of samples, it has been found that:

1. In the window areas, the threading dislocation and stacking fault densities are similar in both samples, $\approx 1 \times 10^{10}\, cm^{-2}$ and $1 \times 10^{6}\, cm^{-1}$ respectively. These densities do not vary because in the window areas in both samples the GaN is deposited onto the substrate. These threading dislocations have screw or mixed character and the stacking faults are basal of the I_1 type.

2. In the overgrown areas, the reduction of the dislocation density depends on the thickness of the film, the thicker the film the smaller the densities. $S2$ shows a slightly smaller dislocation density than $S1$ close to the top surface. Dislocations lying parallel to [0001] direction near the SiO_2 mask in $S1$, are not observed in $S2$. These dislocations could result of the residual strain coming from the window areas in $S1$ (the mask

is deposited directly on the sapphire). The voids in the $S2$ samples are smaller than those in $S1$ samples and a reduced dislocation density is observed around the small void. The stacking faults density is slightly smaller in $S2$ than in $S1$ ($4 \times 10^4\, cm^{-1}$ and $6 \times 10^4\, cm^{-1}$) as a consequence of the buffer layer.

3. Low PSFs density is observed in the overgrown areas in both types of samples ($S1$ and $S2$).

4. Stacking mismatch boundaries are not often observed in GaN samples. The only one observed in this work was in sample $S2$.

We can conclude that the $S2$ samples with buffer layer present slightly smaller defect density than the $S1$ samples. The $S2$ optical properties are improved, since the stacking fault density is slightly reduced in the $S2$ samples. Stacking faults areas give emission at different energy of emission that the NBE emission.

4.8 Defect mechanism

Defects are created during the HVPE-ELO growth process, we can divided in two steps:

1. During the deposition of the nucleation layer and the growth of the buffer layer.

2. During the growth of the GaN film using ELO.

4.8.1 Buffer layer

The defects created during the deposition of the buffer layer can be explained with the following growth model (Figure 4.35). It consists of the following steps:

Nitridation. Nitridation is applied to the sapphire in order to modify the surface energy and to enhance the nucleation layer. In this work we have shown that the sapphire surface has imperfections that we attributed to the long nitridation time (Figure 4.35a).

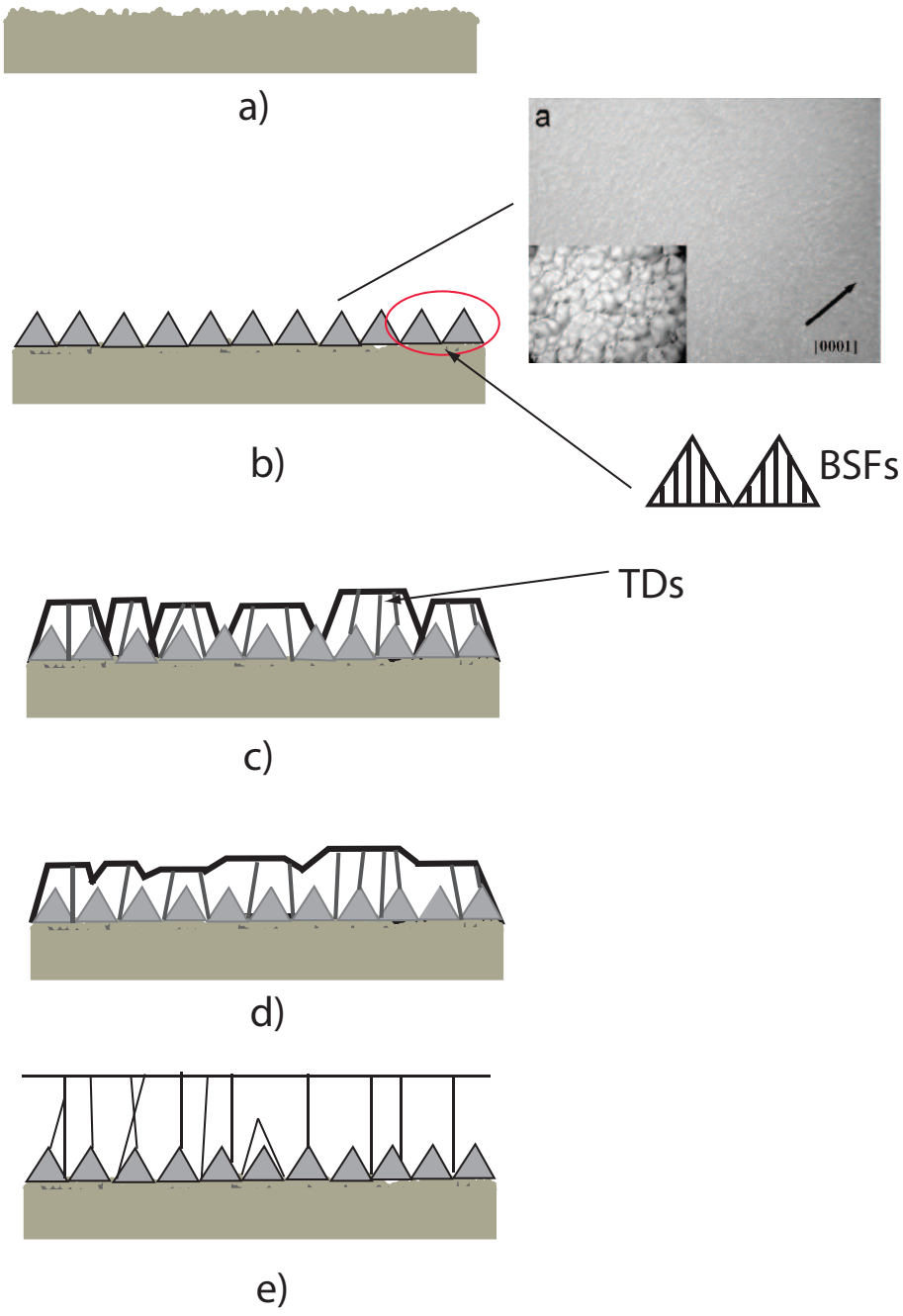

Figure 4.35: *Schematic growth sequence of the defects generation during the buffer layer growth: (a) nitridation, (b) nucleation of the islands, (c) growth of islands and generation of threading dislocations, (d) coalescence of the islands and (e) buffer layer with high dislocation density.*

Nucleation layer. GaN nucleates on the substrate as islands. The nucleation layer serves as the crystallographic and morphological template for the subsequent GaN deposition. In this work, it was not deposited at low temperature as is usually done in c-GaN by MOCVD, resulting in a lower quality nucleation layer. The deposition temperature was ranging 1075 ^oC to 1090 ^oC and at 400 mbar. The GaN nucleation layer is rough and consists of large non-coalesced islands as is shown in the image in Figure 4.35(b) [91]. At this pressure, the GaN growth is 3D (islands growth).

As a consequence of the imperfections on the sapphire surface and oxygen impurities, stacking faults are formed at the GaN/sapphire interface. Stacking faults are perpendicular to the interface crossing the layer to the top surface of the film (Figure 4.35(b)).

Island growth. After the deposition of the nucleation layer, the pressure is reduced to 100 mbar and temperature is kept constant. At this pressure the lateral growth is faster that the vertical one. The islands start to coalesce and form threading dislocations (Figure 4.35(c)), of screw or mixed characters. The stacking faults created at the interface during the nucleation layer deposition follow the GaN layer growth.

Coalescence of the islands. The islands continue growing until the full coalescence (Figure 4.35(d)). The coalesced layer does not have a flat surface and the threading dislocation density increases.

Buffer layer. After the coalescence of the islands, the film growth continues until the flattening of the surface. This ends the formation of the buffer layer. The buffer layer has high dislocation and stacking fault densities. The dislocation density increases when the layer thickness increases ($t > t_{critical}$). The critical thickness is less than one monolayer. Misfit dislocations accommodate the large mismatch of the system, originating the formation of more TDs.

This growth model describes the a-GaN growth buffer layer by HPVE using two different pressures (400 and 100 mbar) and high temperature. This model is similar to that describing the growth of c-GaN buffer layers. The main difference is that in c-

GaN the nucleation layer and buffer layer are deposited at low temperature (525 to 600 C^o) by MOCVD [148, 149]. In c-GaN grown by MOCVD, the dislocation density is decreased when using short nitridation time and it is increased when using long nitridation times [148]. A difference between the a-GaN and the c-GaN model is the position of the stacking faults. In c-GaN, BSFs are parallel to the GaN/sapphire interface and not perpendicular to it as it is in a-GaN (Figure 4.35(b)). For this reason, the BSFs in c-GaN do not have effect on the optical properties of the material. In a-GaN films, the nucleation layer and buffer layer are grown by MOCVD [47, 112, 145]. a-GaN films grown directly on the sapphire using HVPE have been only reported in few works [14, 145]. There is consequently not many works to compare with this work.

4.8.2 Growth of the GaN film

The second part of the growth model consists of the growth of the a-GaN film using ELO technique. In order to explain the defects in the overgrown areas, two different CL-images (3.48 and 3.42 eV) are used (Figure 4.36).

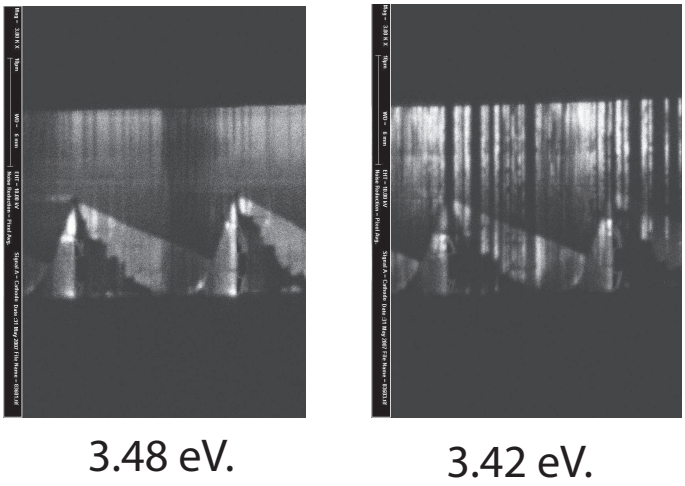

Figure 4.36: *CL-images at 3.48 and 3.42 eV.*

In these images, one can observe the growth fronts until they coalesce forming a triangular feature, where the [0001] direction can be distinguished from the $[000\overline{1}]$ due to the incorporation of impurities, obtaining a flat face for $-c$-direction and a diagonal face for

c-direction. Figure 4.37(a) shows a scheme of the cross section along the $[10\bar{1}0]$ direction. In this scheme, one can observe how is the growth in the window and the overgrown areas until the coalescence. The threading dislocations in the buffer layer are blocked by the SiO_2 mask and only in the window areas the dislocations and stacking faults are propagated vertically. In the lateral area (above the SiO_2 mask), new dislocations are formed. These dislocations have their origin in:

- The difference of thermal expansion coefficients between SiO_2 mask and GaN combined with the residual strain. This occurs during the cooling of the growth process. These effects contribute to the formation of defects in the GaN.
- The coalescence of the two meeting fronts.

In the overgrown areas, stacking faults are also found and are formed by:

- Imperfections in the SiO_2 mask. Figure 4.37(c) shows a micrograph under $\vec{g} = (01\bar{1}0)$ with stacking faults created at the GaN/mask interface. Figure 4.37(d) shows a HRTEM micrograph in the $[10\bar{1}0]$ zone axis above the SiO_2 mask. The SiO_2 mask does not have a flat surface and therefore it can contribute to the formation of stacking faults (since they contribute to the relaxation of the strain during the lateral growth).
- Impurities above the SiO_2 mask. The incorporation of oxygen in the GaN structure during the lateral growth can contribute to the formation of stacking faults (Figure 4.37(c)). Figure 4.36 at 3.42 eV shows BSFs created at the GaN/sapphire interface, giving emission along the film. The black area around the voids is the area of the GaN with larger impurities' density, and it does not emit light at this energy.

After the coalescence, it is necessary to grow the GaN layer for longer time in order to obtain a fully coalesced and a flat layer (Figure 4.37(b)). In the window areas, the dislocations go straight towards the surface and the dislocation density is high. The dislocation density is inhomogenous along the film and it is much higher in the window areas than in the overgrown areas as have been observed in published works.

Figure 4.38 shows a scheme of the cross section along $[10\bar{1}0]$ direction of the c-GaN [150, 151]. Comparing a-GaN and c-GaN schemes, we observed that the dislocations in the

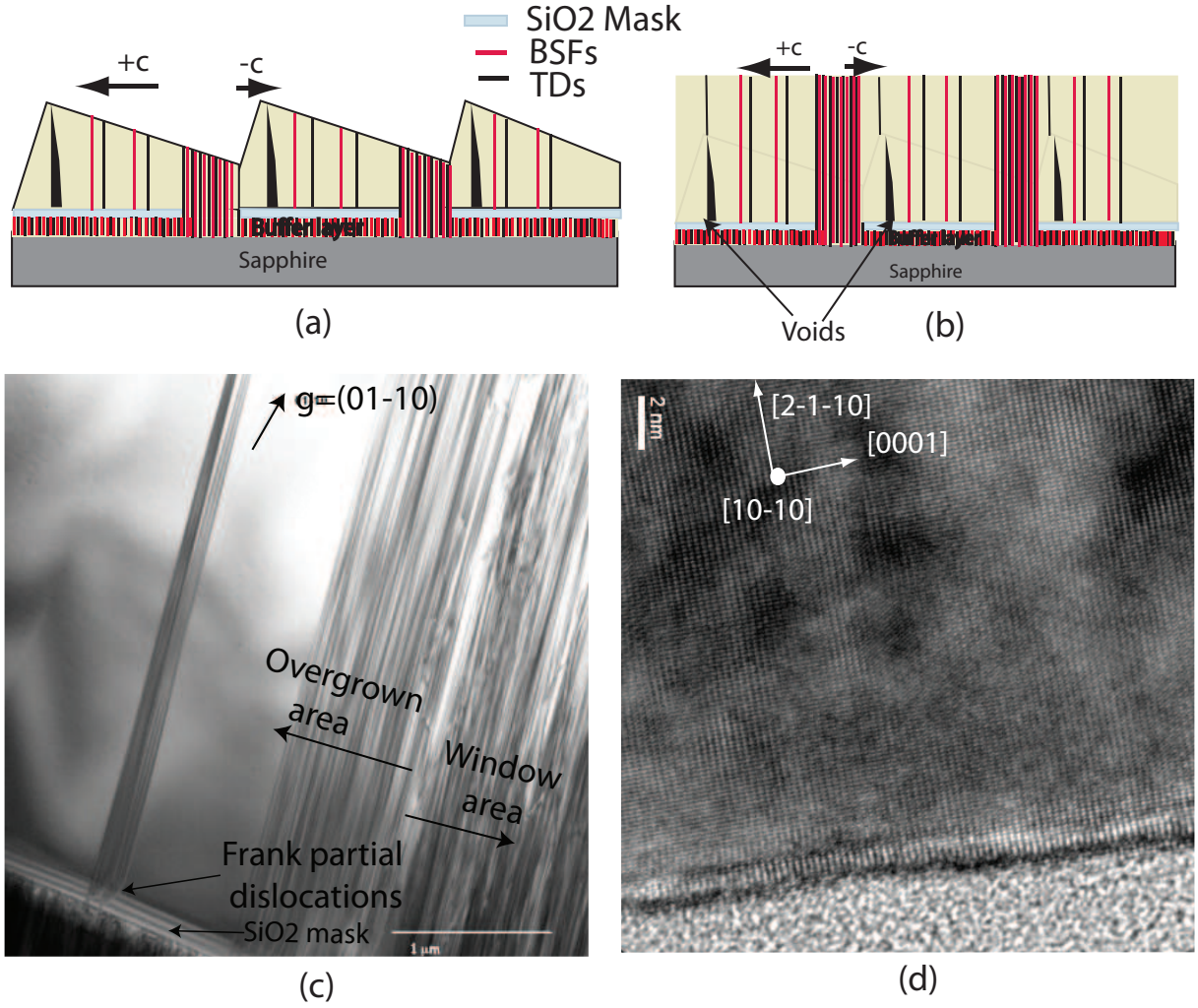

Figure 4.37: *Scheme of the* $[10\bar{1}0]$ *cross section of a-GaN when the ELO stripes coalesces.*

window areas in c-GaN propagate vertically and then bend 90^o to the lateral areas. This does not occur in a-GaN. Bending dislocation phenomenon reduces the dislocation density in the window areas creating a homogeneous dislocation density along the layer. c-GaN takes advantage of the phenomenon to improve the quality of the layer.

In c-GaN, the bending dislocations are formed due to the variation of the lateral growth rate. Firstly, GaN is grown (dashed lines in Figure 4.38) having its vertical growth rate faster than its lateral growth rate, resulting in a triangular $[10\bar{1}0]$-cross section. Further growth conditions favor the lateral growth until the full coalescence. The behavior of the

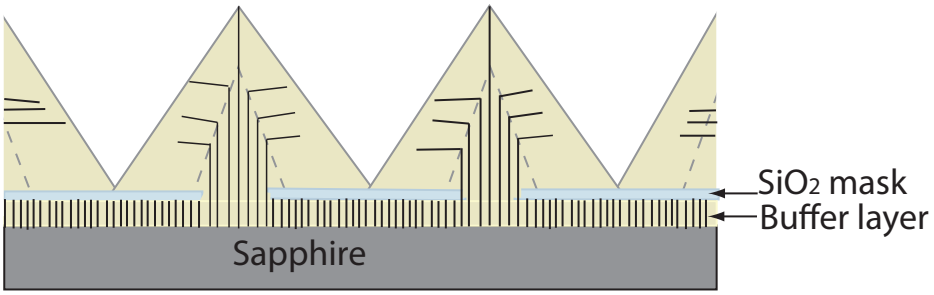

Figure 4.38: *Scheme of the* $[10\bar{1}0]$ *cross section of a two step ELO growth. The dislocations in the window area bend to the lateral area. dashed line is the first step of ELO growth.*

dislocations is illustrated in Figure 4.38.

In a-GaN films, bending dislocation does not occur and it has high stacking fault density which affect the optical properties.

4.9 Microstructural characterization of a-GaN/$Al_{1-x}Ga_xN$ single quantum well.

Quantum wells in non-polar materials such as a-$(11\bar{2}0)$ plane GaN do not suffer from the quantum confined Stark effect that reduces the emission efficiency in the polar structure (c-plane GaN) [152]. In order to confirm the absence of quantum confined Stark effect, six $Al_{1-x}Ga_xN$/GaN/$Al_{1-x}Ga_xN$ single quantum well (SQW) samples have been prepared by MBE in collaboration with LASPE-IQEP. These samples correspond to a particular *Al* content and SQW thickness. They were characterized by SEM to probe the surface quality and by TEM to analyze the MBE layers structure.

The structure of these specimens is schematically shown in Figure 4.39. It consists of an a-GaN template grown by HVPE-ELO (specimen characterized in the previous sections), and 4 supplementary layers grown by MBE. The first MBE layer, which is a-GaN, has been grown in order to deposit the SQW group on a material of better structural quality.

The last three layers of the SQW group consist of a single GaN quantum well inserted between two $Al_{1-x}Ga_xN$ layers.

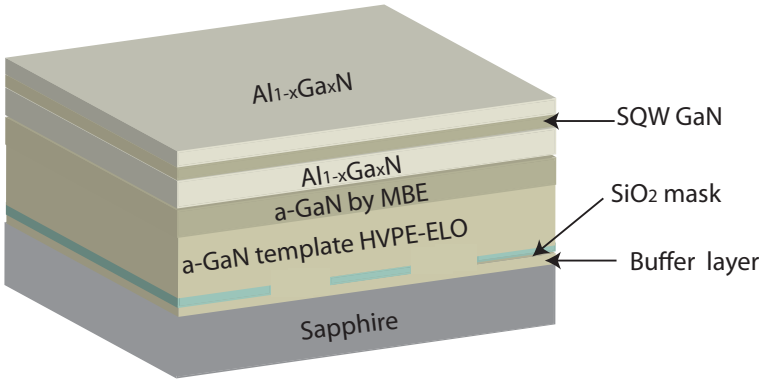

Figure 4.39: *Scheme of the structure of the $Al_{1-x}Ga_xN/GaN/Al_{1-x}Ga_xN$ quantum well specimen grown on a-GaN template HVPE-ELO by MBE.*

The six samples can be divided in three different groups according to the aluminum content (atom %). Each group is formed of two samples of different GaN-SQW thickness. The thickness of the MBE-layers was measured by HRTEM and DF-TEM techniques, and the aluminum content (Al%) was measured by EDS in scanning transmission electron microscopy (STEM). Table 4.4 resumes the main characteristics of these samples.

Layers/Sample	S1	S2	S3	S4	S5	S 6
$Al_{1-x}Ga_xN$ $(\pm 3nm)$	160	168	145	155	138	140
GaN $(\pm 0.3nm)$	1.7	3.7	1.7	3.75	1.6	3.65
$Al_{1-x}Ga_xN$ $(\pm 2nm)$	42	40	40	39	36	38
Atomic % of Al (± 0.03)	0.23	0.225	0.135	0.133	0.08	0.075

Table 4.4: *Thicknesses and Al content of $a-GaN/Al_{1-x}Ga_xN$ single quantum well samples.*

4.9.1 V-defects on the sample surface.

The surface of the SQW samples was imaged by SEM. The six SQW samples have a rough surface due to the formation of pits at the surface connected to threading dislocations. Pits

or v-defects degrade the performance of devices, in particular light emission [22] and affect the optical properties of the quantum well [153]. The formation of the pits was attributed mainly to dislocations, although there was no convincing evidence [154, 155].

The pits density has been measured in the six SQW-GaN samples by the mean of SEM micrographs (Figure 4.40). They all present a high pit density at their surface, up to $\approx 1 \times 10^{12}\ cm^{-2}$. A SEM micrograph of sample S4 shows that the pits are distributed all over the surface with a higher density in the window areas (Figure 4.40(a), position 2). There are two different sizes of pits, shown inside the white circles indicated by S for small pits and by L for large pits (Figure 4.40(a)). A higher magnification SEM micrograph from the S4 surface is shown in Figure 4.40(b), where we can observe the two pit sizes (S and L). The large pits affect more the surface quality than the small ones.

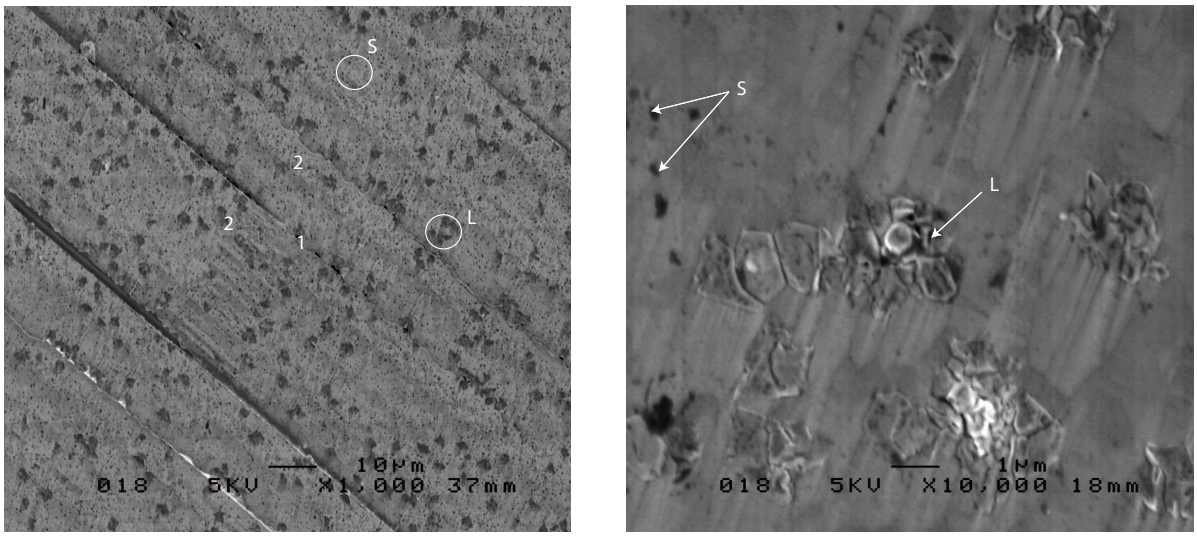

(a) (b)

Figure 4.40: *SEM micrographs of the sample surface (S4). a) distribution of the pits:* ***1*** *coalesced area and* ***2*** *window areas and b) the size of the pits vary: large (L) and small (s).*

To understand the relation between the pits and treading dislocations, cross-sectional TEM samples along the $[10\bar{1}0]$ direction (perpendicular to the SiO_2 mask) and the [0001] direction (parallel to the SiO_2 mask) have been prepared. DF micrograph of a pit under $\vec{g} = (1\bar{2}10)$ diffraction condition close to the $[10\bar{1}0]$ zone axis is shown in Figure 4.41(a).

The large pit ($\approx 700\,nm$ depth) starts in the MBE-GaN layer and presents, at its bottom, a group of straight dislocations coming from the template. The $\vec{g}.\vec{b} = 0$ invisibility criterion shows that these dislocations have screw character with $\vec{b} = \frac{1}{3} < 11\bar{2}0 >$.

The small pits are commonly observed at locations where groups of dislocations intersect the surface as is demonstrated by the DF micrograph under $\vec{g} = (1\bar{2}10)$ diffraction condition, taken close to the [0001] zone axes is shown in Figure 4.41(b). The pit ($\approx 250\,nm$ depth) is created at the intersection of several dislocation groups near the surface. These dislocations have different characters and can be divided in 3 groups (marked by 1, 2 and 3 in Figure 4.41(b)):

1. Threading dislocations with screw character and Burgers vector $\vec{b} = \frac{1}{3} < 11\bar{2}0 >$.
2. Dislocations forming a subgrain boundary or a low angle grain boundary (coalesced area). The identification of the grain boundary was not possible due to the orientation of the sample.
3. Groups of dislocations that cross diagonally the layer.

Dislocations in group 4 have the character of dislocations in group 3, but end at a nearby neighbored pit (micrograph 4.41(b)).

4.9.2 $Al_{1-x}Ga_xN$/GaN-SQW/$Al_{1-x}Ga_xN$/GaN MBE interfaces

We found that, new defects can be formed at the interfaces of the MBE layers. A scheme of the structure of the MBE-layers is given in Figure 4.42 where the two most important interfaces, ***1*** for $Al_{1-x}Ga_xN$/GaN and as ***2*** for GaN-SQW/$Al_{1-x}Ga_xN$, are indicated.

A HRTEM micrograph taken along the $[10\bar{1}0]$ zone axis of $Al_{1-x}Ga_xN$/GaN interface (1) is shown in Figure 4.43. A smooth interface and a perfect match between the planes of MBE-GaN and $Al_{1-x}Ga_xN$ layers is observed due to the small difference between their lattice parameters (Figure 4.43(a)). When the *Al* content is low (AlN: a= 0.3112 nm and c=0.4982nm [16] and GaN: a= 0.319 nm and c=0.518nm) the lattice mismatch is very small (i.e. 5 % of Al, the mismatch is 0.12%).

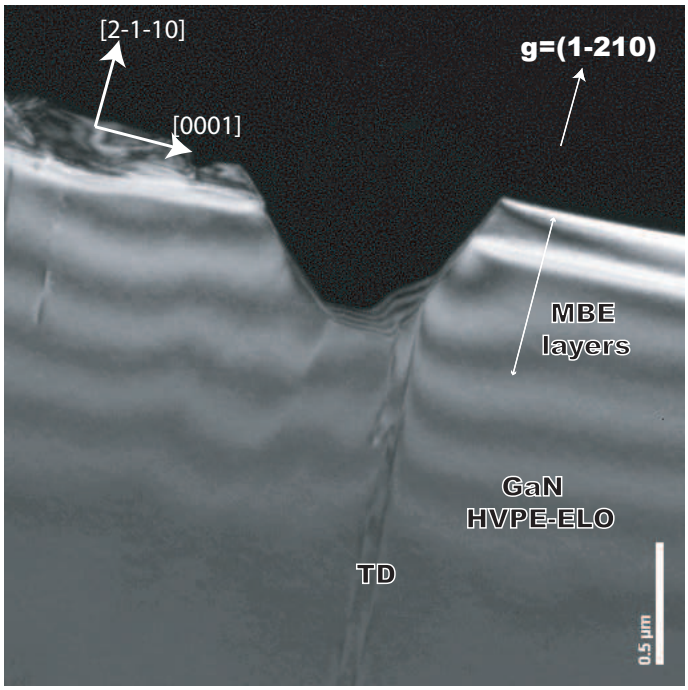

(a)

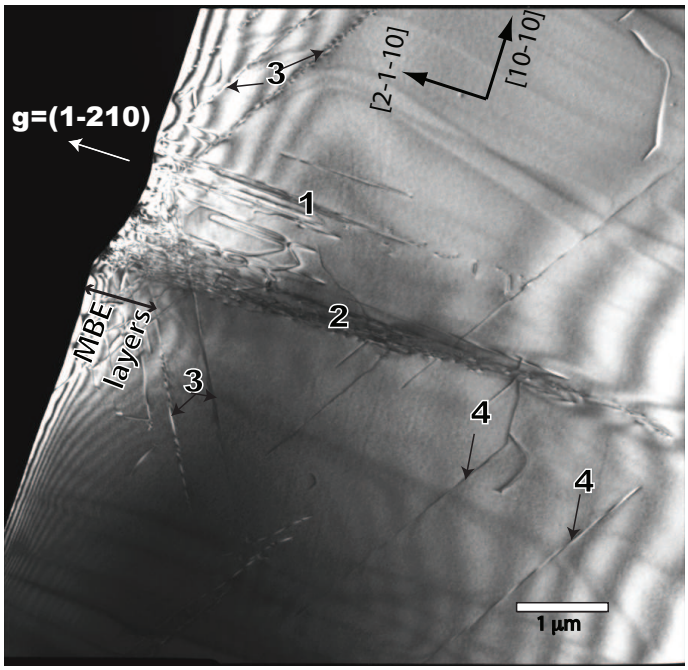

(b)

Figure 4.41: *Cross-sectional TEM micrographs under* $\vec{g} = (1\bar{2}10)$ *diffraction condition close to the* $[10\bar{1}0]$ *(*$\perp$ *SiO_2 mask) and [0001] (*$\parallel$ *SiO_2 mask) zone axis: a) a pit with threading dislocations of screw character at the bottom and b) formation of a pit by the intersection of several groups of dislocations.*

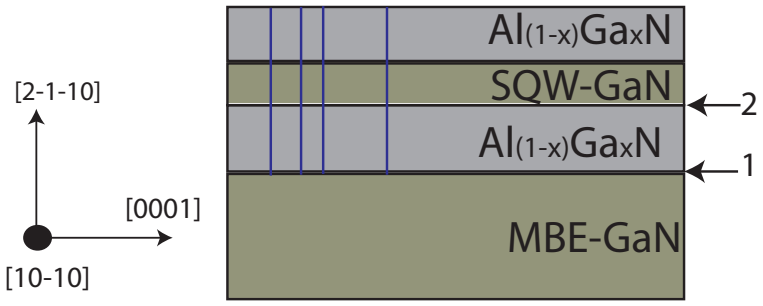

Figure 4.42: *Scheme of the structure of the MBE-layers: Projection along the* $[10\bar{1}0]$ *zone axis; new defects shown as blue lines originated at the* $Al_{1-x}Ga_xN/GaN$ *interface (1) crossing the layers towards the surface.*

At the $Al_{1-x}Ga_xN$/MBE-GaN interface, new defects are formed, and they are identified as I_1-BSFs (Figure 4.43(b)). I_1-BSFs are observed as lines starting at the $Al_{1-x}Ga_xN$/MBE-GaN interface and ending at the surface. Due to the defects, the MBE-layers can be divided in two areas: perfect MBE-GaN (*1*) and faulted $Al_{1-x}Ga_xN$/SQW-GaN/$Al_{1-x}Ga_xN$ layers (*2*). The Fourier transforms (FT) from the two areas *1* and *2* of Figure 4.43(b) are shown in Figure 4.43(c). In the FT of area *2*, streaking diffracted spots along [0001] direction are observed which are not observed in the FT of the area *1*. These typical streaks are characteristic of a crystal containing stacking faults in the basal plane. A high basal stacking fault density was measured in the MBE layer. This density ranges from 1×10^5 to 1×10^6 cm^{-1} and it is close to the BSF density measured in the GaN template.

In order to observe these BSFs, a plan-view sample was prepared. A plan-view DF micrograph taken under $\vec{g} = (1\bar{2}10)$ diffraction condition shows a high density of prismatic stacking faults ending at the sample surface (Figure 4.44(a)). Some of them are aligned in groups (G) and other are isolated (white arrows). PSFs are located at the end of two I_1-BSFs as is shown in Figure 4.44(b) where the two stacking faults can be observed (black arrows). PSF density in the MBE layers is much larger than the one in GaN templates. PSFs are created due to the new BSFs in the MBE layers and the BSFs coming from the template.

A single GaN quantum well is observed between the two $Al_{1-x}Ga_xN$ layers in the HRTEM micrograph of Figure 4.45. The BSFs coming from the $Al_{1-x}Ga_xN$/GaN interface seem

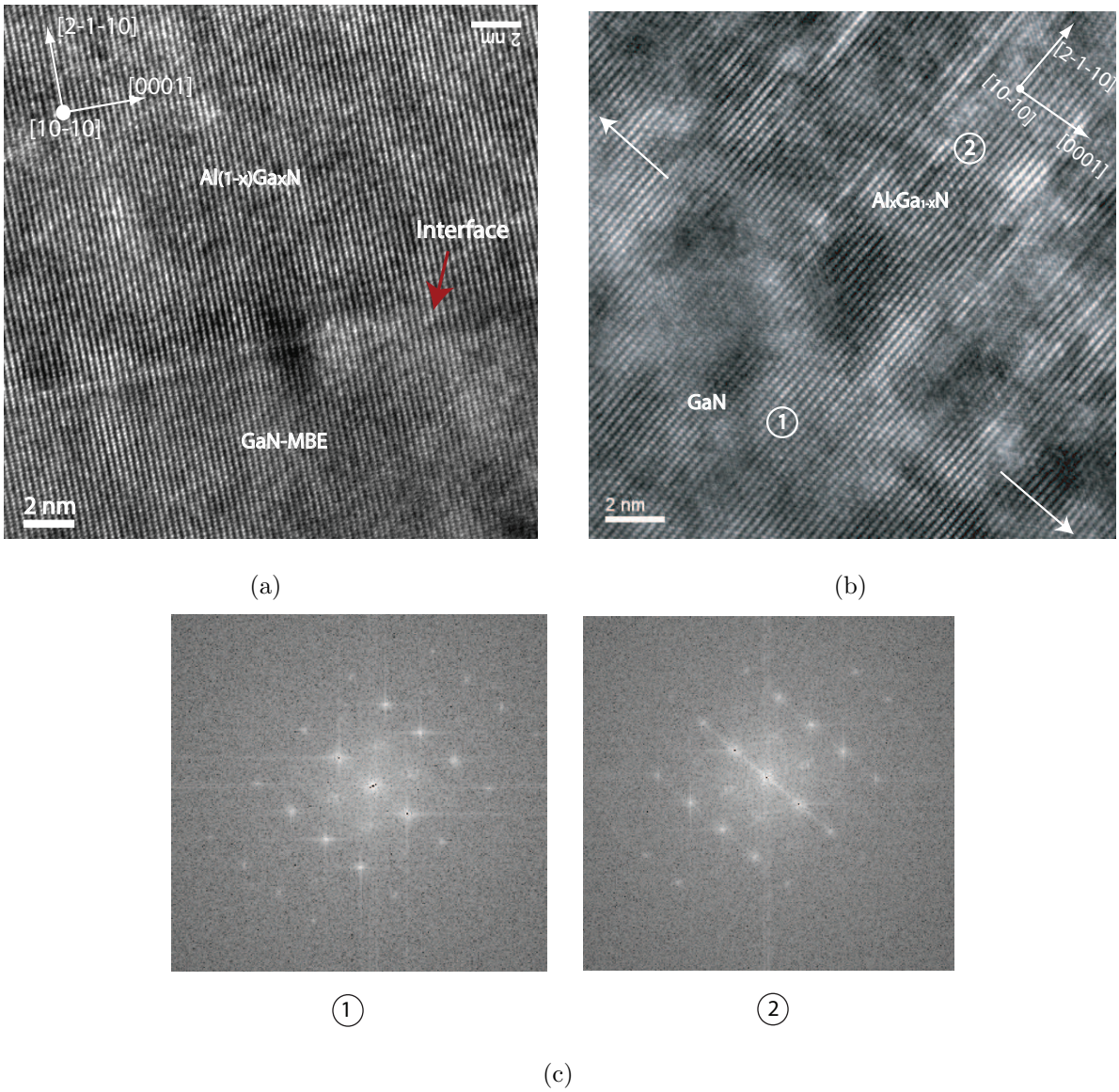

Figure 4.43: *HRTEM micrographs of the $Al_{1-x}Ga_xN/MBE-GaN$ interface taken along the $[10\bar{1}0]$ zone axis: a) smooth interface between $Al_{1-x}Ga_xN$ and $MBE-GaN$ layers (pointed with a red arrow) with a perfect match between planes, b) new defects originated at this interface, which have different contrast (dark lines) and c) Fourier transforms (FT) obtained from the two areas marked 1 and 2 in the HRTEM micrograph in Figure 4.43(b). There is a difference between the two FTs. In the area 2 the FT shows streaks parallel to* [0001] *direction.*

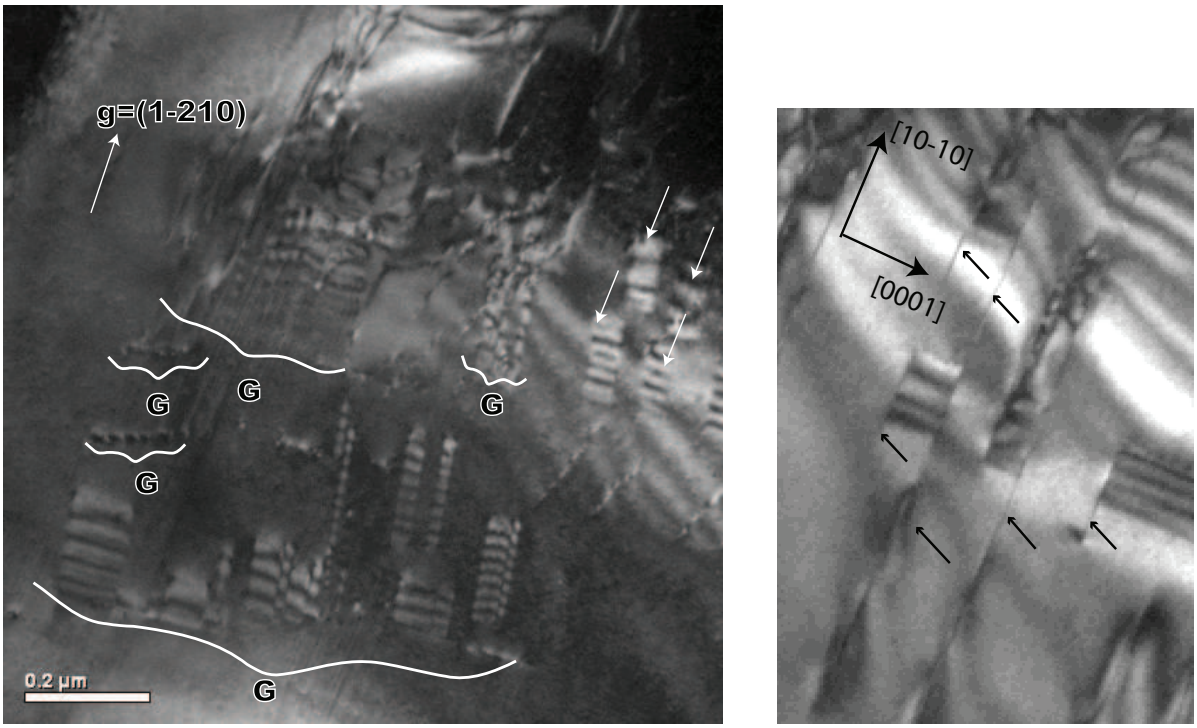

(a) (b)

Figure 4.44: *Prismatic stacking faults at GaN-SQW sample surface. a) plane of view micrograph taken under* ($\vec{g} = 1\bar{2}10$) *diffraction condition, high density of prismatic stacking faults is observed forming groups and b) plan-view micrograph at* $[2\bar{1}\bar{1}0]$ *zone axis, the prismatic stacking faults are formed at the end of two* I_1*-BSFs (black arrows).*

to be interrupted at the $Al_{1-x}Ga_xN$/GaN-SQW interface (A) and to start again at the GaN-SQW/$Al_{1-x}Ga_xN$ interface (B). These BSFs end at the top surface of the film.

Figure 4.46 shows a scheme of a MBE layer having two BSFs (red) at the interface *1* which end at the surface. According to this scheme, the BSFs do not stop at SQW-GaN/$Al_{1-x}Ga_xN$ interface, but they cross the GaN quantum well towards the surface as is shown in Figure 4.45 where the BSFs are perfect aligned.

In the analysis of the six GaN-SQW samples, we observed the same kind of defects described in this section.

In all the six samples, defects formed at the template such as TDs and BSFs crossing the MBE-layer towards the surface have been observed. Figure 4.47 shows a weak beam

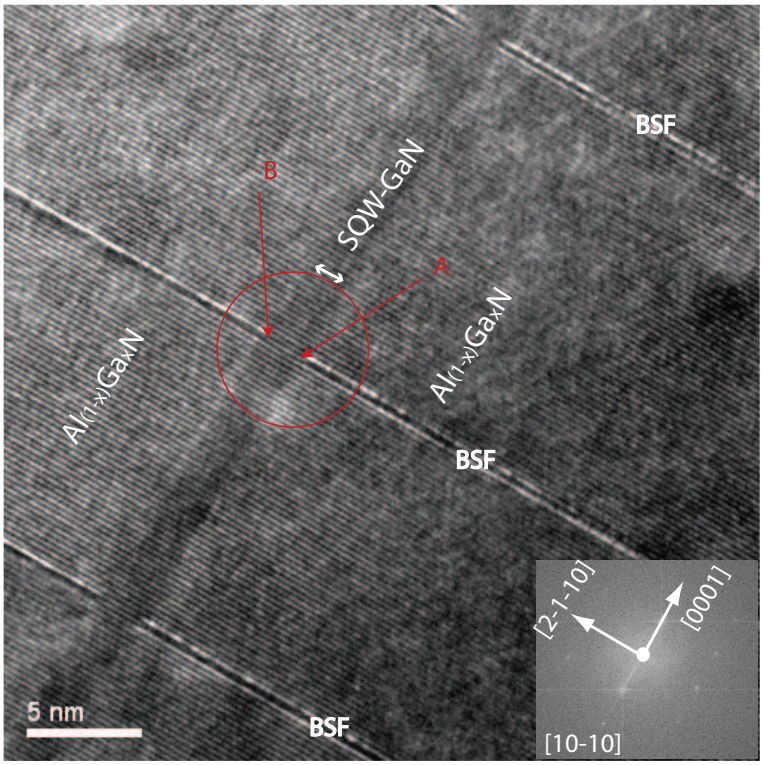

Figure 4.45: *HRTEM micrograph of the GaN single quantum well between $Al_{1-x}Ga_xN$ layers. Basal stacking faults seem that stop before and continue after the GaN-SQW.*

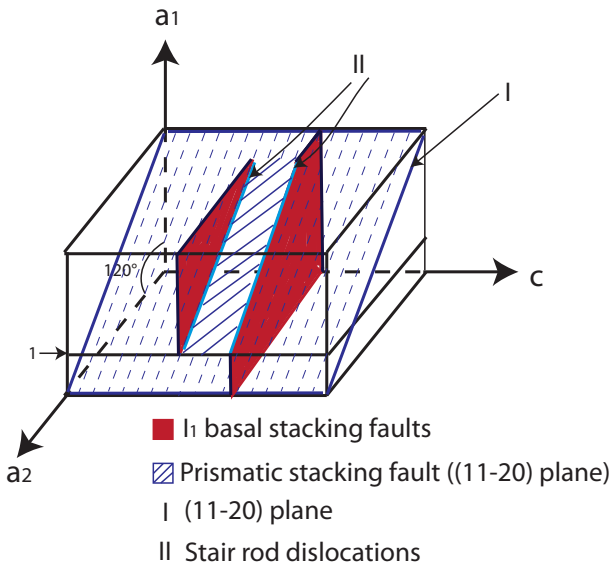

Figure 4.46: *Scheme of the structure of the MBE-layers: Position of the two basal stacking faults and the prismatic stacking faults.*

micrograph of some BSFs crossing the MBE layers. The white arrows show SFs created in the MBE layers where the partial dislocations are visible. The black arrows show BSFs created in the template crossing the MBE layers.

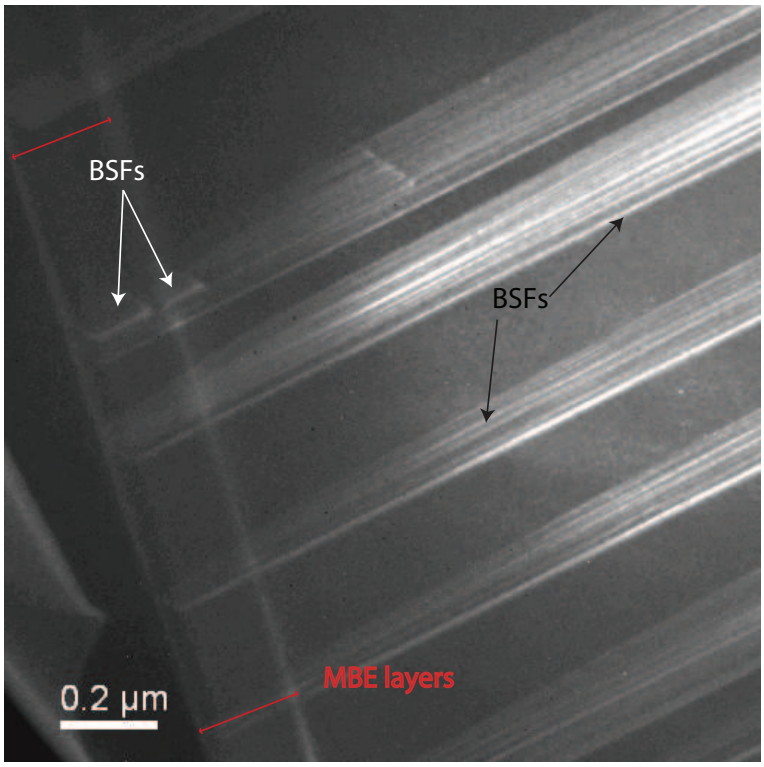

Figure 4.47: *Weak beam micrograph under* $g/3g = (0\bar{1}11)$ *diffraction condition. Basal stacking faults formed at the MBE layers are pointed by white arrows and BSFs coming fron the template are pointed by black arrows.*

4.9.3 Basal stacking faults effects on *a*-GaN quantum well.

In order to analyze the optical properties of the MBE-SQW samples, micro-photoluminescence (μ-PL) was performed in collaboration with LASPE-EPL.

Figure 4.48(a) shows a μ-PL spectrum of an a-GaN quantum well at a position free of stacking faults. Two transitions are observed, the NBE at 3.49 eV and the one related to $Al_{1-x}Ga_xN$ layers at 3.67 eV. This spectrum shows the good quality of the material. However, a μ-PL spectrum (Figure 4.48(b)) performed in a faulted area in the SQW

a-GaN samples shows three transitions: the dominant peak at 3.41 eV, the NBE and $Al_{1-x}Ga_xN$ peak . According to our results in CL and μ-PL, SFs are the defects that emit light at 3.41 eV.

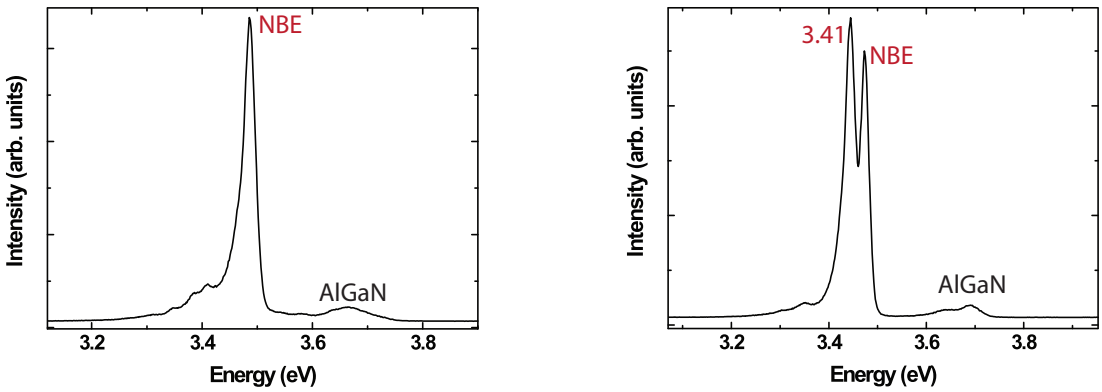

(a) (b)

Figure 4.48: *Micro-photoluminescence spectra of SQW a-GaN: a) Free of BSFs; two transitions are observed where the dominant is at 3.49 eV (NBE) and 3.67 eV ($Al_{1-x}Ga_xN$), and b) With BSFs, showing one transition more at 3.41 eV (BSFs).*

4.9.4 Discussion

A structural characterization of an *a*-GaN/$Al_{1-x}Ga_xN$ SQW grown by MBE on a-GaN template has been performed. The growth of GaN SQW is one of the important steps to produce advanced optoelectronic devices. A defect analysis of the GaN-SQW samples was performed by TEM.

High pits density, up to $1 \times 10^{12}\, cm^{-2}$, has been observed at the sample surface. A single threading dislocation of screw character at the bottom of the larger pits has been observed. Moreover, small pits have been observed originated from the intersection of several dislocations groups at the surface. Consequently, the treading dislocations are responsible for the pit formation.

BSFs are formed at the MBE-GaN/ $Al_{1-x}Ga_xN$ interface and their density ranges from 1×10^5 to $1 \times 10^6\, cm^{-1}$. They cross the GaN single quantum well and propagate towards the heterostructure surface. A high prismatic stacking fault density is measured at the MBE layers. They are located at the end of two I_1-BSFs. We can conclude that the PSFs are created during the formation of the BSFs at the MBE-GaN/ $Al_{(1-x)}Ga_xN$ interface and the propagation of the SFs in the template.

Photoluminescence spectrum shows three emissions: 3.49, 3.41 and 3.67 eV (Figure 4.48). According to Amano et al. [156] the single a-GaN quantum well samples are affected by the stacking faults, where the emission at 3.41 eV is attributed to BSFs. This emission is considered to coming from the stacking faults of the well, which form a well into the well due to the thin layer of zinc-blende embedded into the wurtzite lattice [126, 156]. This is in agreement with our results in CL and μ-PL in previous sections.

Chapter 5

Conclusions and perspectives

In this work, the microstructural characterization of a-$(11\bar{2}0)$ plane GaN films on r-$(1\bar{1}02)$ plane sapphire substrates grown by a novel HVPE-ELO process has been carried out in order to assess their structural and optical quality. The structural defects have been studied mainly by electron microscopy using two beam, weak beam and HRTEM techniques. Complementary observations of the optical properties have been carried out by using CL-SEM and μ-PL techniques. According to the TEM analysis, a-plane GaN has different structural defects and presents higher stacking fault density than c-plane GaN and therefore, the optical properties of a-GaN film are inhomogeneous along the film.

SEM analysis demonstrates that the GaN stripes morphology depends on the growth conditions, mainly temperature, H_2 flow and pressure. GaN with appropriated stripe morphology has a small growth window and therefore any small variation in the growth conditions affects the vertical and lateral growth rates. This small variation affects mainly the $(11\bar{2}0)$-horizontal facet and consequently, different ELO stripe morphology is obtained. The optimal conditions to grow a-GaN with a rectangular stripe morphology have been found to be T=1090 ^oC, H_2=3000 sccm and P=100 mbar.

This work demonstrates the locally poor structural quality of the a-$(11\bar{2}0)$ plane GaN thick films grown on r-$(1\bar{1}02)$ plane sapphire due to the high defect density formed at their interface. a-GaN/r-sapphire interface is not smooth and has steps due to the rough sapphire surface obtained after nitridation. This surface contributes to the formation of defects at the GaN/sapphire interface. The high defect density precludes a direct determination of

its structure. The study of the epitaxial growth has been found that the a-GaN/r-sapphire epitaxial relationship in this system is $(0002)[10\bar{1}0]_{GaN} \parallel (1\bar{1}04)[11\bar{2}0]_{sapphire}$. In this orientation relationship, the lattice mismatch is 1.1%, which is one order of magnitude lower than that obtained in *c*-GaN. Despite this small lattice mismatch, the a-GaN films have a higher defect density that can be attributed to lattice and thermal mismatch between GaN and sapphire, and to the imperfections of the sapphire surface.

This study has shown that a-GaN films contain a very high stacking fault and threading dislocation densities. The threading dislocation density is reduced by SiO_2 mask from 1×10^{10} to 3×10^{8} cm^{-2} and stacking fault density from 1×10^{6} to 4×10^{4} cm^{-1}, in window and overgrown areas respectively. In the window areas, the majority of the threading dislocations have screw character with Burgers vector $\vec{b} = \frac{1}{3} < 11\bar{2}0 >$ and a minority mixed character with Burgers vector $\vec{b} = \frac{1}{3} < 11\bar{2}3 >$ $(1 \times 10^{9}\, cm^{-2})$. These results demonstrate the efficiency of ELO technique, since the defect densities in the overgrown areas have been reduced by two orders of magnitude.

TEM characterization has revealed that even with the implementation of the ELO method, new dislocations and stacking faults are formed above the SiO_2 mask. These dislocations have mainly Burgers vectors $\vec{b} = \frac{1}{3}[11\bar{2}0]$ with edge character, $\vec{b} = \frac{1}{3}[2\bar{1}\bar{1}0]$ with edge character and $\vec{b} = \frac{1}{3}[\bar{1}2\bar{1}0]$ with screw character. Moreover, a few Shockley partial dislocations, with Burgers vectors $\vec{b} = \frac{1}{3} < 10\bar{1}0 >$, have been also observed in these areas. As a result, in a-GaN films above the SiO_2 mask, the defects density is still high $(10^{8}\, cm^{-2})$.

In a-GaN 4 types of stacking faults have been observed contrary to c-GaN where they are rarely observed. These stacking faults are I_1-BSFs, I_2-BSFs, $(11\bar{2}0)$-prismatic stacking faults and $(10\bar{1}0)$-stacking faults. I_1-BSFs originate at the interface during the growth due to the imperfections of the sapphire surface and they propagate towards the surface. $(11\bar{2}0)$-prismatic stacking faults are located at the end of two I_1-BSFs. It has been found that I_2-BSFs are bounded by two Shockley partial dislocations. Furthermore, $(10\bar{1}0)$-stacking faults have been observed forming closed domains. They are connected with stacking faults in (0001)-basal and $(11\bar{2}0)$-prismatic planes.

The quality of the a-GaN layers has been assessed by SEM-CL and μ-PL experiments.

These experiments have proved that the GaN layers have inhomogenous optical properties. Both techniques have shown emissions at 3.42, 3.29 and 3.21 eV which are not typical in c-GaN layers. The dominant emission at 3.42 eV results of the high density of basal stacking faults, and it is observed in both window and overgrown areas. Threading dislocations, which are non-radiative recombination centers, affect mainly the window areas. I_1-BSFs, which emit light at different energy, affect both window and overgrown areas.

The analysis of samples without and with buffer layer ($S1$ and $S2$, respectively) has shown that $S2$ samples have slightly smaller defect density leading to an improvement of the optical properties in their overgrown areas. We conclude that, the buffer layer in the GaN layer is an important factor for the reduction of the defect density.

MBE-layers have been studied by electron microscopy in order to characterize their structural defects. Their microstructural characterization has revealed that new defects are created at the $Al_{1-x}Ga_xN/GaN$ interface. These defects propagate towards the surface and have been identified as I_1-BSFs, with $\vec{R} = \frac{1}{3} < 20\bar{2}3 >$. μ-PL experiments in a-GaN single quantum well revealed two transitions. The NBE transition at 3.49 eV and another one at 3.41 eV which is attributed to the basal stacking faults. The formation of the stacking faults at the $Al_{(1-x)}Ga_xN/MBE-GaN$ interface creates prismatic stacking faults, ending at the surface. Prismatic stacking fault density is much higher in the MBE layers than in the GaN template. The defect analysis in the MBE layers has shown that dislocations and stacking faults formed in the GaN templates propagate to the surface. According to these results, the defect density in the MBE layers is higher than in the template due to the new stacking faults.

This work has also demonstrated that in order to improve the optical properties of a-GaN films and weight the structural impact of each defect, careful TEM characterization must be conducted in parallel with μ-PL and CL.

Future perspectives are:

1. The reduction of the defect density using two step ELO technique, where the overgrown areas of the 1st ELO step are the window areas of the 2nd ELO step. The SiO_2 mask

of the 2nd ELO step can stop the defects of the window areas of the 1st ELO step.

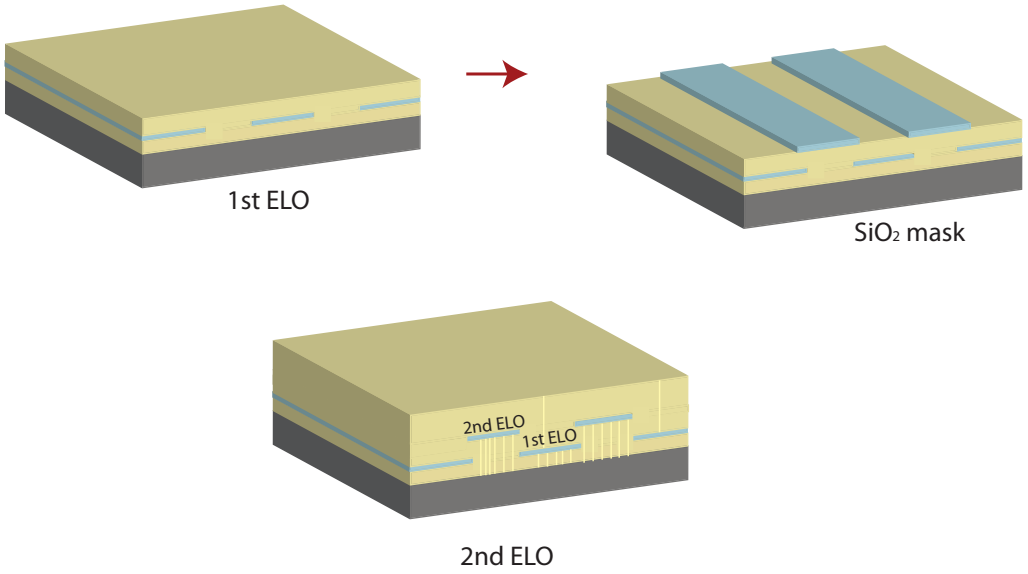

Figure 5.1: *Two steps ELO: second SiO_2 mask is deposited on the window areas from the first ELO.*

This can be a challenge since the precise alignment of the second SiO_2 mask in the window areas is a prerequisite.

2. The analysis of a-GaN using cathodoluminescence scanning transmission electron microscopy (CL-STEM) in combination with CL-SEM. CL-STEM has a higher resolution and can provide more information on particular defects (Figure 5.2). This analysis can provide guidelines to propose new growth conditions.

3. The improvement of the growth of the heterostructures by MBE in order to avoid the new defects formed at the $Al_{1-x}Ga_xN/GaN$.

4. The selection of different directions of the alignment of the SiO_2 mask, of different substrates material or/and of different non-polar growth direction. The results achieved under these new parameters could be compared with this work.

5. The selection of a-GaN homoepitaxial growth.

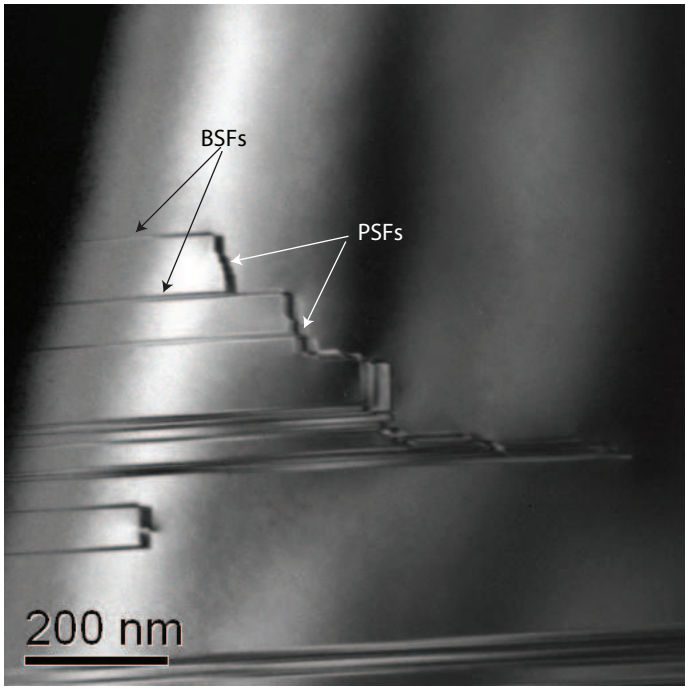

Figure 5.2: *DF micrograph of prismatic and basal stacking faults in a-GaN layers*

APPENDIX

Appendix A

Piezoelectric Polarization

The piezoelectric polarization for a binary compounds $P^{PZ}_{(X,Y)N}$ [19] (in C/m^2) can be expressed as

$$\begin{aligned} P^{PZ}_{GaN} &= -0.918\varepsilon + 9.541\varepsilon^2 \\ P^{PZ}_{AlN} &= -1.808\varepsilon + 5.624\varepsilon^2 \qquad for \qquad \varepsilon < 0 \\ P^{PZ}_{AlN} &= -1.808\varepsilon - 7.888\varepsilon^2 \qquad for \qquad \varepsilon > 0 \\ P^{PZ}_{InN} &= -1.373\varepsilon + 7.559\varepsilon^2 \end{aligned} \tag{A.1}$$

as a function of the basal strain of the III-nitrides,

$$\varepsilon = \frac{a_{subs} - a_{nitride}}{a_{nitride}} \tag{A.2}$$

with $a_{nitride}$ and a_{subs} the lattices constants of the unstrained nitride and substrate.

Appendix B

Howie-Whelan theory

In the Howie-Whelan theory considers two beams approximation, where there is only one strong diffracted beam. The amplitude changes by small increments as the beam passes through crystal slab of thicness(dz). The amplitudes ϕ_0 and ϕ_g are given by a pair of coupled differential equations:

$$\frac{d\phi_g}{dz} = \frac{\pi \mathrm{i}}{\xi_g}\phi_0 e^{-2\pi \mathrm{i} s z} + \frac{\pi \mathrm{i}}{\xi_0}\phi_g \tag{B.1}$$

and

$$\frac{d\phi_0}{dz} = \frac{\pi \mathrm{i}}{\xi_0}\phi_0 + \frac{\pi \mathrm{i}}{\xi_g}\phi_g e^{2\pi \mathrm{i} s z} \tag{B.2}$$

ξ_g, ξ_0 are the extinction distances for the diffracted and incident beams. They can be simplify by making the substitutions $\phi_0' = \phi_0 e^{\frac{-\pi \mathrm{i} z}{\xi_0}}$ and $\phi_g' = \phi_g e^{2\pi \mathrm{i} s z - \frac{\pi \mathrm{i} z}{\xi_0}}$

The Equations B.1 and B.2 became

$$\frac{d\phi_g'}{dz} = \frac{\pi \mathrm{i}}{\xi_g}\phi_0' + 2\pi \mathrm{i} s \phi_g' \tag{B.3}$$

and

$$\frac{d\phi_0'}{dz} = \frac{\pi \mathrm{i}}{\xi_g}\phi_g' \tag{B.4}$$

For a perfect crystal, these equations can be resolved by elimination of ϕ_g and $\frac{d\phi_g}{dz}$ from

the equations that leads to a second order differential equation for ϕ_0

$$\frac{d^2\phi_0}{dz^2} - 2\pi \mathrm{i} s\frac{\phi_0}{dz} + \frac{\pi^2}{\xi_g^2}\phi_0 = 0 \tag{B.5}$$

The intensity in the diffracted beam, $|\phi_g|^2 = \phi_g\phi_g^*$, the intensity at the bottom of the specimen (z=t) is given

$$1 - |\phi_0|^2 = |\phi_g|^2 = \left(\frac{\pi t}{\xi_g}\right)^2 \frac{sin^2(\pi t s_{eff})}{(\pi t s_{eff})^2} \tag{B.6}$$

s_{eff} is the effective extinction error

$$s_{eff} = \sqrt{s^2 - \frac{1}{\xi_g^2}} = \sqrt{\frac{w^2+1}{\xi_g}} \tag{B.7}$$

B.1 Contrast from an imperfect crystal

Now, we consider an imperfect crystal. The Howie-Whelan equations include the lattice distortion $\vec{R}$. So, for a imperfect crystal

$$\frac{d\phi_g}{dz} = \frac{\pi \mathrm{i}}{\xi_0}\phi_g + \frac{\pi \mathrm{i}}{\xi_g}\phi_0 e^{-2\pi \mathrm{i}(sz + \mathbf{g}.\mathbf{R})} \tag{B.8}$$

simplifying this equation by setting

$$\phi_0'(z) = \phi_0(z)e^{\frac{-\pi \mathrm{i} z}{\xi_0}} \tag{B.9}$$

and

$$\phi_g'(z) = \phi_g e^{2\pi \mathrm{i} s z - \frac{\pi \mathrm{i} z}{\xi_0} + 2\pi \mathbf{i}\mathbf{g}.\mathbf{R}} \tag{B.10}$$

The Equation B.8 becomes

$$\frac{d\phi_0'(z)}{dz} = \frac{\pi \mathrm{i}}{\xi_g}\phi_g'(z) \tag{B.11}$$

and

$$\frac{d\phi'_g}{dz} = \frac{\pi \mathbf{i}}{\xi_g}\phi'_0(z) + [2\pi \mathbf{i}(s + \mathbf{g}.\frac{d\mathbf{R}}{dz})]\phi'_g(z) \tag{B.12}$$

B.1.1 Contrast from planar defects

Figure B.1 shows a specimen with a planar defect. The upper crystal is held fixed while the lower one is translated by a vector $\vec{R}(\vec{r})$ and/or rotated through some angle θ about any axis v.

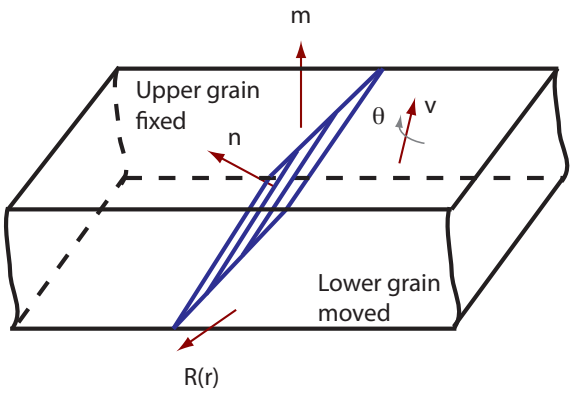

Figure B.1: *Specimen with a planar defect, the lower plane is translated by a vector* $\mathbf{R}(\mathbf{r})$ *and rotated an angle* θ *about the vector* $\mathbf{v}$*, relative to the upper grain. The defect plane is* $\mathbf{n}$*, the foil normal is* $\mathbf{m}$*.*

The Howie-Whelan equations for a planar defect are:

$$\frac{d\phi'_0(z)}{dz} = \frac{\pi \mathbf{i}}{\xi_g}\phi'_g e^{2\pi \mathbf{i}\mathbf{g}.\mathbf{R}} \tag{B.13}$$

and

$$\frac{d\phi'_g}{dz} = \frac{\pi \mathbf{i}}{\xi_g}\phi'_0(z)e^{2\pi \mathbf{i}\mathbf{g}.\mathbf{R}} + 2\pi \mathbf{i} s\phi'_g \tag{B.14}$$

These equations have the term $2\pi \mathbf{i}\mathbf{g}.\mathbf{R}$. This term is called α, and planar defects are seen when $\alpha \neq 0$

$$\alpha = 2\pi \mathbf{i}\mathbf{g}.\mathbf{R} \tag{B.15}$$

Appendix C

HRTEM image formation

Figure C.1 shows the Abbe image formation theory for a periodic specimen where the diffraction pattern consists of a set of points amplitudes, when the beam is coherent (small condenser aperture). Parallel beams are gathered to a focus in the back focal plane at a point distance $\mathbf{X}$ from the optic axis where $\mathbf{X} = \phi f$, where ϕ is $\approx$ twice the Bragg angle and f is the focal length of the lens. The image is subsequently formed by the interference of the spherical waves emitted by of the sources in the back focal plane.

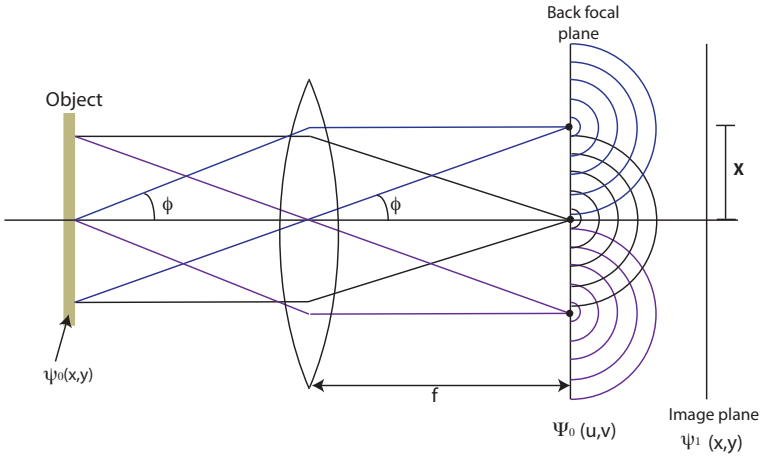

Figure C.1: *Ray diagram for the formation of an image following the Abbe theory.*

The variables used for the distribution of amplitude or intensity in the diffraction pattern are the angular variables $u = (2/\lambda)sin(\phi_x/2)$ and $v = (2/\lambda)sin(\phi_y/2)$,or in the small angle approximation, $u = x/f\lambda$ and $v = y/f\lambda$. The amplitude of the wave in the back focal plane is written as $\Psi_0(u, v)$ (u and v are termed spatial frequencies).

The formation of the Fraunhofer diffraction pattern is described by a Fourier transform operation, $\mathcal{F}$:

$$\Psi_0(u,v) = \mathcal{F}\psi_0(x,y) \tag{C.1}$$

The formation of the image is then described by two successive Fourier transform operations, and apart from scaling factor, the equation is

$$\psi_i(x,y) = \mathcal{F}[\mathcal{F}\psi_0(xy)] = \psi_0(-x,-y) \tag{C.2}$$

which therefore describes two stages on the image formation process: the interference of the wave generated at the object gives the Fraunhofer diffraction pattern in the back focal plane and interference of the waves from the back focal plane recreates the object wave function in the image plane.

The wave amplitude in the back focal plane is given for a Fourier transform

$$\Psi_0(u,v) = \mathcal{F}\psi_0(x,y) = \int \psi_0(xy)\exp[2\pi\mathfrak{i}(ux+uy)]dxdy \tag{C.3}$$

where ψ_0 is the wave leaving the object. The variables u and v are given by the angles ϕ_x and ϕ_y at which the wave leave the object.

The ideal process of imaging is described by the Equation C.4. It is the transition from the object exit wave function$\psi_0(x,y)$, to the Fourier transform Ψ_0 and back to image function ψ_i.

$$\psi_i(x,y) = \mathcal{F}\Psi_1(u,v) = \mathcal{F}[\mathcal{F}\psi_0(x,y)] = \psi_0(-x,-y) \tag{C.4}$$

where $\Psi_1 = \mathcal{F}\Psi_0$. The effect of the aperture is represented by multiplying the distribution $\Psi(u,v)$ by the aperture function

$$A(uv) = \begin{cases} 1 & , \quad if(u^2+v^2)^{\frac{1}{2}} < \frac{1}{2}a \\ 0 & , \quad otherwise \end{cases}$$

The wave front at the back focal plane is perturbed by defocus or aberrations of the lens. The perturbation is represented by multiplying $\Psi(u,v)$ by the phase factor $exp[\mathfrak{i}\chi(uv)]$.

The phase change $\chi(uv)$ contains a second order term in u and v, proportional to the defocus, Δf. Astigmatism introduces different focal lengths in the u and v direction. Assuming astigmatism can be corrected, the important aberration term is of fourth order and derives from the third order, spherical aberration term (C_s, aberration coefficient), so

$$\chi(uv) = \pi\lambda\Delta f(u^2 + v^2) + \frac{1}{2}\pi C_s\lambda^3(u^2 + v^2)^2. \tag{C.5}$$

The function that multiplies $\Psi(u, v)$ is thus $T(u, v) \equiv A(u, v)exp[\mathrm{i}\chi(uv)]$, known as the transfer function of the lens. The image amplitude is then

$$\psi_i(x, y) = \mathcal{F}[\Psi_1(u, v).T(u, v)] = \psi_0(x, y) * t(x, y) \tag{C.6}$$

The intensity distribution of the image

$$I(xy) = |\psi(xy)|^2 = |\psi_i(xy) * t(xy)|^2 \tag{C.7}$$

$t(xy)$ is the point spread function which describes the spreading of the complex amplitude of a point source by imperfections in the action of the lens system.

The equation C.7 in terms of two-dimensional vector $\mathbf{r}$ is

$$I_i(\mathbf{r}) = |\psi_1(\mathbf{r}) * t(\mathbf{r})|^2 \tag{C.8}$$

The point spread function $t(\mathbf{r})$, which produce the limitation of resolution and contrast of the image, is complex, with real and imaginary parts.

$$c(r) = \mathcal{F}Acos\chi(\mathbf{u}) \qquad s(r) = \mathcal{F}Asin\chi(\mathbf{u}) \tag{C.9}$$

which are real functions of the two dimensional vector $\mathbf{u}$ (components uv) because $cos\chi$ and $sin\chi$ are real.

For a coherent imaging system, Equation C.8 is used only when the object is very thin, for which the weak phase approximation (WPOA) is valid. For a plane wave of unit amplitude incident on such object weakly scattering:

$$\psi(\mathbf{r}) = 1 - \mathrm{i}\sigma Vp(\mathbf{r}) \tag{C.10}$$

σ is the electron matter interaction constant, $\sigma = \pi/\lambda E = 2\pi me\lambda/h^2$ and Vp is the projected potential of the crystal, $r = (x, y)$ in the z-direction. And the image intensity is

$$I(\mathbf{r}) = |1 - \mathrm{i}\sigma Vp(\mathbf{r}) * [c(\mathbf{r}) + \mathrm{i}s(\mathbf{r})]|^2 \tag{C.11}$$

with $c(r) * 1 = \int c(r)dr = 1$ and $s(r) * 1 = \int s(r)dr = 0$. Then, the intensity is given

$$I(\mathbf{r}) = 1 + 2\mathrm{i}\sigma Vp(\mathbf{r}) * s(\mathbf{r}) \tag{C.12}$$

The range of validity of WPOA is very small. When the WPOA fails, phase object approximation (POA) is used which neglectes Fresnel diffraction but includes larger phase changes.

The central beam for the diffraction pattern can be distinguished,

$$q(\mathbf{r}) = 1 + \{exp[-\mathrm{i}\sigma Vp(\mathbf{r})] - 1\} \tag{C.13}$$

so, the image intensity is given by

$$I(\mathbf{r}) = 1 + 2\sigma Vp(\mathbf{r}) - \sigma^2 Vp^2(\mathbf{r}) * c(\mathbf{r}) + [\sigma Vp * s(\mathbf{r})]^2 + [\sigma Vp * c(\mathbf{r})]^2 \tag{C.14}$$

As a first approximation $c(\mathbf{r}) = 0$

$$I(\mathbf{r}) = [1 + \sigma Vp * s(\mathbf{r})]^2 \tag{C.15}$$

For $\Delta f \approx 0$, $cos\chi = 1$ and $sin\chi = 0$, $s((r))$ can be ignored, Thus

$$I(\mathbf{r}) = 1 - \sigma^2 Vp^2(\mathbf{r}) * c(\mathbf{r}) + [\sigma Vp * c(\mathbf{r})]^2 \tag{C.16}$$

Appendix D

Transformation Miller-Miller-Bravais indices

The Bravais lattices describe the primitive and non primitive unit cells from the crystalline systems. For the hexagonal system, the unit cell is described in three axes (Figure D.1(a)) where $a = b \neq c$ and $\alpha = \beta \neq \gamma$.

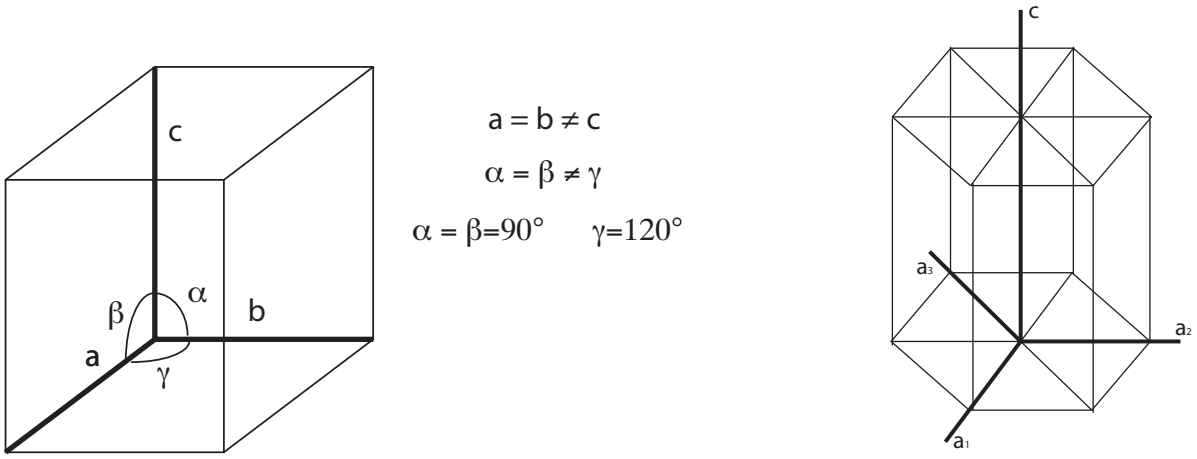

(a) (b)

Figure D.1: *Description of the hexagonal unit cells for three and four indices: a) Miller indices and b) Miller-Bravais indices.*

Miller indices can describe all planes and directions families in all the systems in three indices (hkl) and $[uvw]$ except the hexagonal system, because the planes and directions equivalent by symmetry in hexagonal system do not exhibit indices on similar form. An

alternative system was suggested, it is Miller-Bravais indices. It use four indices to give $(hkil)$ and $[uvtw]$. Figure D.1(b) describe the unit cell for the hexagonal system indicating the four axes.

To transform from MIller indices to Miller-Brave indices and vice-versa for planes and directions is necessary use the following relationships:

For planes $(hkl) \rightarrow (hkil)$, the relationship is:

$$i = -(h + k) \tag{D.1}$$

For direction $[uvw] \leftrightarrow [uvtw]$, the direction transformation is given by the following relationships:

$$u_m = u_b - t_b \qquad v_m = v_b - t_b \qquad w_m = w_b \tag{D.2}$$

$$u_b = \frac{1}{3}(2u_m - v_m) \qquad v_b = \frac{1}{3}(2v_m - u_m) \qquad t_b = -\frac{1}{3}(u_m - v_m) \qquad w_b = w_m \tag{D.3}$$

where $[u_m v_m w_m]$ is the direction in Miller indices and $[u_b v_b t_b w_b]$ in Miller-Bravais indices.

Abbreviations

AE	Auger electrons
BF	Bright field
BSE	Backscattered electrons
BSFs	Basal stacking faults
CBED	Convergent beam electron diffraction
CL	Cathodoluminescence
DF	Dark field
EDs	Energy dispersive spectrometer
EELS	Electron energy loss spectroscopy
ELO	Lateral epitaxial overgrowth
HRTEM	High resolution transmission electron microscopy
HVPE	Hydride vapor phase epitaxy
IDBs	Inversion domain boundaries
LD	Laser diodes
LED	Light emitting diodes
MBE	Molecular beam epitaxy
μ- PL	μ-photoluminescence
NBE	near band edge
PSFs	prismatic stacking faults
SAED	Select area electron diffraction
SE	Secondary electrons
SEM	Scanning electron microscopy
SQW	single quantum well
STEM	Scanning transmission electron microscopy
SFs	Stacking faults
TDs	Threading dislocations
TEM	Transmission electron microscopy
WB	Weak beam
XR	X ray

Bibliography

[1] S.C. Jain, M. Willander, J. Narayan, and R. Van Overstraeten. *Appl. Phys. Rev.*, 87(3):965, 2000.

[2] A. Chitnis, C. Cheng, V. adivarahan, M. Shatalov, E. Kuokstis, V. Mandavilli, J. Yang, and M. Asif Khan. *Appl. Phys. Lett.*, 84(18):3663, 2004.

[3] C. Chen, V. Adivarahan, J. Yang, M. Shatalov, E. Kuokstis, and M. Asif Khan. *Jpn. J. Appl. Phys.*, 42:L1039, 2003.

[4] S. Nakamura. *J. Cryst. Growth*, 201-202:290, 1999.

[5] E. Monroy, F. Calle, J. L. Pau, E. Munoz, F. Omnes, B. Beaumont, and P. Gibart. *Phys. Stat. Sol. (a)*, 185(1):91, 2001.

[6] S. J. Pearton, F. Ren, A. P. Zhang, and K. P. Lee. *Mater. Sci. Eng.*, R30:55, 2000.

[7] R. Juza and H. Hahn. *Z. Anorg. Allg. Chem.*, 239:282, 1938.

[8] H. P. Maruska and J. J. Tietjen. *Appl. Phys. Lett.*, 15(10):327, 1969.

[9] H. Amano, M. Kito, K. Hiramatsu, and I. Akasaki. *Jpn. J. Appl. Phys.*, 28(12):L2112, 1989.

[10] S. Nakamura, M. Senoh, and T. Mukai. *Jpn. J. Appl. Phys.*, 30(10a):L1708, 1991.

[11] C.Q. Chen, V. Adivarahan, M. Shatalov, M.E. Gaevski, E. Kuokstis, J. W. Yang, H.P. Maruska, Z. Gong, M. Asif Khan, R. Liu, A. Bell, and F.A Ponce. *Phys. Stat Sol.*, 2(7):2732, 2005.

[12] H. Marchand, X. Wu, J. P. Ibbetson, P. T. Fini, P. Kozodoy, S. Keller, J. S. Speck, S. DenBaars, and U. K. Mishra. *Appl. Phys. Lett.*, 73(6):747, 1998.

[13] V. Wagner, O. Parillaud, H. J. Buhlmann, M. Ilegems, S. Gradecak, P. Stadelmann, T. Riemann, and J. Christen. *J. Appl. Phys.*, 92(3):1307, 2002.

[14] B.A. Haskell, F. Wu, M.D. Craven, S. Matsuda, P.T. Fini, T. Fuji, K. Fujito, S.P. DenBaars, J.S. Speck, and Shuji Nakamura. *Appl. Phys. Lett.*, 83(4):644, 2003.

[15] V. Potin, P. Ruterana, and G. Nouet. *J. Phys. Condens. Matter*, 12(49):10301, 2000.

[16] S.Nakamura, S. Pearton, and G. Fasol. *The Blue Laser Diode*. Springer, second edition, Germany, 2000.

[17] F. Bernardini, V. Fiorentini, and D. Vanderbilt. *Phys. Rev. B*, 56(16):R10024, 1997.

[18] F. Bernardini, V. Fiorentini, and D. Vanderbilt. *Phys. Rev. B*, 63:193201, 2001.

[19] V. Fiorentini, F. Bernardini, and O. Ambacher. *Appl. Phys. Lett.*, 80(7):1204, 2002.

[20] O. Ambacher, J. Smart, J. R. Shealy, N. G. Weimann, K. Chu, M. Murphy, W. J. Schaff, L. F. Eastman, R. Dimitrov, L. Wittmer, M. Stutzmann, W. Rieger, and J. Hilsenbeck. *J. Appl. Phys.*, 85(6):3222, 1999.

[21] M.S. Shur, A.D. Bykhovski, R. Gaska, and M. A. Khan. *Handbook of the Thin Film Devices*, volume I. Academy Press, 2000.

[22] D. Du and D. J. Srolovitz. *Acta Mater.*, 52:3365, 2004.

[23] E.S. Hellman. *MRS Internet J. Nitride Semicond. Res.*, 3:11, 1998.

[24] K. Dovidenko, S. Oktyabrsky, J. Narayan, and M. Razeghi. *MRS Internet J. Nitride Semicond. Res.*, 4S1:G6.46, 1999.

[25] Z. Liliental-Weber, T. Tomaszewicz, D. Zakharov, and M.A. O'Keefe. *J. Cryst. Growth*, 281:125, 2005.

[26] J. Pankove and T. D. Moustakas. *Gallium Nitride (GaN) I*, volume 50. Semiconductor and semimetals, 1998.

[27] D. I. Florescu, J.C. Ramer, D. S. Lee, and A. Armour. *Appl. Phys. Lett.*, 84(25):5252, 2004.

[28] A. Dussaigne, B.Damilano, J. Brault, J. Massies, E. Feltin, and N. Grandjean. *J. Appl. Phys.*, 103:013110, 2008.

[29] Z. Chen, N. Fichtenbaum, D. Brown, S. Keller, U. K. Mishra, S. P. Denbaars, and S. Nakamura. *J. Electron. Mater.*, article in press.

[30] S.N. Lee, H.S. Paek, J. K. Son, T. Sakong, O. H. Nam, and Y. Park. *J. Cryst. Growth*, 3007:358, 2007.

[31] T. Lei, Jr. K. F. Ludwig, and T. D. Moustakas. *J. Appl. Phys.*, 74(7):4430, 1993.

[32] S. Tripathy, R. K. Soni, H. Asahi, K. Iwata, R. Kuroiwa, K. Asami, and S. Gonda. *J. Appl. Phys.*, 85(12):8386, 1999.

[33] D. N. Zakharov, Z. Liliental-Weber, B. Wagner, Z. J. Reitmeier, E. A. Preble, and R. F. Davis. *Phys. Rev. B*, 71:235334, 2005.

[34] J. H. Song, Y. Z. Yoo, T. Sekiguchi, K. Nakajima, P. Ahmet, T. Chikyow, K. Okuno, M. Sumiya, and H. Koinuma. *Phys. Stat. Sol. (c)*, 0(7):2520, 2003.

[35] P. Waltereit, O. Branddt, A. Trampert, H. T. Grahn, J. Menninger, M. Ramsteiner, M. Reiche, and K. H. Ploog. *Lett. to Nature*, 406:865, 2000.

[36] T. Paskova, V. Darakchieva, P.P. Paskov, J. Birch, E. Valcheva, P.O.A. Persson, B. Arnaudov, T. Tungasmitta, and J B. Monemar. *J. Cryst. Growth*, 281:55, 2005.

[37] M. D. Reed, O. M. Kryliouk, M. A. Mastro, and T.J. Anderson. *J. Cryst. Growth*, 274(1-2):14, 2005.

[38] N. Akopian, G. Bahir, D. Gershoni, M. D. Craven, J. S. Speck, and S. P. DenBaars. *Appl. Phys. Lett.*, 86(20):202104, 2005.

[39] S. Ghosh, P. Waltereit, O. Brandt, H. T. Grahn, and K. H. Ploog. *Phys. Rev. B*, 65(7):0752021, 2002.

[40] D.S. Li, H. Chen, H.B. Yu, X.H. Zheng, Q. Huang, and J.M. Zhou. *Chin. Phys. Lett.*, 21(5):970, 2004.

[41] E. V. Etzkorn and D. R. Clarke. *J. Appl. Phys.*, 89(2):1025, 2001.

[42] K. Iwata, H. Asahi, K. Asami, R. Kuroiwa, and S. Gonda. *Jpn. J. Appl. Phys Part.2*, 36(6A):L661, 1997.

[43] C. Sun and M. Razeghi. *Appl. Phys. Lett.*, 63(7):973, 1993.

[44] P. Vennegues and Z. Bougrioua. *Appl. Phys. Lett.*, 89:111915, 2006.

[45] C. Q. Chen, J. Zhang, J. Yang, V. Adivarahan, S. Rai, S. Wu, H. Wang, W. Sun, M. Su, Z. Gong, E. Kuokstis, M. Gaevskiand, and M. Asif Khan. *Jpn. J. Appl. Phys., Part 2*, 42(No. 7B):L818, 2003.

[46] D.S. Li, H. Chen, H.B. Yu, J. Y. Han, X.H. Zheng, Q. Huang, and J.M. Zhou. *J. Cryst. Growth*, 263:76, 2003.

[47] M. D. Craven, S. L. Lim, F. Wu, J.S. Speck, and S.P. DenBaars. *Phys. Stat. Sol. (a)*, 194(2):541, 2002.

[48] M. D. Craven, F. Wu, A. Chakraaborty, B. Imer, U. K. Mishra, S. P. DenBaars, and J.S. Speck. *Appl. Phys. Lett.*, 84(8):1281, 2004.

[49] J. H. Song, Y. Z. Yoo, K. Nakajima, T. Chikyow, T. Sekiguchi, and H. Koinuma. *J. Appl. Phys.*, 97:043531, 2005.

[50] E. Eiper, A. Hofmann, J. W. Gerlach, B. Rauschenbach, and J. Keckes. *J. Cryst. Growth*, 284:561, 2005.

[51] B. P. Wagner, Z. J. Reitmeier, J. S. Park, D. Bachelor, D. N. Zakharov, Z. Liliental-Weber, and R. F. Davis. *J. Cryst. Growth*, 290(2):504, 2006.

[52] M. D. Craven, A. Chakraaborty, B. Imer, F. Wu, S. Keller, U. K. Mishra, J.S. Speck, and S. P. DenBaars. *Phys. Stat. Sol. (c)*, 0(7):2132, 2003.

[53] T. Paskova, V. Darakchieva, P.P. Paskov, J. Birch, E. Valcheva, P.O.A. Persson, B. Arnaudov, T. Tungasmitta, and J B. Monemar. *Phys. Stat. Sol. (c)*, 2(7):2027, 2005.

[54] P. P. Paskov, R. Schifano, B. Monemar, T. Paskova, S. Figge, and D. Hommel. *J. Appl. Phys.*, 98(9):1, 2005.

[55] Gradecak S. *Structural and Optical Properties of Laterally Overgrowth Gallium Nitride Studied by Electron Microscopy.* PhD thesis, EPFL, No. 2880, 2003.

[56] J. P. Hirth and J. Lothe. *Theory of Dislocations.* John Wiley and Sons, second edition, New York, 1982.

[57] P. Hirsch, A. Howie, R. Nicholson, D. W. Pashley, and M. J. Whelan. *Electron Microscopy of Thin Crystals.* Krieger Publishing Company, 1977.

[58] M.H. Loretto and R.E. Smallma. *Defect Analysis in Electron Microscopy.* Chapman and Hall Ltd, London, 1975.

[59] L. J. Teutonico. *Mater. Sci. Eng.*, 6:27, 1970.

[60] I. Y. Knoke, E. Meissner, J. Friedrich, H. P. Strunk, and G. Muller. *J. Cryst. Growth*, 310:3351, 2008.

[61] D. J. H. Cockayne, I. L. F Ray, and M. Whelan. *Philos. Mag.*, 20:1265, 1969.

[62] D. J. H. Cockayne. *Ann. Rev. Mater. Sci.*, 11:75, 1981.

[63] B.G Yacobi and D.B. Holt. *Cathodoluminescence Microscopy of Inorganic Solids.* Plenum Press, New York, 1990.

[64] T. Detchprohm, K. Hiramatsu, N. Sawaki, and I. Akasaki. *J. Cryst. Growth*, 137(1-2):170, 1994.

[65] C. Kirchner, V. Schwegler, F. Eberhard, M. Kamp, J. K. Ebeling, P. Prystawko, M. Leszzynski, I. Grzegory, and S. Porowski. *Prog. Cryst. Growth Charact. Mater.*, 41:57, 2000.

[66] S. Porowski. *J. Cryst. Growth*, 189-190:153, 1998.

[67] T. Paskova, V. Darakchieva, E. Valcheva, P.P. Paskov, J B. Monemar, and M. Heuken. *J. Cryst. Growth*, 257:1, 2003.

[68] A. Gassmann, T. Suski, N. Newman, C. Kisielowski, E. Jones, E. R. Weber, Z. Liliental-Weber, M. D. Rubin, H. I. Helava, I. Grzagory, M. Bockowski, J. Jun, and S. Porowski. *J. Appl. Phys.*, 80(4):2195, 1996.

[69] B.A. Haskell, F.wu, S. Matsuda, M.D. Craven, P.T. Fini, S.P. DenBaars, J.S. Speck, and Shuji Nakamura. *Appl. Phys. Lett.*, 83(8):1554, 2003.

[70] R. A. Oliver, M. J. Kappers, C. McAleese, R. Datta, J. Sumner, and C. J. Humphreys H. *J. Mater. Sci: Mater Electron*, 19:S208, 2008.

[71] K. Pakula, J. M. Baranowski, and Borysiuk. *Cryst. Res. Technol.*, 42(12):1176, 2007.

[72] C. E. C. Dam, A. P. grzegorczyk, P. R. Hageman, and P. L. Larsen. *J. Cryst. Growth*, 290:473, 2006.

[73] W. Zhou, D. Ren, and P. D. Dapkus. *J. Cryst. Growth*, 283:31, 2005.

[74] H. P. D. Schenk, P. Vennegues, O. Tottereau, T. Riemann, and J. Cristen. *J. Crystal Growth*, 258:232, 2003.

[75] X. J. Ning, F. R. Chien, and P. Pirouz. *J. Mater. Res.*, 11(3):580, 1996.

[76] L. Liu and J. H. Edgar. *Mat. Sci. Eng., R*, 37:61, 2002.

[77] www.crystal-gmbh.com.

[78] T. Sasaki and S. Zembutsu. *J. Appl. Phys.*, 61(7):2533, 1987.

[79] A. Koukitu and Y. Kumagai. *J. Phys. Condens. Matter*, 13(32):6907, 2001.

[80] D. A. Neumayer and J. G. Ekerdt. *Chem. Mater.*, 8(1):9, 1996.

[81] X. Wang and A. Yoshikawa. *Prog. Cryst. Growth Charact. Mater.*, 48-49(1-3):42, 2004.

[82] R. Cadoret and A. Trassoudaine. *J. Phys. Condens. Matter*, 13(32):6893, 2001.

[83] D. Martin, J. Napierala, M. Ilegems, R. Butte, and N. Grandjean. *Appl. Phys. Lett.*, 88:241914, 2006.

[84] H. Wang, C. Chen, Z. Gong, J. Zhang, M. Gaevski, M. Su, J. Yang, and M. Asif Khan. *Appl. Phys. Lett.*, 84(4):499, 2004.

[85] V. S. Ban. *J. Electrochem. Soc*, 119(6):761, 1972.

[86] D. Martin, J. F. Carlin, V. Wagner, H. J. Buhlmann, and M. Ilegems. *Phys. Stat. Sol. (a)*, 194(2 SPEC.):520, 2002.

[87] V. Wagner. *Growth of GaN by Hydride Vapor Epitaxy.* PhD thesis, EPFL, No. 2462, 2001.

[88] T. Hashimoto, M. Yuri, M. Ishida, Y. Terakoshi, O. Imafuji, T. Sugino, and K. Itoh. *Jpn. J. Appl. Phys.*, 38:6605, 1999.

[89] P. Vennegues and B. Beaumont. *App. Phys. Lett.*, 75(26):4115, 1999.

[90] K. Uchida, A. Watanabe, M. Kouguchi, T. Tanaka, and S. Minagawa. *J. Appl. Phys.*, 79(7):3487, 1996.

[91] T. Zhu, D. Martin, R. Butté, J. Napierala, and N. Grandjean. *J. Cryst. growth*, 300(1):187, 2007.

[92] S.A. Kukushkin, A. V. Osipov, V. N. Bessolov, B. K. Medvedev, V. K.Nevolin, and K. A. Tcarik. *Rev. Adv. Mater. Sci.*, 17:1, 2008.

[93] N. Grandjean, J. Massies, P. Vennegues, M. Laugt, and M. Leroux. *Appl. Phys. Lett.*, 70(5):643, 1997.

[94] W. A. Melton and J. I. Pankove. *J. Cryst. Growth*, 178(1-2):168, 1997.

[95] P. Ruterana, V. Potin, B. Barbaray, and G. Nouet. *Philos. Mag., A*, 80(4):937, 2000.

[96] F. Wu, M. D. Craven, S. H. Lim, and J. S. Speck. *J. Appl. Phys.*, 94(2):942, 2003.

[97] Hull. D. *Introduction to Dislocations.* Pergamon Press, second edition, Oxford, 1975.

[98] D. Cherns and M. E. Hawkridge. *J. Mater. Sci.*, 41:2685, 2006.

[99] Ph. Komninou, J. Kioseogluo, G. P. Dimitrakopulos, Th. Kehagias, and Th. Karakostas. *Phys. Stat. Sol. (a)*, 202(15):2888, 2005.

[100] P. Ruterana, J. Chen, and G. Nouet. *Mat. Scien. Eng., B*, 82:123, 2001.

[101] I. Markov. *Crystal Growth for Beginners: Fundamentals of Nucleation, Crystal Growth and Epitaxy.* World Scientific, Singapore, 1995.

[102] P. Ruterana and G. Nouet. *Mater. Chem. Phys.*, 81:249, 2003.

[103] D.S. Li, H. Chen, H.B. Yu, X.H. Zheng, Q. Huang, and J.M.Zhou. *J. Cryst. growth*, 265:107, 2004.

[104] M.D. Craven, S.H. Lim, F. Wu, J.S. Speck, and S.P. DenBaars. *Appl. Phys. Lett.*, 81(3):469, 2002.

[105] S. Jursenas, E. Kuokstis, S. Miasojedovas, G. Kurilcik, A. Zukauskas, C. Q. Chen, J. W. Yang, V. Adivarahan, and M. Asif Khan. *Appl. Phys. Lett.*, 85(5):771, 2004.

[106] B. Beaumont, Ph Vennegues, and P. Gibart. *Phys. Stat. Sol. (b)*, 227(1):1, 2001.

[107] J. L. Rouviere, M. Arlery, B. Daudin, G. Feuillet, and O. Briot. *Mat. Sci. Eng., B*, 50(1-3):61, 1997.

[108] M.D. Craven, S.H. Lim, F. Wu, J.S. Speck, and S.P. DenBaars. *Appl. Phys. Lett.*, 81(7):1201, 2002.

[109] A. Sakai, H. Sunakawa, A. Kimura, and A. Usui. *Appl. Phys. Lett.*, 76(4):442, 2000.

[110] S. Gradecak, V. Wagner, M. Ilegems, T. Riemann, J. Crysten, and P. Stadelmann. *Appl. Phys. Lett.*, 80(16):2866, 2002.

[111] H. K. Cho, J. Y. Lee, K. S. Kim, G. M. Yang, J. H. Song, and P. W. Yu. *J. Appl. Phys.*, 89(5):2617, 2001.

[112] X. Ni, U. Ozgur, Y. Fu, N. Biyikli, J. Xie, A: Baski, H. Morkoc, and Z. Liliental-Weber. *Appl. Phys. Lett.*, 89(26):262105, 2006.

[113] R. Liu, A. Bell, F. A. Ponce, C. Q. Chen, J. W. Yang, and M. A. Khan. *Appl. Phys. Lett.*, 86:021908, 2005.

[114] A. Chakraborty, Stacia Keller, C.Meier, B. A. Haskell, S. Keller, P.Watereit, S. P. DeBaars, S. Nakamura, J. S. Speck, and U. K. Mishry. *Appl. Phys. Lett.*, 86:031901, 2005.

[115] W.H. Sun, J. W. Yang, C. Q. Chen, J. P. Zhang, M. Gaevski, E. Kuokstis, V. Adivarahan, H. M. Wang, Z. Gong, M. Su, and M. Asif Khan. *Appl. Phys. Lett.*, 83(13):2599, 2003.

[116] W.H. Sun, E. Kuokstis, M. Gaevski, J. P. Zhang, C. Q. Chen, H. M. Wang, J. W. Yang, G. Simin, M. Asif Khan, R. Gaska, and M. S. Shur. *Phys. Stat. Sol. (a)*, 200(1):48, 2003.

[117] V. Adivarahan, S. Wu, J. P. Zhang, A. Chitnis, M. Shatalov, V. Mandavilli, R. Gaska, and M. Asif Khan. *Appl. Phys. Lett.*, 84(23):4762, 2004.

[118] K. Hiramatsu, K. Nishiyama, A. Motogaito, H. Miyake, Y. Iyechica, and T. Maeda. *Phys. Stat. Sol. (a)*, 176:535, 1999.

[119] P. Stadelmann. http:cimewww.epfl.ch/people/stadelmann/jemswebsite/jems.html.

[120] R. Kroger, T. Paskova, S. Figge, D. Hommel, A. Rosenauer, and B. Monemar. *Appl. Phys. Lett.*, 90:081918, 2007.

[121] T. Hashimoto, Y. Terakoshi, M. Yuri, M. Ishida, O. Imafuji, T. Sugino, and K. Itoh. *J. Appl. Phys.*, 86(7):3670, 1999.

[122] F. Dwikusuma. *J. Appl. Phys.*, 94(9):5656, 2003.

[123] A. K. Head, P. Humble, L. M. Clarebrough, A. J. Morton, and C. T. Forwood. *Computed Electron Micrographs and Defect Identification.* North-Holland, Amsterdam, 1973.

[124] Z. Liliental-Weber, M. Benamara, W. Swider, J.Park, P. A. Grudowski, C. J. Eiting, and R. D. Depuis. *MRS Internet J. Nitride Semicond. Res.*, 4S1:4.6, 2000.

[125] B. A. Haskell, S. Nakamura, S. P. DenBaars, and J. S. Speck. *Phys. Stat. Sol. (c)*, 244(8):2847, 2007.

[126] C. Stampfl and G. Van de Walle. *Phys. Rev. B*, 57(24):R15052, 1998.

[127] C. M. Drum. *Philos. Mag.*, 11(313), 1965.

[128] D. Hull and D. J. Bacon. *Introduction to Dislocations*. Butterworth-Heinemann, fourth edition, Oxford, 2001.

[129] R.B. Schwarz, K. Khachaturyan, and E. R. Weber. *Appl. Phys. Lett.*, 70(9):1122, 1997.

[130] K. Kim, W. R. L. Lambrecht, and B. Segall. *Phys. Rev. B*, 53(24):16310, 1996.

[131] A. F. Wright. *J. Appl. Phys.*, 82(6):2833, 1997.

[132] A. Polian, M. Grimsditch, and I. Grzegory. *J. Appl. Phys.*, 79(6):3343, 1996.

[133] G. P. Dimitrakopulos, A. M. Sanchez, Ph. Komninou, Th. Kehagias, Th. Karakostas, and G. Nouet P. Ruterana. *Phys. Stat. Sol. (b)*, 242(8):1617, 2005.

[134] V. Potin, G. Nouet, and P. Ruterana. *Philos. Mag. A*, 79(12):2899, 1999.

[135] Y. Xin, P. D. Brown, C. J. Humphreys, T. S. Cheng, and C. T. Foxon. *Appl. Phys. Lett.*, 70(10):1308, 1997.

[136] Z. Liliental-Weber, H. Sohn, N. Newman, and J. Washburn. *J. Vac. Sci. Technol: B*, 13(4):1578, 1995.

[137] X. H. Wu, L. M. Brown, D. Kapolnek, S. Keller, B. Keller, S. P. DenBaars, and J. S. Speck. *J. Appl. Phys.*, 80(6):3228, 1996.

[138] J. E. Northrup, J. Neugebauer, and L.T. Romano. *Phys. Rev. Lett.*, 77(1):103, 1996.

[139] A. F. Wright. *J. Appl. Phys.*, 82(10):5259, 1997.

[140] L. Zhou, R. Chandrasekaran, T. D. Moustakas, and J. S. Smith. *J. Cryst. Growth*, 310:2981, 2008.

[141] I. Yonenaga, H. Makino, S. Itoh, and T. Yao. *Phys. Stat. Sol. (c)*, 2:1817, 2005.

[142] T. Paskova, S. Tungasmita, E. Valcheva, E. B. Svedberg, B. Arnaudov, S. Evtimova, P. A. Persson, A. Henry, R. Beccard, M. Heuken, and B. Monemar. *MRS Internet J. Nitride Semicond. Res.*, 5 SUPPL. 1(W3.14), 2000.

[143] P. P. Paskov, R. Schifano, B. Monemar, T. Paskova, S. Figge, and D. Hommel. *J. Appl. Phys.*, 98, 2005.

[144] J. Mei, S. Srinivasan, R. Lui, F. A. Ponce, Y. Narokawa, and T. Mukai. *Appl. Phys. Lett.*, 88:141912, 2006.

[145] P. P. Paskov, T. Paskova, B. Monemar, S. Figge, D. Hommel, B. A. Haskell, P. T. Fini, J. S. Speck, and S. Nakamura. *Superlattices Microstruct.*, 40(4-6 SPEC. ISS.):253, 2006.

[146] M.A. Reshchikov and H. Morkoc. *Phys. B*, 376-377:428, 2006.

[147] P. P. Paskov, R. Schifano, T. Malinauskas, T. Paskova, J. P. Bergman, B. Monemar, S. Figge, D. Hommel, B. A. Haskell, P. T. Fini, J. S. Speck, and S. Nakamura. *Phys. Stat. Sol. (c)*, 3(6):1499, 2006.

[148] X. H. Wu, P. Fini, E. J. Tarsa, B. Heying, S. Keller, U. K. Mishra, S. P. DenBaars, and J. S. Speck. *J. Cryst. Growth*, 189-190:231, 1998.

[149] P. Fini, X. Wu, E. J. Tarsa, J. Golan, V. Srikant, S. Keller, S. P. Denbaars, and J. S. Speck. *Jpn. J. Appl. Phys Part.1*, 37:4460, 1998.

[150] P. Vennegues, B. Beaumont, V. Bousquet, M. Vaille, and P. Gibart. *J. Appl. Phys.*, 87(9):4175, 2000.

[151] A. E. Romanov, P. Fini, and J. S. Speck. *J. Appl. Phys.*, 93(1):106, 2003.

[152] S. F. Chichibu, T. Koida, M. D. Craven, B.A. Haskell, T. Onuma, T. Sota, J. S. Speck, S. P. Den Baars, and S. Nakamura. *Phys. Stat. Sol. (c)*, 2(7):2700, 2005.

[153] S. N. Lee, H.P. Paek, H. Kim, Y. M. Park, T. Jang, and Y. Park. *Appl. Phys. Lett.*, 92:111106, 2008.

[154] J. Kim and K. H. Baik. *J. Ceram. Proc. Res.*, 8(4):277, 2007.

[155] T. Kozawa, T. Kachi, T Ohwaki, Y. Taga, N. Koide, and M. Koike. *J. Electrochem. Soc.*, 143(1):L17, 1996.

[156] H. Amano C. R. Abernathy and J. C. Zolpe, editors. *Material Reseach Society: Gallium Nitride and Related Materials II*, number 468. Material Reaseach Society, 1997.

Acknowledgements

This work was finished with the help of many people who have been given me support, encouragement and inspiration. I would especially like to thank the following people:

Professor Pierre Stadelmann who gave me the opportunity to do my thesis at CIME as well as for his advice and support during these years.

Prof. Karen Scrivener for presiding the thesis jury and Prof. K. Leifer, Dr. J. Michler and Dr F. Diologent for being members of the jury.

This work would not have been possible without the collaboration with LASPE: my gratitude goes to Prof. N. Grandjean and especially T. Zhu for providing the GaN samples.

Many thanks to Daniel Laub for teaching me the preparation of the TEM GaN samples, to Marco Cantoni and to Prof. Buffat for their explanations at the microscope. I would like to thank Doncan, Ben, Nirav and Aristeidis for reading and correcting this thesis.

I would like to thanks all my friends for their support during this work: Lisa, Erika, Naama, Jelena, Mercedes, Carla, Nirav, Ben, Ali, Kim, Michal K., Aga, Michael D., Blanca, Sandeep, Bojana, Barbora. A special thanks to Aristeidis for making my life happy.

To the people I owe the most: Susana and Daniel, Dani, Esther, Magoli and todos mis niños, thanks for always believing in me. Gracias por su apoyo en cada una de las decisiones que yo he tomado.

Curriculum Vitae

Yadira Arroyo Rojas Dasilva

Born in April 4th,1975
Nationality: Mexican
Email: yadira.arroyo@epfl.ch

Av. Beaulieu 3
Lausanne 1004
Switzerland

Education:

2004-Present	*PhD thesis in Materials Science* CIME- Centre interdisciplinaire du microscopie electronique Ecole Politechnique Federale de Lausanne Lausanne, Switzerland
2000-2003	*Master in Metallurgy and Materials Science* Metallurgical researches institute Michoacana de San Nicolas de HIdalgo University Morelia, Michoacán, Mexico.
1993-1998	*Diploma in Chemical Engineering* Chemical Engineering Faculty Michoacana de San Nicolas de HIdalgo University Morelia, Michoacán, Mexico.

Work Experiences

2004-Present	*Assistant* CIME-Centre interdisciplinaire du microscopie electronique Ecole Politechnique Federale de Lausanne Lausanne, Switzerland
2004-2004	*Teaching* Industrial Engineering Vasco de Quiroga University Morelia, Michoacán, Mexico.
2002-2004	*Teaching* Modstil A.C. Institute Morelia, Michoacán, Mexico.

Conference presentations

Y. Arroyo Rojas Dasilva, T. Zhu, D. Martin, N. Grandjean and P. Stadelmann. "Characterization of a-plane GaN films grown on r-plane sapphire substrate by electron microscopy" (oral presentation). 14th European microscopy congress, Aachen,Germany, 2008.

Y. Arroyo Rojas Dasilva, J. Napierala, D. Martin and P. Stadelmann. "Transmission electron microscopy study of GaN films by HVPE-ELO" (poster presentation). 16th International microscopy congress, Sapporo, Japan, 2006.

Y. Arroyo and P. Stadelmann. "Electron microscopy characterization of GaN films by ELO on sapphire. Microscopy conference" (poster presentation), Davos, Switzerland, 2005.
